

RADIALLY SPREADING SURFACE FLOWS

by

MICHAEL RAY MACLATCHY

B.A.Sc., The University of British Columbia, 1991  
M.A.Sc., The University of British Columbia, 1993

A THESIS SUBMITTED IN PARTIAL FULFILLMENT OF  
THE REQUIREMENTS FOR THE DEGREE OF  
DOCTOR OF PHILOSOPHY

in

THE FACULTY OF GRADUATE STUDIES

(Department of Civil Engineering)

We accept this thesis as conforming  
to the required standard

THE UNIVERSITY OF BRITISH COLUMBIA

March 1999

© Michael Ray MacLatchy, 1999

In presenting this thesis in partial fulfilment of the requirements for an advanced degree at the University of British Columbia, I agree that the Library shall make it freely available for reference and study. I further agree that permission for extensive copying of this thesis for scholarly purposes may be granted by the head of my department or by his or her representatives. It is understood that copying or publication of this thesis for financial gain shall not be allowed without my written permission.

Department of Civil Engineering

The University of British Columbia  
Vancouver, Canada

Date April 1<sup>st</sup> 1989

## Abstract

The present study investigated the radially spreading surface flow that is created when a vertical buoyant jet is discharged in shallow water and surfaces. Experiments were conducted for a series of vertical buoyant jets discharging into a shallow circular tank specially designed to simulate an infinite ambient water body so that downstream control effects were avoided. A range of flow rates and port diameters were utilized to determine the nature of the flow structure in the radially spreading surface region. Velocity profiles using an ADV, and temperature profiles using a thermistor array, were made throughout the radial flow region.

The present study concentrated on the radial buoyant jet region of a vertical buoyant jet discharged in shallow water. In this region the surface flow rapidly entrained ambient fluid as it moved outward, and the rate at which fluid was entrained with distance was greater for the radially spreading flow than for the vertical jet itself. Both the bulk and minimum time-averaged dilutions increased linearly with radial distance. The upper layer depth increased in a parabolic fashion with radial distance, consistent with previous studies of mixing layers. The composite Froude number decreased gradually from its high initial values, but was never less than one through the entire radial extent in which measurements were made. Thus, for the range of conditions of this study the flow remained internally supercritical (on a time-averaged basis). This was also true for the stability Froude number, indicating that the radial flow was unstable and entrainment occurred throughout the radial extent investigated.

No internal hydraulic jumps were found in the radially spreading surface flow in the present study. Significant entrainment into the radially spreading surface flow was found. The entrainment velocity was found to be proportional to the velocity difference between the upper and lower layers at larger radius where the radial flow had become established. The entrainment hypothesis of Morton, Taylor and Turner (1956) was consistent with the measured behaviour of the radially spreading surface flow in the present study.

## Table of Contents

<b>Abstract</b>		<b>ii</b>
<b>List of Tables</b>		<b>vii</b>
<b>List of Figures</b>		<b>viii</b>
<b>Acknowledgments</b>		<b>xii</b>
<b>1. Introduction</b>		<b>1</b>
<b>2. Review of Jets and Plumes</b>		<b>5</b>
2.1 Important Parameters .....		5
2.1.1 Jets.....		5
2.1.2 Pure Jets .....		8
2.1.3 Pure Plumes .....		11
2.1.4 Buoyant Jets .....		11
<b>3. Review of Literature Relevant to Radially Spreading Surface Flows</b>		<b>14</b>
3.1 Stratified Flows .....		14
3.1.1 Governing Parameters of Stratified Flows .....		14
3.1.2 Principles of Stratified Flows.....		18
3.2 Entrainment and Mixing .....		21
3.2.1 Mechanisms of Entrainment .....		21
3.2.2 Entrainment Hypothesis.....		23
3.3 Previous Investigations of Radially Spreading Jets .....		25
3.3.1 Introduction.....		25

3.3.2	Important Parameters .....	25
3.3.3	Flow Regions of Vertical Buoyant Jets.....	27
3.3.4	Density Jump Model Studies .....	28
3.3.4.1	Lee & Jirka (1981).....	29
3.3.4.2	Wright et al. (1991).....	32
3.3.5	Flow Visualization Studies .....	34
3.3.5.1	MacLatchy (1993).....	34
3.3.5.2	Fisher (1995).....	37
3.3.5.3	Chen (1980) .....	38
3.3.6	Synopsis and Discussion of the Different Studies .....	40
<b>4.</b>	<b>Experiments</b> .....	<b>51</b>
4.1	Introduction.....	51
4.2	Instrumentation and Equipment.....	52
4.2.1	Experimental Tank.....	52
4.2.2	Acoustic Doppler Velocimeter.....	55
4.2.3	Thermistor Array.....	57
4.3	Experiments .....	59
4.3.1	Experimental Procedure.....	61
4.4	Data Processing and Calculations.....	63
4.4.1	Velocity Data .....	63
4.4.2	Temperature Data.....	66
4.4.3	Calculated Quantities .....	66
4.4.4	Errors and Discrepancies .....	70
4.4.4.1	Kinetic Energy and Temperature Fluxes.....	71

4.4.4.2	Errors in Velocity Measurements.....	73
4.4.4.3	Errors in Temperature Measurements.....	75
4.4.4.4	Overall Error and Repeatability .....	76
4.5	Investigation of Replenishment Flows.....	78
<b>5.</b>	<b>Results and Discussion</b>	<b>92</b>
5.1	Introduction.....	92
5.2	Results.....	93
5.2.1	Dilutions.....	93
5.2.2	Upper Layer Depths .....	98
5.2.3	Velocity and Density Profiles .....	100
5.2.4	Froude Numbers.....	101
5.2.5	Bulk Richardson Numbers .....	104
5.3	Comparison to Entrainment Hypothesis .....	106
5.4	Comparison to Previous Studies.....	108
5.5	Summary of Results .....	112
<b>6.</b>	<b>Conclusions and Recommendations</b>	<b>135</b>
6.1	Conclusions.....	135
6.2	Recommendations.....	136
	<b>Notation</b>	<b>138</b>
	<b>References</b>	<b>141</b>
	<b>Appendix A: Extension of Froude Numbers to Radial Flows</b>	<b>144</b>

<b>Appendix B: Theoretical Development of Upper Layer Growth Model</b>	<b>148</b>
<b>Appendix C: Plots of Velocity Profiles for Individual Experiments</b>	<b>156</b>
<b>Appendix D: Plots of Temperature Profiles for Individual Experiments</b>	<b>164</b>

**List of Tables**

3.1. Numerical values of non-dimensional solution to velocity and tracer profiles after Chen (1980) .....	43
4.1. Details of Experiments Conducted .....	80
5.1. Comparison of results of Lee & Jirka (1981), Wright et al. (1991) and the present study.....	114

## List of Figures

Figure 2.1: Definition Sketch for pure free jets. ....	13
Figure 3.1: Generalized definition sketch for two layer flow with internal hydraulic jump. ....	44
Figure 3.2: Flow regimes in two layer flow in a channel, as described by Wilkinson & Wood (1971). ....	45
Figure 3.3: Comparison of the experiments of Lee & Jirka (1981), Wright et al. (1991), MacLatchy (1993) and Fisher (1995) by jet Froude number ( $F$ ) and depth to diameter ratio ( $H/D$ ).....	46
Figure 3.4A: Generalized definition sketch of flow regions of a vertical buoyant jet in shallow water. ....	47
Figure 3.4B: Definition sketch of flow regions of a vertical buoyant jet in shallow water, as defined by Lee & Jirka (1981).....	47
Figure 3.5: Estimated mean dilution, and stability and composite Froude numbers for assumed top-hat and triangular velocity profiles for Lee & Jirka (1981) experiment 9. ....	48
Figure 3.6: Experimental apparatus of MacLatchy (1993). ....	49
Figure 3.7: Flow visualization of radially spreading upper layer from MacLatchy (1993). ....	50
Figure 4.1: Schematic of tank and profiling mechanism. ....	81
Figure 4.2: Schematic diagrams of ADV head and thermistor array. ....	82
Figure 4.3: Comparison of the experiments of Lee & Jirka (1981), Wright et al. (1991), Fisher (1995), and the present study, by jet Froude number ( $F$ ) and depth to diameter ratio ( $H/D$ ). ....	83
Figure 4.4: Comparison of the experiments of Lee & Jirka (1981), Wright et al. (1991), Fisher (1995), and the present study, by densimetric Froude number ( $F$ ) and depth to diameter ratio ( $H/D$ ). ....	84

Figure 4.5: Definition sketch of quantities.....	85
Figure 4.6: Sample plot of velocity data from experiment B4 at R/D of 2.5 and 15 superimposed with theoretical velocity profile of Chen (1980) .....	86
Figure 4.7: Maximum velocities calculated from fitted theoretical velocity profile of Chen (1980), for all experiments. ....	87
Figure 4.8: Surface (Maximum) temperatures calculated from fitted theoretical temperature profile of Chen (1980), for all experiments. ....	88
Figure 4.9: Comparison of bulk dilution calculated by volume flux with bulk dilution calculated by temperature flux. ....	89
Figure 4.10: Plot of momentum flux discrepancy ( $m/M$ ) and measured temperature flux discrepancy ( $T_f/T_{f_0}$ ), as function of radius, averaged over all experiments. ....	90
Figure 4.11: Temperature flux discrepancy as function of square root of momentum flux discrepancy. ....	91
Figure 5.1: Time averaged mean dilution results for individual experiments (average of all replicates) as a function of non- dimensionalized trajectory length ( $Z/D$ ). ....	115
Figure 5.2: Dilution results from Hill (1972) (+), Crow and Champagne (1971) (o) and Albertson et al. (1950) (x) for the zone of flow establishment, plotted as a function of $z/D$ . ....	116
Figure 5.3: Time averaged minimum dilution results for individual experiments (average of all replicates) as a function of non- dimensionalized trajectory length ( $Z/D$ ). ....	117
Figure 5.4: $S - S_v$ plotted as a function of $R/D$ .....	118
Figure 5.5: $S_{\min} - S_v$ plotted as a function of $R/D$ .....	119
Figure 5.6: Upper layer depth plotted as a function of non-dimensionalized radius. ....	120

Figure 5.7: Non-dimensionalized upper layer depth ( $h/D$ ) plotted as a function of non-dimensionalized radius. ....	121
Figure 5.8: $\left(\frac{h-h_o}{H}\right)F^{-1/2}\left(\frac{H}{D}\right)^{1/2}$ plotted as a function of $0.10\left(\frac{R-R_o}{H}\right)+\frac{1}{2}\left(0.10\frac{R-R_o}{H}\right)^2$ .....	122
Figure 5.9: Composite plot of smoothed velocity profiles for experiment B2. ....	123
Figure 5.10: Composite plot of smoothed temperature profiles for experiment B2. ....	124
Figure 5.11: Original average upper layer velocity plotted against average upper layer velocity calculated using equations 5.5 and 5.9. ....	125
Figure 5.12: Composite Froude number as a function of non-dimensionalized radius. ....	126
Figure 5.13: Stability Froude number plotted as a function of non-dimensionalized radius. ....	127
Figure 5.14: Plot of bulk Richardson number as a function of non-dimensionalized radius. ....	128
Figure 5.15: plot of entrainment velocity ( $U_e$ ) as a function of velocity difference ( $\Delta U$ ). ....	129
Figure 5.16: Comparison of final dilution results from Lee & Jirka (1981), Lee & Jirka modified, Wright et al. (1991) and the present study. ....	130
Figure 5.17: Plot of predicted bulk dilution as a function of $R/H$ . ....	131
Figure 5.18: Plot of predicted non-dimensionalized upper layer depth ( $h/H$ ) as a function $R/H$ . ....	132
Figure 5.19: Plot of predicted Composite Froude number as a function of $R/H$ . ....	133

Figure 5.20: Plot of predicted bulk Richardson number as a function of $R/H$ . .....	134
Figure C.1: Time averaged radial velocity profiles for experiment A1 .....	157
Figure C.2: Time averaged radial velocity profiles for experiment A2 .....	158
Figure C.3: Time averaged radial velocity profiles for experiment B2 .....	159
Figure C.4: Time averaged radial velocity profiles for experiment B3 .....	160
Figure C.5: Time averaged radial velocity profiles for experiment B4 .....	161
Figure C.6: Time averaged radial velocity profiles for experiment C1 .....	162
Figure C.7: Time averaged radial velocity profiles for experiment C2 .....	163
Figure D.1 Time averaged temperature profiles for experiment A1 .....	165
Figure D.2 Time averaged temperature profiles for experiment A2.....	166
Figure D.3 Time averaged temperature profiles for experiment B2 .....	167
Figure D.4 Time averaged temperature profiles for experiment B3 .....	168
Figure D.5 Time averaged temperature profiles for experiment B4 .....	169
Figure D.6 Time averaged temperature profiles for experiment C1 .....	170
Figure D.7 Time averaged temperature profiles for experiment C2 .....	171

## Acknowledgments

For his constant encouragement and constructive supervision, I would like to thank my thesis supervisor, Dr. Greg Lawrence. Without Dr. Lawrence I would not have gotten the value from my research or accomplished the things that I have in my time as a graduate student. I would be remiss if I did not also express my thanks for the assistance and guidance that I received from the other members of my thesis committee, Dr. Michael Quick, Dr. Douw Steyn, and Dr. Rob Millar. I would also like to thank Kurt Nielson, and Scott Jackson of the Civil Engineering Hydraulics Laboratory, for the construction and later modification of the experimental apparatus used in this study, especially the two-dimensional profiling mechanism.

For preserving my sanity during critical moments of my work, I would like to particularly thank my parents and friends. Special thanks go to my two close friends Violeta Martin, for all the friendly talks and encouragement over coffee, and Stephen Marshall, for all those wild computer games played to the small hours of the morning (A great stress reliever, even if not a means to catch up on sleep!).

And so it begins.

## Chapter 1

### Introduction

Many wastewater discharges, such as pulp mill effluents and cooling water from thermal power plants, are buoyant with respect to the receiving water that they are entering. These effluents are frequently released as vertical discharges located at the bottom of shallow water bodies. Such discharges pose a concern from an environmental standpoint. Contaminants or heat may be present, with the potential for a negative impact on the receiving environment. Depending upon the location, and regulatory requirements, it is often necessary to achieve a required dilution within a certain distance of the point of discharge. In shallow water the degree of dilution will be greatly influenced by the depth available in which the jet may entrain fluid. Once surface impingement occurs radial spreading of the jet may account for additional dilution. The extent to which this additional dilution occurs will depend on such factors as the buoyancy and velocity of the effluent, and the relative proportion of the depth occupied by the surface layer. Eventually, as the distance from the discharge point increases, the initial momentum of the discharge will be of less importance, and the behavior of the flow will become plume like, and buoyancy effects will dominate.

While most real situations will involve the presence of ambient currents or multiport diffusers, the simpler case of stagnant ambient with a single port has considerable relevance, both as a fundamental case, and in situations where the ambient currents are relatively small with respect to the velocities in the radially spreading surface flow. Often multiport discharges can be modeled as originating from a single port when the individual plumes merge prior to encountering the surface. One example of a single port vertical discharge is the disposal of acid rock drainage into the deactivated, water

filled, Island Copper mine pit on northern Vancouver Island, Canada (Wilton & Lawrence (1998)).

In investigations of a radial surface buoyant jet in a circular tank, Chen (1980) found that entrainment occurred into the surface flow via the action of large scale instabilities or coherent structures. Koh (1971) reported similar behaviour while studying the discharge of a two-dimensional horizontal surface buoyant jet. As with Chen (1980), Koh observed the existence of an entrainment region where the surface flow increased in thickness due to entrainment of ambient water. Flow visualization investigations of the radially spreading surface flow emanating from a vertical buoyant jet in shallow water conducted by MacLachy (1993) and Fisher (1995) reported similar results to those above.

In contrast to these investigations, Lee & Jirka (1981) and Wright et al. (1991) have both presented models of vertical buoyant jets in shallow water accompanied by laboratory investigations to validate their models. In Lee & Jirka's case their model of the radially spreading upper layer was based on the assumption of the existence of an internal hydraulic jump. Wright et al. (1991) based their model of the transition from near-field to far-field in the radially spreading surface flow on the assumption of the existence of a density jump of the maximum entraining type, based on the definitions developed by Wilkinson & Wood (1971).

The objectives of the present study were to determine whether an internal hydraulic jump is indeed present in the radially spreading flow in proximity to the surface impingement region and to investigate the extent to which entrainment is occurring into the radially spreading flow. Of importance in determining the presence of an internal hydraulic jump was calculation of the composite Froude number, which required measurement of the velocities of both the upper and lower layers. Such velocity measurements had not previously been reported for this radial flow configuration. Velocity measurements were also necessary to properly determine the volume and tracer

fluxes in the upper layer in calculating the bulk and minimum dilutions experienced by the radial flow.

In addition the present study was intended to obtain relationships allowing the behaviour of the radially spreading flow to be predicted. These relationships cover the bulk and minimum dilutions and upper layer depth as functions of the initial jet conditions and radial distance. From these quantities other parameters can be calculated, such as the composite and stability Froude numbers and average upper layer velocities. These results were also compared to relevant theory regarding stratified flows and the entrainment hypothesis.

Basic relationships used to describe the velocity and concentration profiles, and dilution of vertical jets are presented in Chapter 2, see also Fischer et al. (1979), and List (1982). In addition, Chapter 2 also contains a discussion of the basic parameters used to characterize plumes and buoyant jets.

Chapter 3 contains a review of the basic parameters used to describe stratified flows, such as the bulk Richardson number and the composite Froude number, discusses entrainment and mixing, and introduces the entrainment hypothesis as reviewed by Turner (1986). Early works by Abraham (1965), Wilkinson & Wood (1971), Koh (1971) and Chen (1980), as well as others, provide useful background theory and investigations of jets and stratified flows.

Previous investigations of the radial surface flow associated with the discharge of a vertical buoyant jet in shallow water are also discussed in Chapter 3. In this chapter the theoretical and experimental studies of Lee & Jirka (1981) and Wright et al. (1991) are reviewed and contrasted with the results of three flow visualization studies, MacLachy (1993), Fisher (1995) and Chen (1980)

In Chapter 4, the experimental apparatus and instruments used in the present study are introduced and described, including the operation and characteristics of the primary instruments used, the acoustic Doppler velocimeter and the thermistor array. In the

experiments of this study a vertical buoyant jet was discharged in shallow water, at the center of a circular containment tank. Once the vertical jet surfaced it formed a surface layer that spread radially, and symmetrically until it reached the wall of the circular tank. Velocity and temperature profiles were made at various radii within the radially spreading surface flow. This chapter also contains a description of the experimental methodology used and discusses the calculation and analysis of important quantities, such as bulk dilution and flow-weighted mean temperature, from the experimental data. In addition Chapter 4 includes a general discussion of the error and uncertainty associated with the measurements.

The results obtained in the present study, and their significance are discussed in Chapter 5. In this chapter some predictive equations are also developed for such quantities as the upper layer depth and bulk dilution.

In Chapter 6 the conclusions and recommendations arising out of the present study are presented.

The results of this study will be of use in increasing the understanding of radially spreading surface flows caused by vertical jets in shallow water. Refinement of predictive models used to aid in the design of similar outfalls will hopefully arise out of this study.

## Chapter 2

### **Review of Jets and Plumes**

The behaviour of the radially spreading surface flow caused when a vertical buoyant jet is discharged in shallow water will be influenced by the behaviour of the vertical jet before it surfaces. The amount of dilution experienced by the vertical jet will determine the volume flux that must be accommodated in the radial flow at the outset from the surface impingement region and how buoyant this radial flow is. To understand the radially spreading flow the vertical jet region must first be understood and properly modeled. This chapter will discuss representative literature on existing knowledge of vertical buoyant jets. The reader is referred to the works by Fischer et al. (1979) or List (1981) if more detailed information is required.

A detailed discussion of literature regarding stratified flows and studies specifically involving radially spreading flows is left for the following chapter. In Chapter 3 the results of four studies, Lee & Jirka (1981), Wright et al. (1991), MacLachy (1993) and Fisher (1995), which focused on the radially spreading surface layers which result from the discharge of vertical buoyant jets in shallow water, are discussed and contrasted with each other.

#### ***2.1 Important Parameters***

A vertical buoyant jet discharged in shallow water can be separated into two distinct types of flows, a vertical jet, and a radial stratified flow. The parameters generally held to be of importance in the vertical jet flow will be discussed here.

##### **2.1.1 Jets**

The behavior of a jet or plume discharged into a fluid is governed by three general categories of parameters. These categories are: environmental, which relate to the conditions in the receiving, or ambient, fluid; geometrical, which deal with the geometric

relationship between the jet and the ambient fluid; and jet parameters which are the specific properties of the jet. Examples of environmental conditions are the density stratification, flow velocities, and degree of turbulence in the ambient fluid. Geometrical parameters of importance include the depth of submergence of the jet, angle of the jet to the horizontal, or angle of the jet to the flow in the ambient. For multiport discharges the number and spacing of the ports is also of importance. Significant jet (or plume) parameters include the jet velocity, total discharge, and the density deficit between the jet and the ambient fluid. As this study is primarily concerned with vertical buoyant jets in shallow homogeneous quiescent water, only the specific properties of the jet, and ambient depth and density, are of real relevance. The case of density stratification of the ambient receiving water is not considered here.

Making use of the definitions in Fischer et al. (1979), there are three expressions that are useful in describing the conditions in a jet:

$$\text{Volume flux,} \quad \mu = \int_A u \, dA \quad (2.1)$$

$$\text{Momentum flux,} \quad m = \int_A u^2 \, dA \quad (2.2)$$

$$\text{Buoyancy flux,} \quad \beta = \int_A g' u \, dA \quad (2.3)$$

- Where:
- A = cross sectional area of jet.
  - u = time averaged velocity in axial direction.
  - $\mu$  = specific mass flux or volume flux.
  - m = specific momentum flux.
  - $\beta$  = The specific buoyancy flux, the specific buoyant or submerged weight of the fluid passing through a cross section per unit time.
  - $g' = (\Delta\rho/\rho)g$ , effective gravitational acceleration.
  - $\Delta\rho$  = density difference between fluid and ambient.

$\rho$  = reference or ambient density.

These quantities will vary with location in the jet as fluid is entrained and velocities decrease. For purposes of determining how the jet will behave it is often more convenient to state these quantities in terms of the initial jet conditions. In terms of the initial jet conditions the equivalent expressions to equations 2. 1 to 2. 3 for a round jet are:

$$Q = \frac{\pi}{4} D^2 U_o \quad (2.4)$$

$$M = \frac{\pi}{4} D^2 U_o^2 \quad (2.5)$$

$$B = g'_o Q \quad (2.6)$$

Where:  $Q$  = initial volume flow (at jet exit).  
 $M$  = initial momentum flux.  
 $B$  = initial buoyancy flux.  
 $g'_o$  = initial effective gravitational acceleration.  
 $U_o$  = initial mean jet velocity (at nozzle).  
 $D$  = jet port diameter.

Note that these expressions are for round jets, similar expressions are possible for other jet configurations. The three initial parameters,  $Q$ ,  $M$ , and  $B$  will govern the behavior of round buoyant jets as long as the jet is fully turbulent, that is, if the jet Reynolds number is greater than about 4000 (Fischer et al, 1979). If this condition is met, other factors will have relatively little significance in determining the behavior of the jet.

Two other parameters of importance often encountered in the study of jets and buoyant jets are the regular Froude number ( $F$ ) and densimetric Froude number ( $F_o$ ):

$$F = U_o / \sqrt{gD} \quad (2.7)$$

$$F_o = U_o / \sqrt{g'_o D} \quad (2.8)$$

The regular Froude number expresses the velocity (momentum) of the jet relative to the size of the port from which the jet originates. When the regular Froude number is significantly less than 1 it has been found that the jet may not completely fill the jet nozzle, particularly when bends or expansions occur before the actual nozzle. The densimetric Froude number is similar but takes into account the density difference between the jet fluid and the ambient fluid into which it is being discharged.

There are three basic types of jets and plumes: pure jets, pure plumes and buoyant jets. A pure jet is a jet having initial momentum but no buoyancy, its density is the same as the ambient into which it is discharged, the simplest example would be the jet of water from a garden hose submerged in a bucket of water. In contrast a pure plume has no initial momentum flux, but does have initial buoyancy flux, an example would be the rising column of smoke and hot gases over a fire. The initial buoyancy is provided by the heat of the fire. A buoyant jet has both initial buoyancy and momentum, its exact characteristics depend on the relative strengths of these two quantities. An example of a buoyant jet is the cooling water discharge from a thermal power station, which has buoyancy due to heat picked up from the station and has momentum from mechanical pumping. We will now discuss the behavior, and the relationships used to describe the behavior, of pure jets, pure plumes and buoyant jets.

### **2.1.2 Pure Jets**

Upon entering the ambient fluid, a shear layer will form between the jet and the ambient fluid. The behavior of the jet may be broken into two distinct zones. Within the first zone, the shear forces generated by the interaction of the jet and the ambient fluid have not penetrated into the center of the jet, and there exists a jet core in which the velocity remains equal to the jet exit velocity. This is called the Zone of Flow Establishment (ZFE). A short distance from the jet exit, the transition distance ( $z_t$ ), approximately six to seven port diameters, the shear between the jet and the ambient has

reached the center of the jet and the velocity and concentration profiles are Gaussian. As a result, the time-averaged profiles of velocity or concentration can be expressed as a maximum value at the jet centerline, and the distance from the jet centerline. This zone is referred to as the Zone of Established Flow (ZEF), refer to figure 2.1.

The formula for the velocity distribution in the ZEF takes the form (Fischer et al., 1979):

$$u = u_c \exp[-(x/b)^2] . \quad (2.9)$$

Where  $u_c$  is the centerline (maximum) velocity,  $x$  is the distance from the centerline, and  $b$  is the characteristic width of the profile. For a pure jet a characteristic length may be defined (Fischer et al., 1979), the jet length scale :

$$l_Q = \frac{Q}{M^{0.5}} = \sqrt{A} = D\sqrt{\frac{\pi}{4}} \quad (2.10)$$

Expressions for the centerline velocity and momentum flux as functions of distance from the jet exit,  $z$ , can be derived (Fischer et al., 1979), as can expressions for the characteristic widths,  $b_w$  and  $b_t$ , of the velocity and tracer concentration profiles respectively:

$$u_c \frac{Q}{M} = 7.0 \frac{l_Q}{z} \quad (2.11)$$

$$\frac{\mu}{Q} = 0.25 \frac{z}{l_Q} \quad (2.12)$$

$$\frac{b_w}{z} = 0.107 \quad (2.13)$$

$$\frac{b_t}{z} = 0.127 \quad (2.14)$$

Where  $b_w$  = the characteristic width of the velocity profile (Gaussian).

$b_t$  = the characteristic width of the concentration or temperature profile.

Provided that  $z \gg l_0$ .

In a similar fashion, it is also possible to define the centerline concentration as a function of  $z$ , and the concentration with distance from the centerline (Fischer et al., 1979):

$$C_m/C_o = 5.64(l_0/z) \quad (2.15)$$

$$C = C_m \exp\left[-(x/b_t)^2\right] \quad (2.16)$$

As a consequence of the shear between the jet and ambient fluid, entrainment of ambient fluid into the jet will occur. In formulating an approach to the entrainment problem, Morton, Taylor and Turner (1956), proposed that the velocity of the inflowing diluting fluid be proportional to the local centerline velocity of the jet. This is the entrainment hypothesis, discussed by Turner (1986) and reviewed in the next chapter. The resulting expression for the entrainment flux is  $Q_e = 2\pi\alpha b u_c$ , where  $\alpha$  is an entrainment coefficient. Further research (List and Imberger, 1973) revealed that  $\alpha$  was not a constant, but in fact was a function of the local densimetric Froude number.

An alternate approach, and one that is more easily applied, is to assume a constant spreading angle for the jet, as proposed by Abraham (1965). With this approach the diffusion layer is assumed to spread linearly. It has been shown that the spreading angle varies by less than 10% between the extreme end cases of pure plumes and jets, while  $\alpha$  varies widely with  $F_o$  (Turner, 1986). Jirka (1975) further demonstrated that the two approaches were consistent, and the spreading angle could be related to  $\alpha$  for both the case of a jet or plume.

### 2.1.3 Pure Plumes

For a pure round plume, both the initial momentum and volume fluxes are zero. An expression for the center line vertical velocity in a plume is (Fischer et al., 1979):

$$u_c = 4.7 \frac{B^{1/3}}{z^{1/3}} \quad (2.17)$$

As the plume rises the volume flux increases from its initial value of zero to (Fischer et al., 1979):

$$\mu = 0.35B^{1/3}z^{5/3} \quad (2.18)$$

### 2.1.4 Buoyant Jets

Buoyant jets are hybrids of jets and plumes, the fluid being discharged is buoyant, but also has significant initial momentum. In addition to the length scale  $l_Q$ , used to characterize pure jets, an additional characteristic length scale is introduced for buoyant jets (Fischer et al., 1979):

$$l_M = \frac{M^{3/4}}{B^{1/2}} \quad (2.19)$$

The ratio of  $l_Q$  to  $l_M$  is the initial jet Richardson number (Fischer et al., 1979):

$$R_o = \frac{l_Q}{l_M} = \frac{QB^{1/2}}{M^{5/4}} \quad (2.20)$$

When the ratio of the jet Richardson number ( $R_o$ ) to the plume Richardson number ( $R_p = 0.557$ ) approaches or exceeds a value of approximately one half ( $R_o/R_p \geq 0.5$ ), then the buoyant jet can be considered a fully developed plume at the end of the zone of flow establishment (Fischer et al. (1979)). In a manner similar to that for pure jets, Fischer et al. (1979), presents expressions for the dilution of a buoyant jet, where:

$$\bar{\mu} = \frac{\mu}{Q} \left( \frac{R_o}{R_p} \right) \quad (2.21)$$

$$\zeta = c_p \left( \frac{z}{l_Q} \right) \left( \frac{R_o}{R_p} \right) \quad (2.22)$$

Where  $c_p = 0.254$ , the plume growth coefficient, and  $\zeta$  = dimensionless distance from jet orifice. The buoyant jet volume flux ( $\bar{\mu}$ ) becomes (Fischer et al., 1979):

$$\bar{\mu} = \zeta \quad \zeta \ll 1 \quad (2.23)$$

$$\bar{\mu} = \zeta^{5/3} \quad \zeta \gg 1 \quad (2.24)$$

It is interesting to note that all buoyant jets will eventually become plumes, once they have traveled a great enough distance. The determining parameter for whether a buoyant jet behaves as a plume, or as a jet, is the ratio of  $z$  to  $l_M$ . If  $z \gg l_M$  then the buoyant jet will behave as a plume, conversely if  $z \ll l_M$  then the buoyant jet will retain its jet like behavior (Fischer et al., 1979). Also, if  $l_Q$  and  $l_M$  are of the same order, the buoyant jet will become plume like very close to the jet exit (Fischer et al., 1979).

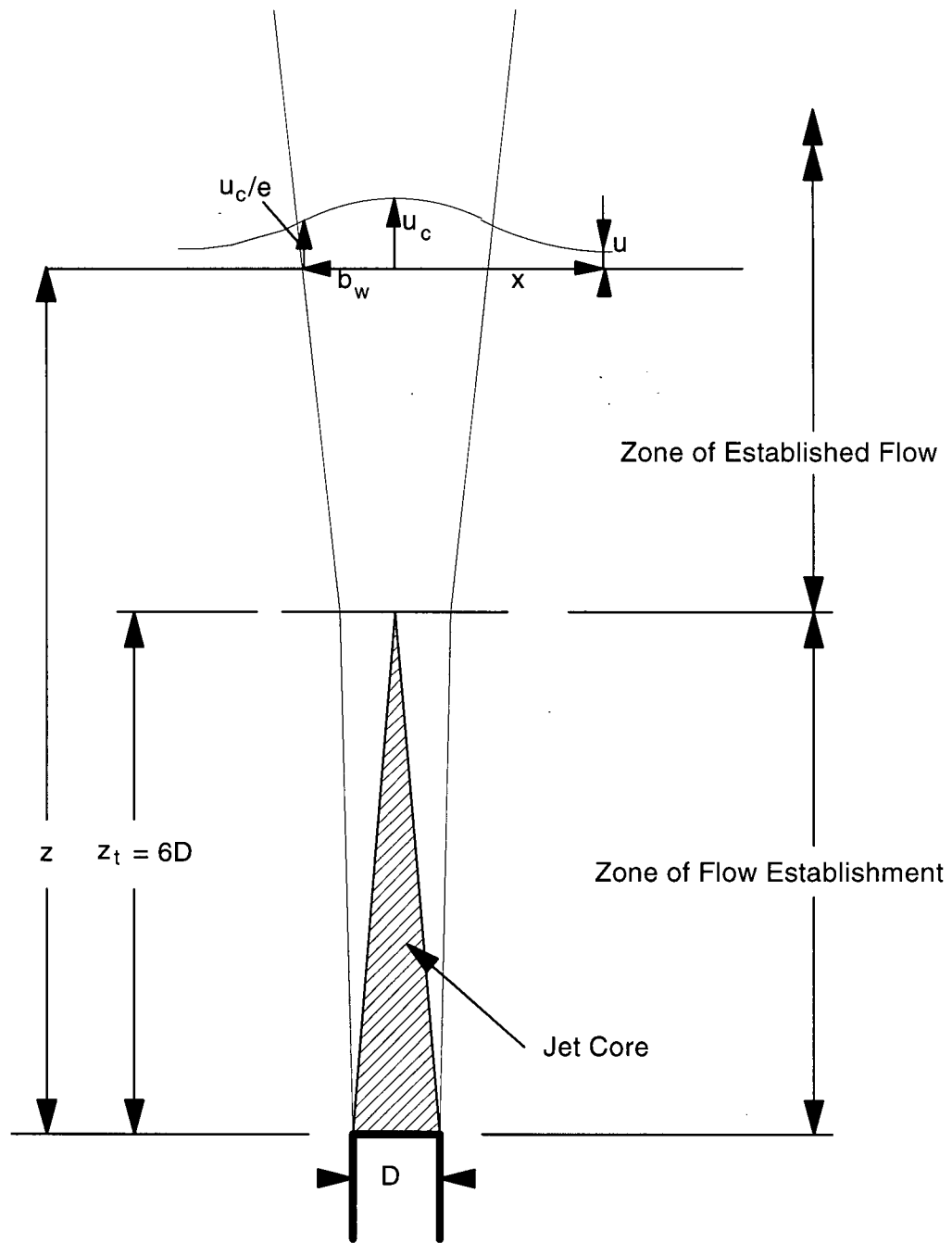


Figure 2.1 : Definition Sketch for pure free jets.

## Chapter 3

### Review of Literature Relevant to Radially Spreading Surface Flows

#### 3.1 Stratified Flows

##### 3.1.1 Governing Parameters of Stratified Flows

For stratified flows the main parameters of importance are the Richardson number and the Composite Froude number and its components. The Richardson number can take on a variety of forms though, depending upon the nature of the flow being considered (Turner, 1973; Christodoulou, 1986). For the type of flow of interest in this study the two forms of Richardson number applicable are the gradient Richardson number,  $Ri_g$ , and the bulk Richardson number,  $Ri_b$ . The gradient Richardson number is used primarily for the case of a continuously stratified fluid and is defined as:

$$Ri_g = -g \frac{\partial \rho}{\partial z} / \rho \left( \frac{\partial u}{\partial z} \right)^2 = \left( \frac{N}{S} \right)^2 \quad (3.1)$$

Where:  $\frac{\partial \rho}{\partial z}$  = density gradient in the vertical direction  
 $\frac{\partial u}{\partial z}$  = horizontal velocity gradient in the vertical direction

(velocity shear).

$N$  = Brunt Vaisälä (buoyancy) frequency

$$= \sqrt{(g/\rho) \partial \rho / \partial z}$$

$S$  =  $\partial u / \partial z$  = Velocity shear

By making use of the Boussinesq approximation and a characteristic length scale ( $L$ ) and velocity scale ( $U$ ), of the flow, we can define a generalized bulk (or overall) Richardson number for a layered system (Christodoulou, 1986):

$$Ri_b = g'L/U^2 \quad (3.2)$$

The length and velocity scales employed in equation 3.2 are not unique and many different formulations are possible, with corresponding different critical values (Christodoulou, 1986). In considering the case of a counter flowing upper and lower layer the shear between the two layers will be dependent upon the velocity difference between the two layers,  $\Delta U = U_U - U_L$ . Where  $U_U$  and  $U_L$  are the average velocities of the upper and lower layers respectively. The characteristic length scale will be the depth of the upper layer,  $h$ . Using these quantities results in the following form of bulk Richardson number (Turner, 1973):

$$Ri_b = g'h/(\Delta U)^2 \quad (3.3)$$

The Richardson number expresses the relative importance of the buoyancy forces, that tend to stabilize a stratified flow, and the shear forces arising from the velocity difference, that will tend to cause the flow to become unstable. In general as the Richardson number decreases, particularly when much less than one, a stratified flow will tend to become more unstable (Christodoulou, 1986; Turner, 1973), while Richardson numbers greater than one indicate a flow with a stable interface. Some caution is warranted however as the particular formulation of Richardson number used, e.g. gradient or bulk, and in the case of the bulk Richardson number, which values are used for the characteristic length and velocity scales, will effect what value of Richardson number is critical in determining the onset of stability or instability (Turner, 1973). For bulk Richardson numbers  $\gg 1$  a stratified flow is considered to be very stable, while when  $\ll 1$  the flow is considered to be very unstable (Turner, 1973; Christodoulou 1986). A specific value of bulk Richardson number often considered to be the critical value between stability and instability is of the order of 0.3 (Turner, 1973; Lawrence et al., 1991). For the gradient Richardson number the demarcation between stable and unstable flow is usually taken to be approximately 0.25 (Miles, 1963; Turner, 1973; Christodoulou, 1986).

The composite Froude number ( $G^2$ ) is used to indicate whether a stratified flow is internally supercritical, critical or subcritical in nature (Armi, 1986; Lawrence, 1990). These conditions refer to whether the flow is moving faster than the speed of an interfacial wave (internally supercritical,  $G^2 > 1$ ), the same speed as a wave on the interface (internally critical,  $G^2 = 1$ ), or internally subcritical, where the flow is moving slower than the interfacial wave speed ( $G^2 < 1$ ). The composite Froude number depends on the upper and lower layer densimetric Froude numbers,  $F_U = U_U / \sqrt{g'h}$  and  $F_L = U_L / \sqrt{g'(H-h)}$  (Lawrence, 1990), and is expressed as:

$$G^2 = F_U^2 + F_L^2 - \varepsilon F_U^2 F_L^2 \quad (3.4)$$

Where  $\varepsilon = \Delta\rho/\rho$ , the density difference ratio between layers. When the density difference is small ( $\varepsilon < 0.01$ ), and the Boussinesq approximation appropriate, the composite Froude number simplifies to:

$$G^2 = \frac{U_U^2}{g'h} + \frac{U_L^2}{g'(H-h)} \quad (3.5)$$

Where  $U_U$ ,  $U_L$  are the average velocities in the upper and lower layer respectively, and  $h$ ,  $H-h$  are the corresponding upper and lower layer depths.  $H$  is the total depth and is usually constant. Refer to figure 3.1 for a generalized definition sketch of a two layer flow. The reduced gravitational acceleration ( $g'$ ) is based on the density difference between the two layers.

The conditions of internally critical, sub or supercritical flow are similar to the concepts of wave speed and sub and supercritical flow in a single layer open channel flow. With internally supercritical flow, internal long waves are blocked from traveling along the interface (Lawrence, 1990), much as surface waves are prevented from traveling upstream in single layer supercritical flow. Again in a manner similar to that found in single layer flows, the transition from internally supercritical conditions to internally

subcritical conditions occurs through an internal hydraulic jump, the dominant layer suddenly increases in thickness and slows down (Lawrence, 1990). The other layer must decrease in thickness and increase in velocity to accommodate this change.

Lawrence (1990) demonstrated that the composite Froude number can be calculated from three other Froude numbers, the stability Froude number ( $F_{\Delta}$ ), the internal Froude number ( $F_I$ ), and the external Froude number ( $F_E$ ),

$$F_{\Delta}^2 = \frac{\Delta U^2}{g'H} \quad (3.6)$$

$$F_I = \frac{U_U(H-h) + U_L h}{\sqrt{g'h(H-h)H(1-F_{\Delta}^2)}} \quad (3.7)$$

$$F_E = \frac{\tilde{U}}{\sqrt{gH}} \quad (3.8)$$

Where  $\tilde{U} = (U_U h + U_L(H-h))/H$ , the flow weighted mean velocity.

Using these components the formulation for the composite Froude number is (Lawrence, 1990):

$$(1-G^2) = (1-F_{\Delta}^2)(1-F_E^2)(1-F_I^2) \quad (3.9)$$

The external Froude number is the Froude number of the two layer flow as a whole, considering it as if it were a single layer with the velocity equal to the weighted average of the velocities of both layers. In the present study the external Froude number is small and will be neglected.

The stability Froude number can be considered an inverse of the overall Richardson number of both layers of the system, it indicates the stability of internal long waves on the interface, essentially when less than 1 the long waves are stable, when greater than 1 the long waves are unstable (Lawrence, 1990). When the stability Froude

number is greater than 1 the internal Froude number is complex (Lawrence, 1990). Such a condition would indicate that internal long waves are unstable and the principles of internal hydraulic theory may no longer be applicable. So while it is mathematically still possible to calculate the composite Froude number using equation 3.5, the physical meaning of the composite Froude number where  $F_{\Delta}^2 > 1$  is uncertain.

The equations discussed above are directly applicable to planar two layer flows. These equations are shown to be valid for two layer radial flows in Appendix A. A discussion of the equations of motion as applied to two layer radial flows is used to extend the Froude numbers discussed above to two layer radial flows.

### **3.1.2. Principles of Stratified Flows**

In a fundamental work on the effect of imposed controls on stratified flows, Wilkinson & Wood (1971) examined the form that a density jump took as the height of a sill at the end of a long channel was varied, refer to figure 3.2. The experimental apparatus was a long channel with a reservoir at its end, filled with a liquid. A denser liquid was discharged into the bottom of this channel, and allowed to flow down the channel and spill into another reservoir. The lighter upper fluid was either largely stationary or, if significant entrainment into the denser fluid was occurring, was flowing in the opposite direction to that of the lower denser layer.

Wilkinson & Wood (1971) identified two possible physical features within the two layer flow density jump. In the first of these features, termed an entrainment region, there existed interfacial shear that caused interfacial instabilities, and therefore entrainment, to occur. The second feature was a roller region in which there was a reverse flow near the interface with the ambient fluid, and interfacial shear was considerably lower, a rapid increase in the depth of, and slowing of, the faster lower layer accompanied this feature. Entrainment into the roller region was negligible. The roller region could be considered an internal hydraulic jump, while the entrainment region

would be considered an entraining shear layer. These two features could occur separately or in combination, depending upon the extent of downstream control imposed. Either or both of these features together were considered to be forms of a “density jump” as termed by Wilkinson & Wood (1971).

This terminology has subsequently given rise to some confusion, as the term “density jump” is occasionally used interchangeably with the term “internal hydraulic jump”, see Wright et al (1991), though according to the definitions of Wilkinson & Wood (1971) an internal hydraulic jump is a subtype of a “density jump” and the two expressions are not equivalent. Also, an entraining shear layer could be considered an entirely different feature than an internal hydraulic jump. The confusion associated with differences in terminology will be discussed further later in this chapter.

Of importance is Wilkinson & Wood's (1971) observations of how and when entraining shear and roller regions occurred as the degree of downstream control was varied. In the absence of a downstream control only an entrainment region was found to be present in the stratified flow. In order for a roller region (internal hydraulic jump) to exist, Wilkinson & Wood (1971) determined that it was necessary for a downstream control such as a weir, sill, or channel constriction, to be present. The greater the control that was exerted, the less the extent of the entrainment region, with the roller region being pushed farther upstream. If the downstream control, such as weir height, were increased beyond a certain point, it was found that the entrainment zone ceased to exist, further increases in the sill height resulted in the density jump being forced farther and farther upstream. Eventually the density jump would inundate the outlet for the dense fluid and the density jump itself would be drowned.

Similar work involving stratified flow in a long narrow channel was undertaken by Lawrence (1985), who investigated the occurrence of internal hydraulic jumps, and associated mixing downstream of sills placed in a channel. Both layers of fluid were flowing in the same direction, but when a sill was placed in the channel a velocity

difference between the two layers was created, and an internal hydraulic jump was observed. When the flume was free from obstacles, the flow lacked an internal hydraulic jump, and there was no significant entrainment occurring. Internal hydraulic jumps were only present when the sill was present in the channel, and would form downstream of the obstacle. Often shear instabilities, of the Kelvin-Helmholtz type, were observed on the interface in the approach to the internal hydraulic jumps. These instabilities resulted in entrainment of fluid into the faster moving layer.

Koop & Browand (1979) also investigated the entrainment and mixing that occurred at a density interface in a two layer flow in a long channel, in the absence of sills or other obstacles. In their experiments both layers were flowing in the same direction, though with a velocity difference. As for Lawrence (1985), they did not observe the presence of an internal hydraulic jump in the channel. Instead, interfacial instabilities, in the form of vortices, initiated at the entrance to the channel. As these vortices moved down the channel they grew in size, and merged. At some point in the channel the instabilities reached a maximum size. When this occurred the instabilities collapsed into a stable interface, with only small instabilities present, the turbulence generated by these large scale instabilities having been dissipated.

Koop & Browand (1979) reason that the large scale structures are critical in the formation and maintenance of turbulence. The statically stable conditions arising from the density difference resulted in the ultimate destruction of the turbulence generated. Koop & Browand (1979) provide an explanation as to why the collapse of the vortex structures occurs. As a vortex grows, it lifts denser fluid into the lighter upper layer, and depresses lighter fluid into the denser lower layer. As vortex size increases, it requires greater energy to accomplish this, eventually there will be insufficient energy to overcome buoyancy, and the turbulent structure collapses.

In studying the discharge of a horizontal surface buoyant jet, Koh (1971), observed the existence of an entrainment region immediately after the jet exit. In this

region ambient fluid is entrained into the surface jet, which grows in thickness. This transition was modeled as occurring when the Richardson number of the flow reached a critical value, and the turbulent entrainment collapsed under the influence of buoyancy.

Similar results were reported by Chen (1980). Experiments with a radial surface buoyant jet in a circular tank produced a region of flow with increasing thickness, and entrainment occurring, until at a distance equal to the momentum length scale defined by  $M$  and  $B$  ( $l_M = M^{3/4}/B^{1/2}$ , equation 2.19), the entrainment structure collapsed, and the radial jet became a radial plume. From this point outward, until the spreading radial plume contacted the walls of the experimental tank, the radial plume was of constant depth. It is interesting to note that Chen (1980) also observed that once the jet had contacted the walls, the surface layer increased in thickness due to the flow being blocked. This resulted in the entrainment zone being "drowned" and an internal hydraulic jump appeared to form, and is comparable to an imposed downstream control as reported by Wilkinson & Wood (1971).

To what extent entrainment occurs, and the physical manifestation of this entrainment, depends entirely on the stability of the interface between the two layers, usually expressed in one form or other of the Richardson number. Christodoulou (1986) has summarized the results of many investigations of stratified flows. He reports that when the bulk Richardson number,  $R_b$ , is less than one, entrainment and mixing on the interface occurs in the form of large energetic vortices, that engulf and then mix fluid into the more active layer, which grows in thickness. The smaller the bulk Richardson number the larger and more energetic the vortices. When the bulk Richardson number is greater than one, but still relatively small, entrainment is slower and may occur through the action of cusp type (Holmboe) instabilities (Christodoulou, 1986). At very large bulk Richardson numbers (large buoyancy forces relative to shear) shear instabilities are suppressed and no turbulent entrainment occurs.

## **3.2 Entrainment and Mixing**

### **3.2.1 Mechanisms of Entrainment**

In both jets and stratified shear flows, entrainment and mixing of fluid into the flow occurs through the action of large scale structures (instabilities), often termed coherent structures, and small scale turbulence. A stratified shear flow is a flow that has a variation or gradient in velocity perpendicular to the mean flow and a density stratification. The velocity variation gives rise to shear forces in the fluid. Entrainment of fluid in shear flows is dominated by the action of the large scale turbulence structures, often termed coherent structures. These coherent structures, in the form of vortices or eddies, are known to be common in many turbulent flows (Ho & Heurre, 1984). It is the engulfing process associated with the rolling up of vortex structures that accomplishes most of the entrainment of fluid into the dominant layer (Turner, 1986). The mixing of that entrained fluid with the dominant layer fluid, i.e. where the two fluids are actually blended together, is accomplished by small scale turbulence and diffusion. The two processes are clearly separate in their effect, entrainment by large scale structures, and mixing by small scale processes (Turner, 1986).

Large scale eddies grow linearly as they move downstream (White, 1991). A large scale eddy will continue the process of growing, stretching and entraining ambient fluid until its turbulent kinetic energy (TKE) has been dissipated to such an extent that it no longer has the energy to maintain its structure. The eddy will then collapse and be dragged back into the bulk jet, and the process repeats itself. As the jet progresses farther downstream the largest scale of eddies increase in size but are less energetic. Eventually turbulent kinetic energy has been entirely dissipated and the jet has become a laminar plume or has become completely dissipated into the ambient at very large distances.

Tso et. al. (1981) found that in the self preserving region of a circular jet the large scale eddies or coherent structures were of a size on the order of the local jet diameter. It

is also possible for eddies to overtake preceding eddies and merge with them, larger slower moving eddies result from such a merging.

Turbulent flows have significantly greater entrainment and mixing rates than do laminar flow, this is due to the occurrence and action of these large eddies (Turner, 1986). The entrainment rate of a jet is dependent on the size of the large scale eddies (Turner, 1986). These structures increase the available surface area on which the smaller scales of turbulence can act to transfer and disperse vorticity and TKE, and ultimately mix ambient fluid into the jet. For this reason they are an important mechanism in the dilution that occurs in a jet, and account for the ultimate dissipation of the jet and its momentum and TKE.

### 3.2.2 Entrainment Hypothesis

The classic entrainment hypothesis states that mean inflow velocity across the edge of a turbulent flow is directly proportional to some characteristic velocity of the turbulent flow. This characteristic velocity could be the maximum local time averaged velocity, for example the centerline velocity of a vertical jet, as in Morton et al. (1956), or some other quantity, such as the spatial average of velocity over the section of the turbulent flow (Turner, 1986). Jirka (1975) has demonstrated that the linear growth of jets is consistent with the entrainment hypothesis. The constant of proportionality of the entrainment relationship will vary depending upon the characteristic velocity employed to describe the turbulent flow. The final form of the relationship is also dependent upon such factors as the geometry of the turbulent flow and other properties, and the density difference in the case of a stratified flow (Turner, 1986). The general relationship can be expressed as follows:

$$U_e = \frac{\partial \mu}{\partial L} = \alpha U_c \quad (3.10)$$

The change in volume flux with respect to some distance ( $\partial\mu/\partial L$ ), is the local inflow velocity per unit area ( $U_e$ ), and is a function of the local characteristic velocity ( $U_c$ ) multiplied by a proportionality constant ( $\alpha$ ). For stratified flows the entrainment hypothesis can be modified to account for the velocity difference between the two layers and becomes (Turner, 1986):

$$U_e = \alpha\Delta U \quad (3.11)$$

As was discussed in the previous section, the most important mechanism of entrainment into turbulent flows is via the engulfment of external fluid that occurs as large scale turbulent eddies grow at the edge of a jet or plume. Similarity assumptions imply that these large eddies retain the same relationship with the mean flow whatever the actual scale of the motion, and the amount of small scale turbulent energy is relatively unimportant (Turner, 1986). Thus the most physically important parameter is the characteristic velocity, as long as the largest scales of turbulent motion scale with this characteristic velocity then the entrainment velocity will do so as well (Turner, 1986).

Similar to the entrainment hypothesis of Turner (1986) is the relation between the growth of the mixing layer and the velocity ratio on a sheared density interface between two layers of differing velocity and density. The mixing layer is the region between the layers of a stratified flow in which there is a high degree of velocity shear and mixing of the fluid from the two layers. Ho & Heurre (1984) had stated that the growth of the mixed layer (with downstream distance) in stratified free shear flows can be shown to be dependent upon the velocity ratio:

$$\frac{dh}{dx} = c \frac{\Delta U}{2\bar{U}} \quad (3.12)$$

Where  $\Delta U = U_u + |U_l|$  and is the velocity difference between the two layers while  $\bar{U} = (U_u + |U_l|)/2$  and is the average velocity between the two layers and

represents the mean convective speed of instabilities in the mixing layer. In mixing layers the constant  $c$  is on the order of 0.14 (Lawrence et al., 1991).

### **3.3 Previous Investigations of Radially Spreading Jets**

#### **3.3.1 Introduction**

There are two, somewhat conflicting, views of the nature of the radially spreading surface flow. Some investigators have proposed that a radial internal hydraulic jump or density jump is present in the radially spreading surface flow and that the transition from momentum to buoyancy dominated conditions occurs through such a jump. Other investigators have adopted an entraining shear layer for the model of the radially spreading surface flow. Representative of the internal hydraulic jump or density jump approach are the papers by Lee & Jirka (1981) and Wright et al. (1991), though there is some evolution in the approach apparent between these two papers. Lee & Jirka's (1981) model limits entrainment to the radially spreading surface flow before the internal hydraulic jump occurs. Wright et al. (1991) model entrainment into the radially spreading surface flow but their model is built around the existence of a density jump. The entraining shear layer model is supported by the flow visualization experiments of MacLachy (1993) and Fisher (1995). The jet Froude number and depth to diameter ratio for each of the experiments in these four studies are plotted in figure 3.3 for comparative purposes. Chen (1980) conducted a theoretical and experimental investigation of radially spreading surface flows which reported results similar to MacLachy (1993) and Fisher (1995).

#### **3.3.2 Important Parameters**

When discharged in shallow water, the behaviour of a vertical jet can be described by three basic parameters. The first parameter of importance is the Reynolds number of the jet, that indicates whether the jet is turbulent or laminar in nature. In the present study all experiments used jets that were fully turbulent within the nozzle. All experiments of

Lee & Jirka (1981) and Wright et al. (1991) were also fully turbulent from the outset. Some experiments of Fisher (1995) used Reynolds numbers small enough that they may have initiated as laminar jets, but because of shear between the jet and surrounding fluid they would quickly have become turbulent (White, 1991). If the jet Reynolds number is high enough to ensure turbulent conditions there is no further effect upon the large scale instabilities and entrainment with increasing Reynolds number (White, 1991).

An important factor influencing the behavior of the radially spreading surface flow is the depth of water into which the jet is discharged, particularly relevant is the magnitude of the total water depth relative to the size of the jet port. This relative proportion is expressed in the depth to jet port diameter ratio,  $H/D$  (Lee & Jirka, 1981). The depth to diameter ratio determines the amount of dilution that the vertical jet experiences prior to entering the surface impingement region, and hence the initial volume flux in the radially spreading flow. Also vertical jet characteristics change with distance from the jet port, for instance in the change from the zone of flow establishment to the zone of established flow. Also, with sufficiently deep water the buoyant jet will become plume like (Lee & Jirka, 1981). The depth to diameter ratio may also be important as an indication of how confined the radial inner flow in the lower layer is. Because the inward flow in the lower layer is induced by entrainment into both the vertical jet and radially spreading regions, at smaller  $H/D$  there may be interference between the vertical and radial jet regions, and increased shear between the two layers.

An additional parameter of importance is the densimetric Froude number ( $F_o$ ), that expresses the strength (momentum) of the jet relative to its buoyancy (Lee & Jirka, 1981). This quantity is potentially of importance in determining the depth of the radially spreading flow and how quickly the upper layer depth increases (Lee & Jirka, 1981). In combination with the depth to diameter ratio ( $H/D$ ) the densimetric Froude number indicates the stability of the radial flow in the vicinity of the surface impingement region. Under unstable conditions a recirculating region is formed in the vicinity of the vertical

jet instead of a stable spreading surface layer, and the jet fluid is drawn down and re-entrained into the vertical jet. This is referred to as an unstable condition by Lee & Jirka (1981), the criteria they provide for this occurring is when  $F_o > 4.6(H/D)$ .

### **3.3.3 Flow Regions of Vertical Buoyant Jets**

All four of the studies listed above identify four distinct regions of flow associated with a vertical buoyant jet discharged in shallow water. All four studies employ different names for these four regions, here they will be referred to as, the vertical buoyant jet region, surface impingement region, radially spreading buoyant jet region and the radial buoyant plume region. Refer to figure 3.4A for a schematic representation of these regions. The first three regions comprise the near field (momentum dominated), and the last region makes up the far field (buoyancy dominated). The basic characteristics of these four regions, as much as is agreed on by the four studies, are discussed below.

#### **Buoyant Vertical Jet Region**

In this region the vertical buoyant jet entrains ambient fluid as it moves toward the surface. Where the jet enters the surface impingement region, the velocity and density profiles are often assumed to have become self similar (Gaussian) if the water depth is greater than the zone of flow establishment, or about six port diameters (Lee & Jirka, 1981).

#### **Surface Impingement Region.**

Within this region, the vertical flow of the buoyant jet is redirected to a horizontal radially spreading flow. A surface boil, or fountain, is associated with this region (Lee & Jirka, 1981; Wright et al., 1991). There is assumed to be intense turbulent mixing, but no entrainment, within this region (Lee & Jirka, 1981). This is assumed since the surface impingement region is bounded completely by the vertical buoyant jet and radial internal hydraulic jump region and has no interface with the ambient fluid. At the point where the

flow exits from the surface impingement region, the velocity profile is usually assumed to be half-Gaussian, as in Lee & Jirka (1981), Wright et al (1991) and Fisher (1995).

### **Radial Buoyant Jet Region**

It is in this region that real contention arises as to what flow configuration exists and what the most appropriate form of model to use. There have been two main approaches to this region. One approach is that a radial internal hydraulic jump is present, where the radially flowing upper layer suddenly slows down and increases in depth (Lee & Jirka, 1981). The second possibility is that there is an entraining shear layer where ambient fluid is gradually entrained and mixed with the upper layer that becomes deeper and increasingly diluted as it moves outward (Wright et al., 1991).

### **Radial Buoyant Plume Region**

This region is made up of the buoyant upper layer flowing outward from the source and the denser ambient fluid of the lower layer flowing inward to the vertical buoyant jet. Velocities are relatively low, and entrainment across the interface of the two layers is often considered negligible (Lee & Jirka, 1981; Wright et al., 1991).

#### **3.3.4 Density Jump Model Studies**

Two papers have concentrated primarily on developing predictive models of the dilution and thickness at the exit from a density jump in the radially spreading flow. The first of these papers is Lee & Jirka (1981) and the later paper is Wright et al (1991). These papers are representative of most of the existing literature relating to radially spreading surface flows emanating from vertical buoyant jets in shallow water. While other papers certainly exist, many of them draw heavily on the results of Lee & Jirka (1981) and/or are earlier developments of the model and results presented in Wright et al. (1991). Two of these intermediate studies are Wright (1985) and Wright and Bühler (1986).

### 3.3.4.1 Lee & Jirka (1981)

The study by Lee & Jirka (1981) on shallow water jets has formed the basis for later work by many researchers. As part of their study, Lee & Jirka (1981) examined shallow water jets over a wide range of flow conditions. Experimental studies were carried out on semicircular vertical buoyant wall jets with densimetric Froude numbers ( $F_o = U/(g'D)^{1/2}$ ) ranging from 8 to 583 as quoted by Lee & Jirka (1981). Depths used in the study were between 6 and 35 port diameters, and jet Reynolds numbers were sufficiently high for all runs to ensure fully turbulent conditions. Similar to the general flow configuration discussed above, Lee & Jirka have broken their model down into four regions, they term the third region to be a radial internal hydraulic jump, the specifics of which are discussed below, refer to figure 3.4B.

In the radial internal hydraulic jump region the surface flow is presumed to pass from a supercritical flow to a subcritical flow via a (radial) internal hydraulic jump. There is assumed to be an abrupt increase in upper layer thickness, and an energy loss, associated with the radial internal hydraulic jump. Lee & Jirka assume that this region has a distinct interface with constant conditions in both layers. Based on hydraulic theory for two-layer flows and internal hydraulic jumps, Lee & Jirka (1981) were able to develop expressions for estimating the conjugate layer depths upstream and downstream of the internal hydraulic jump.

An alternate configuration is possible when the vertical jet has low buoyancy relative to momentum (large  $F_o$ ), combined with shallow water. Under these conditions a recirculating region is formed in the vicinity of the vertical jet instead of a stable spreading surface layer, and the jet fluid is drawn down and re-entrained into the vertical jet. This is referred to as an unstable condition by Lee & Jirka (1981), the criteria they provide for this occurring is when  $F_o > 4.6(H/D)$ . However, the unstable configuration with associated upper layer re-circulation in the immediate vicinity of the vertical jet is not a direct concern of the present study.

It should be noted that in Lee & Jirka's (1981) formulation they allowed for the existence of a radial buoyant surface jet in the short distance before the toe of the radial internal hydraulic jump, with the radial jump starting at a radius of approximately 60% of the total depth. Entrainment into this radial surface buoyant jet was allowed for. However, because this region was very limited in extent the degree of entrainment assumed to occur is not large. This minor region is not attributed an identity of its own in Lee & Jirka's (1981) formulation. There was assumed to be no entrainment into the radial internal hydraulic jump itself that extends from  $0.6 R/H$  to  $2-3 R/H$ . This arrangement conforms very well to the classic definition of an internal hydraulic jump. Presumably if these properties of an internal hydraulic jump are present they would also be accompanied by a rapid change in the composite Froude number from internally super-critical ( $>1$ ) to internally sub-critical ( $<1$ ) conditions.

Central to Lee & Jirka's (1981) approach to the problem of vertical buoyant jets in shallow water, was the assumption that the transition from near-field to far-field conditions occurred by means of an internal hydraulic jump. In Lee & Jirka's experiments the buoyant upper layer spilled out of the experimental tank through slotted weirs covered with horse hair matting. This may have choked the upper layer flow and provided a downstream control inducing an internal hydraulic jump, if one was observed. Also, the use of a half wall jet, where the visible portion of the radial flow was occurring along a transparent wall, may have altered visible flow conditions due to wall friction effects.

Finally, despite their assumptions as to the presence of an internal hydraulic jump in the radially spreading surface flow, Lee & Jirka (1981) provided no direct evidence that one was present in their experiments. No velocity measurements were reported to verify that there were conditions of internally supercritical and internally subcritical flow upstream and downstream of the supposed location of the internal hydraulic jump, nor does their paper contain any flow visualization of the upper layer flow.

In Lee & Jirka's (1981) own figure 9A they provided a scale diagram of the interface profile with radius and temperature profiles at certain intervals for their experiment 9 ( $H/D = 11.1$ ,  $F = 7$ ,  $Fo = 108.5$ ). It is possible to use this information to calculate the composite and stability Froude numbers and dilutions for these locations in the radial flow, from  $0.38 R/H$  to  $6.5 R/H$ . As they do not provide velocity profiles it is necessary to assume a velocity profile and solve for the velocity in such a way that there is conservation of temperature flux when the velocity profile is integrated over depth with the temperature profiles provided. Two different velocity profiles were assumed, top-hat and triangular. One discrepancy that should be noted is that the densimetric Froude number that Lee & Jirka (1981) quote for experiment 9 is 46, when calculated from the parameters quoted a value of 108.5 is obtained. The corrected value is used in the present study when referring to Lee & Jirka's experiment 9, this was the only experiment where this error was found.

The composite and stability Froude numbers estimated for experiment 9 of Lee & Jirka (1981) are plotted in figure 3.5. Note that the composite Froude number is very large ( $\gg 1$ ) until  $R/H > 3$ , and the flow remains internally super-critical out to large radii. There is some uncertainty associated with the calculation since it was derived from assumed velocity profiles and has an anomaly where the composite Froude number first decreases around  $R/H = 3$  and then increases slightly. However, it is still clear that in the region in which Lee & Jirka (1981) assume a radial internal hydraulic jump ( $0.6 R/H$  to  $2-3 R/H$ ) and well beyond it, the flow is internally super-critical.

Similar to the results for the composite Froude number, the stability Froude number also starts out very large and gradually decreases, but is still greater than 1 at  $6.5 R/H$ . For an unstable interface, as indicated by the high stability Froude number, it is reasonable to expect that there would be entrainment into the radially spreading surface flow beyond the point where Lee & Jirka (1981) had assumed that it would cease, at  $0.6 R/H$ . This is supported by the calculated dilution that increases for radii up to  $6.5 R/H$  and

is also plotted in figure 3.5. There is a small discrepancy with the calculated bulk dilution that appears to decrease slightly in the vicinity of 3 to 4  $R/H$  but this likely arises from the assumptions and approximation that were used to calculate it from Lee & Jirka's figure.

#### **3.3.4.2 Wright et al. (1991)**

A modification of the approach of Lee & Jirka (1981) is presented in Wright et al. (1991). In their model, it was assumed that the place of the radial internal hydraulic jump is taken by a radial "density jump" of the maximum entraining type, as described by Wilkinson & Wood (1971). Thus, the model of Wright et al. (1991) assumes the existence of entrainment into the surface layer and hence results in greater dilution than that that would occur if entrainment were confined to the vertical buoyant jet alone, essentially as Lee & Jirka (1981) did.

Unfortunately, Wright et al. (1991) use the term internal hydraulic jump and density jump interchangeably, which creates confusion as to just what structure they assumed to be present. As was discussed in the review of Wilkinson & Wood (1971), a density jump with a roller region would be considered an internal hydraulic jump, but a density jump of the maximum entraining type would not, it is an entraining shear layer. Yet Wright et al. (1991) state that the "density jump" that they assume to be present is of "the maximum entraining type", with internally critical flow conditions at its exit. This would not be consistent with an internal hydraulic jump as such. This confusion could be minimized if the term "density jump of the maximum entraining type" were instead replaced with "entraining shear flow" whenever the former expression appears in Wright et al. (1991) and other studies that make use of Wilkinson & Wood (1971).

The experiments of Wright et al (1991) had depth to diameter ratios ranging from 20 to in excess of 100, with jet Froude numbers from 2 to 10. Densimetric Froude numbers varied from 2 to almost 10000. Two series of experiments were conducted, one with a negatively buoyant jet the other with a positively buoyant jet.

Wright et al. (1991) assumed that the flow exiting the density jump is internally critical. This assumption has the advantage of allowing the equations of Wright et al.'s model to be more easily solved, since the form and degree of downstream control could be ignored (Wright et al, 1991), and was probably adopted for this reason. Lacking velocity measurements, it is not clear whether this is actually valid for the real situation or is merely an expedient measure. It was noted by Wright et al. (1991) that their model was most sensitive to the length of the density jump. The length of the density jump was assumed to depend primarily on water depth and extended from  $0.135H$  to  $3H$ . Wright et al. (1991) found that the dilution that had occurred by the "end" of the radial density jump increased by a factor of 3 to 5 times the dilution in the vertical jet.

The mathematical formulation employed in the model by Wright et al. (1991) reflect an internal hydraulic jump type approach to the radially spreading surface layer, rather than an entrainment hypothesis based one, that would be based on gradient or bulk Richardson Numbers and some characteristic velocity of the flow. The total entrainment was arrived at indirectly by equating the momentum at the entrance and exit to the density jump, assuming a constant upper layer growth rate and internally critical conditions at the exit from the density jump.

While Wright et al. (1991) conducted a series of some 65 experiments, no flow visualization was included in their study. Only one photograph, taken from above the flow, is provided. The occurrence of "ring vortices" that propagated outward from the surface impingement region were described. They were observed to grow larger with increasing distance from the surface impingement region until they collapsed at the end of the mixing zone. Wright et al reported that initially no organized structure was apparent in the surface jet and the turbulent fluctuations had a relatively high frequency and large amplitude. Also Wright et al reported at larger distances the smaller, higher frequency disturbances had died out, leaving large scale structures with periods on the order of 1 second. Wright et al. noted that the presence of ambient fluid all the way to the surface

indicated that these “ring vortices” occupied the entire depth of the upper layer flow. Wright et al. (1991) did note that as a result of the presence of these structures the use of time averaged concentration and velocity profiles does not provide an accurate description of local conditions at any given time.

### **3.3.5 Flow Visualization Studies**

By using flow visualization techniques, there have been studies that have attempted to identify what actually occurs in the radially spreading regions exiting from the surface impingement region. Two of these, though covering somewhat different flow conditions and depth ratios ( $H/D$ ), have observed surprisingly similar structures and flow development. The first, MacLatchy (1993), used laser induced fluorescence to observe and identify the visible structures in the radially spreading flow, and was primarily a qualitative study. The second study, that of Fisher (1995), also used flow visualization techniques, actually measured dilutions in the radially spreading flow, as well as observations of flow structures and details. The qualitative observations are of primary interest in this discussion.

#### **3.3.5.1 MacLatchy (1993)**

Using a shallow round tank, and different jet nozzles to allow different  $H/D$  ratios, MacLatchy (1993) investigated the radially spreading surface flows emanating from a thermally buoyant vertical jet in both very shallow water ( $H/D = 5$ ), and shallow ( $H/D$  of 7.5 and 15) water. Jet Froude number ranged from 0.5 to 2, while densimetric Froude numbers varied from 2 to 20.

In order to simulate an infinite ambient and provide for entrainment of ambient fluid by the jet, the ambient (cold) water was replenished by a diffuser manifold located along the bottom inside wall of the circular tank. The radially spreading surface layer spilled out of the circular tank upon reaching the wall of the tank, that exerted a local control on the surface flow, but not an internal control on the stratified flow as a whole.

The circular tank was constructed from clear Plexiglas and was 0.3 m deep by 1.8 m in diameter, giving a diameter to depth aspect ratio of 3. The circular tank was contained within a larger square tank (2m by 2m by 0.45m deep) to contain the overflow and facilitate flow visualization by allowing viewing through a straight flat surface. A schematic of the experimental apparatus is provided in figure 3.6.

Flow visualization was accomplished with sodium fluorescein dye injected into the jet discharge line by a small peristaltic dosing pump with a flow range of 0.01 to 1 l/s. Flow illumination was provided by a 4 Watt argon ion laser, with the laser sheet produced by an resonant scanning mirror controlled by a function generator. Image recording was done with both a 35 mm still camera, and video camera, under dark room conditions.

Photographs of the surface flow for an experiment with  $F=2$ ,  $F_o = 50$ , and  $H/D = 15$ , are presented in Figure 3.7. Large scale interfacial instabilities, vortex cells, visible as the brightest areas, are apparent starting from the exit from the surface impingement zone at the left. Ambient (darker) fluid can be seen intruding almost to the free surface between the vortex cells. As the cells move outward (to the right), they grow in size. The translation of vortex cells can be seen in the movement of features **a** and **b** in the sequential photographs. Feature **c** is a wisp of upper layer fluid caught between the surface flow and the underlying inward flow, and as a result, it does not move significantly over the sequence of photos.

At any given instant, a distinct, uniform surface layer did not exist in the near-field. The thickness of the upper layer varied constantly as vortices would form, grow while moving outward, and collapse. In addition, examination of the video recordings revealed that the vortices or billows tended to merge with increasing radial distance.

First hand observations and review of the video recordings revealed that the larger ring vortices in the radially spreading flow originated from the vortices or billows formed in the interfacial regions of the vertical buoyant jet. Billows in the vertical jet could be clearly seen to travel upward into the surface impingement region, to then emerge in the

radial flow. The billows were continuous in nature from the vertical to the radial flow. This phenomena is most readily apparent when the actual motion can be observed.

To investigate the possibility that the ambient replenishment flow might be affecting the upper layer flow, the replenishment flow was varied for some experiments, and the effect observed. The flow structure in the upper layer did not change appreciably with the variation in ambient flow rate. The only significant effect of the lower ambient flow rates was that the dye concentration in the ambient increased more quickly than with the other experiments, with the result that these experiments were of shorter duration than when the ambient replenishment flows were adjusted to meet entrainment requirements. At the walls of the circular tank a portion of the flow was drawn down and back toward the vertical jet by the need to compensate for the deficit in ambient flow for entrainment. Since the portion deflected back by the circular wall was still slightly buoyant with respect to the ambient fluid, it tended to exist as a partial third layer between the radially spreading surface buoyant jet and the ambient. As this intermediate flow approached the center of the tank it tended to disappear due to entrainment into the upper layer, and mixing into the ambient fluid.

When large scale re-circulation did occur at the wall, it was due to the inadequacy of the ambient fluid replenishment flows from the ring diffuser. The entrainment demands of the radially spreading upper layer were satisfied by drawing upper layer fluid down into the lower layer at the circular weir, to eventually be re-entrained back into the upper layer flow. This effect was not one of an internal control imposed by the circular weir, but one that arose because there was not an infinite ambient from which large entrainment flows could be drawn.

MacLatchy (1993) also conducted some investigation of the flow produced when no replenishment was provided and the jet fluid was allowed to build up at the walls of the tank. These experiments were referred to as choked experiments. Without the replenishment flows a build up of dyed fluid was observed at the walls, as in the cases

where replenishment flow was limited it tended to form an intermediate layer that moved inward toward the center. Because of entrainment demands some of this fluid was recirculated through the tank as the cold water was consumed. Eventually flow visualization became impossible because of this dye build up, but no internal hydraulic jumps were observed before any of the choked experiments ceased.

### **3.3.5.2 Fisher (1995)**

The study by Fisher (1995) was primarily intended to investigate and measure the dilution that occurs in both the vertical and radial regions of a jet discharged in a finite depth. This was accomplished by using flow visualization techniques to measure the intensity of laser induced fluorescence of dye contained within the jet fluid and from this determine dilutions at different locations within both the radial and vertical regions. Like Wright et al. (1991), Fisher (1995) found dramatically increased dilutions near the end of the “density jump”, again by factors of from 3 to 5 over that in the vertical jet. As with Wright et al. (1991), Fisher refers to the entraining region of the radial jet as a “density jump”.

Fisher utilized a tank with an effective depth of 75.5 cm with a negatively buoyant jet discharged downward to a raised rectangular surface within the tank. The nozzle diameter was 7.67 cm, giving a depth to diameter ratio of approximately 93. The extent of the raised surface allowed observations of the radial flow to an aspect ratio ( $R/H$ ) of 1.6, in the long dimension of the surface, which is less than the assumed length of density jump of Wright et al. of  $3 R/H$ .

Of greatest interest is the two flow visualization experiments that Fisher (1995) conducted to investigate conditions in the radially spreading region. These experiments used regular jet Froude numbers of 0.58 ( a laminar plume) and 2.15 (turbulent jet) with densimetric Froude numbers of 3.48 and 12.46 respectively. The depth to diameter ratio

used was much greater than those of MacLatchy (1993), the other jet parameters are similar in magnitude.

Despite the different depth ratios of the two studies the observed flow details in the radial region are strikingly similar to those of MacLatchy (1993). Fisher (1995) describes the occurrence of intermittent pulses of jet fluid entering the radial flow from the surface impingement region, these pulses travel outward and grow in size. The pulses of jet fluid tended to curl up to form rotating eddies behind their heads. Occasionally faster moving pulses of fluid would overtake and merge with slower moving cells or eddies, Fisher (1995) describes intense mixing as occurring. Fisher (1995) also alludes to the possibility that the pulses of jet fluid emerging into the radial flow are continuations of pulses observed in the radial plume or jet, but could not identify the continuation of these structures from the vertical to the radial region with certainty.

Fisher (1995) describes the flow structure as being an axisymmetric surface jet that entrains fluid, gradually this entraining jet thickens and slows. As part of the entrainment process the internal Froude number is presumed to approach unity, as this is not supported by velocity data it is not clear how this was determined from the dilution data available, or whether it is merely a restatement of the assumptions of Wright et al (1991). Consistent with the conceptual model of Wright et al. (1991), Fisher (1995) continues to term this flow structure an internal hydraulic jump or density jump, of the maximum entraining form. Fisher (1995) further explicitly states that an abrupt increase in upper layer depth and slowing in velocity of the radial flow (an internal hydraulic jump) was not observed, as Lee & Jirka (1981) had based their approach on.

### **3.3.5.3 Chen (1980)**

Chen's study examined a wide range of gravitational spreading currents. One of the configurations investigated was that of a jet discharged radially at the surface. As such

it differs somewhat from the focus of this study where the jet originates as a vertical discharge which then spreads radially once it has encountered the surface.

Entrainment into the radially spreading surface flow was also reported by Chen (1980). Large scale entrainment structures, similar to those reported by MacLachy (1993) and Fisher (1995) were present. The upper layer grew in thickness until, at large radial distances (approximately equal to the momentum length scale) the entrainment structure collapsed, and the radial jet became a radial plume. From this point outward, until the spreading radial plume contacted the walls of the experimental tank, the radial plume was of constant depth.

Chen (1980) developed a theoretical model for the shape of the velocity and tracer concentration profiles. In his theoretical development Chen (1980) assumed that the ambient water was infinitely deep and hence, that there was no return flow in the lower layer. Using the equations of motion (radial momentum and continuity) and Prandtl-Tollmien's assumptions for the mixing length and eddy viscosity a self similar distribution was developed for the velocity and tracer profiles (Appendix B contains a more detailed review of the development of Chen's theoretical model). Chen presented a numerical solution for the shape of the profile, as a function of the dimensionless similarity variable for the depth ( $\xi$ ):

$$\xi = az/R \quad (3.13)$$

Where  $a$  is a growth rate constant,  $z$  is the depth below the surface, and  $R$  is the radius. The formulation of  $\xi$  implies a linear growth of the profile with radial distance. The velocity or tracer concentration is then a function of the corresponding maximum (or surface) value and  $\xi$ . The solution takes the form of:

$$\frac{U(R, z)}{U_{\max}(R)} = F'(\xi), \quad \frac{\Delta T(R, z)}{\Delta T_{\max}(R)} = F'(\xi)$$

At the surface  $F'(\xi)$  is 1 and the gradient (slope) is zero. At  $\xi=2.4$ ,  $F'(\xi)$  has a value of essentially 0 and has no slope. The numerical solutions for  $F'(\xi)$  are provide in Table 3.1. A best fit, with  $R^2$  of 0.999, to the numerical values provided by Chen (1980) was found to be:

$$F'(\xi) = -0.0495\xi^4 + 0.3393\xi^3 - 0.6207\xi^2 - 0.1962\xi + 1 \quad (3.14)$$

### 3.3.6 Synopsis and Discussion of the Different Studies.

The earliest of the studies, Lee & Jirka (1981) is most closely attached to the theory of an internal hydraulic jump, an abrupt increase in upper layer thickness and slowing of the radial flow is explicitly assumed in their conceptual model. Entrainment into the radial flow is minor, and the dilution at the end of the hydraulic jump is almost the same as at the entrance to the surface impingement region from the vertical jet. The later work of Wright et al. (1991) is also based on what they term to be a density jump or internal hydraulic jump but assumes it to be of the maximum entraining type. Ambient fluid is entrained, and the surface flow becomes deeper, more diluted and slower, until the composite Froude number approaches unity, the flow then stabilizes and large scale entrainment and dilution ceases.

Fisher (1995) and MacLachy (1993) provide details of the radial flow structure based on observations from flow visualization experiments. In addition Fisher (1995) measured dilution of both the vertical and radial flows and obtained results similar to Wright et al. (1991). Fisher (1995) also utilized the same conceptual formulation as Wright et al., that of a density or internal hydraulic jump of the maximum entraining type. The flow details between Fisher (1995) and MacLachy (1993) are very similar, large scale eddies were observed to cause significant entrainment and dilution into the radially spreading layer. These eddies were observed to grow and merge as they moved outward from the surface impingement zone.

The three most recent studies are in agreement that there is significant entrainment and dilution occurring into the radially spreading surface layer. Where there is conflict between these studies is in the assumption of an internal hydraulic jump or density jump of the maximum entraining type. MacLachy (1993) argues that this is not a correct concept for the radially spreading surface layer because of its intermittent, discontinuous nature, that is not well suited to description by conventional internal hydraulic formula. Furthermore, there is not direct evidence to support the assumption that the composite Froude number converges on unity.

Classically the definition of an internal hydraulic jump has meant an abrupt change from internally supercritical to internally subcritical conditions, that results in the composite Froude number changing from greater than 1 to less than 1. Generally an internal hydraulic jump does not result in significant entrainment, only a minor degree of entrainment occurs at the toe of the jump. Wilkinson & Wood (1971) may cause some confusion by their reference to a "density jump of the maximum entraining type", that occurs when there is no topographic control on a two layer flow in a channel. This feature is missing the roller region and abrupt depth change that is usually associated with an internal hydraulic jump. It is probably misleading to refer to an entraining shear flow, where depth is gradually increasing and entrainment occurring, as any kind of jump. There is no "jumping" occurring in an entraining shear flow and the internal Froude number does not change from greater than 1 (internally supercritical) to less than 1 (internally subcritical).

A common feature of all of the above studies is the absence of any velocity measurements in the radially spreading flow. Such measurements are necessary in order to interpret how velocity profiles evolve with radial distance and whether, in fact, the composite Froude number does approach unity, a condition of internally critical flow. Such velocity measurements would also be useful in determining the bulk dilution of the flow as well as the interface depth where the velocity changes from radially outward to

radially inward. Bulk Richardson numbers could also be developed from velocity data, in concert with bulk dilutions and density, and the results compared with the entrainment hypothesis (Turner (1986)) to see how appropriate his concepts are in describing the behavior of the flow. Experiments designed to obtain velocity data in the radially spreading flow are an important part of the present study.

$\xi$	$F(\xi)$	$\xi$	$F'(\xi)$
0	1	1.3	0.3
0.1	0.979	1.4	0.249
0.2	0.94	1.5	0.2
0.3	0.897	1.6	0.165
0.4	0.842	1.7	0.125
0.5	0.782	1.8	0.095
0.6	0.721	1.9	0.067
0.7	0.66	2	0.046
0.8	0.604	2.1	0.03
0.9	0.538	2.2	0.02
1	0.474	2.3	0.009
1.1	0.411	2.4	0
1.2	0.357		

Table 3.1: Numerical values of non-dimensional solution to velocity and tracer profiles after Chen (1980)

Note: Channel controls to produce internal hydraulic jump not shown. Exchange flow velocities will be in opposing directions.

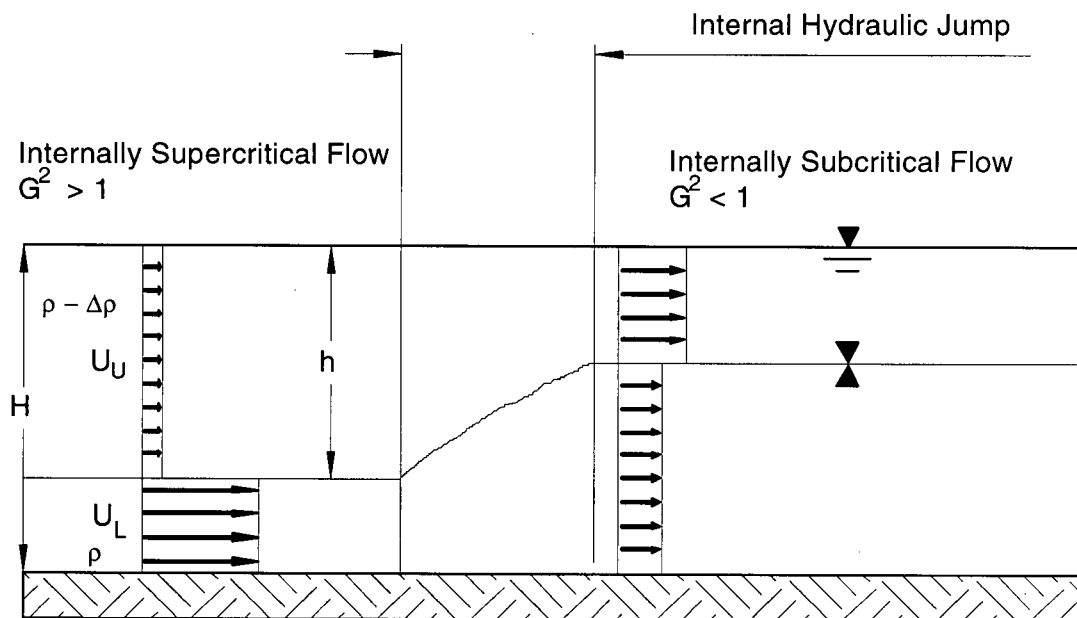


Figure 3.1: Generalized definition sketch for two layer flow with internal hydraulic jump.

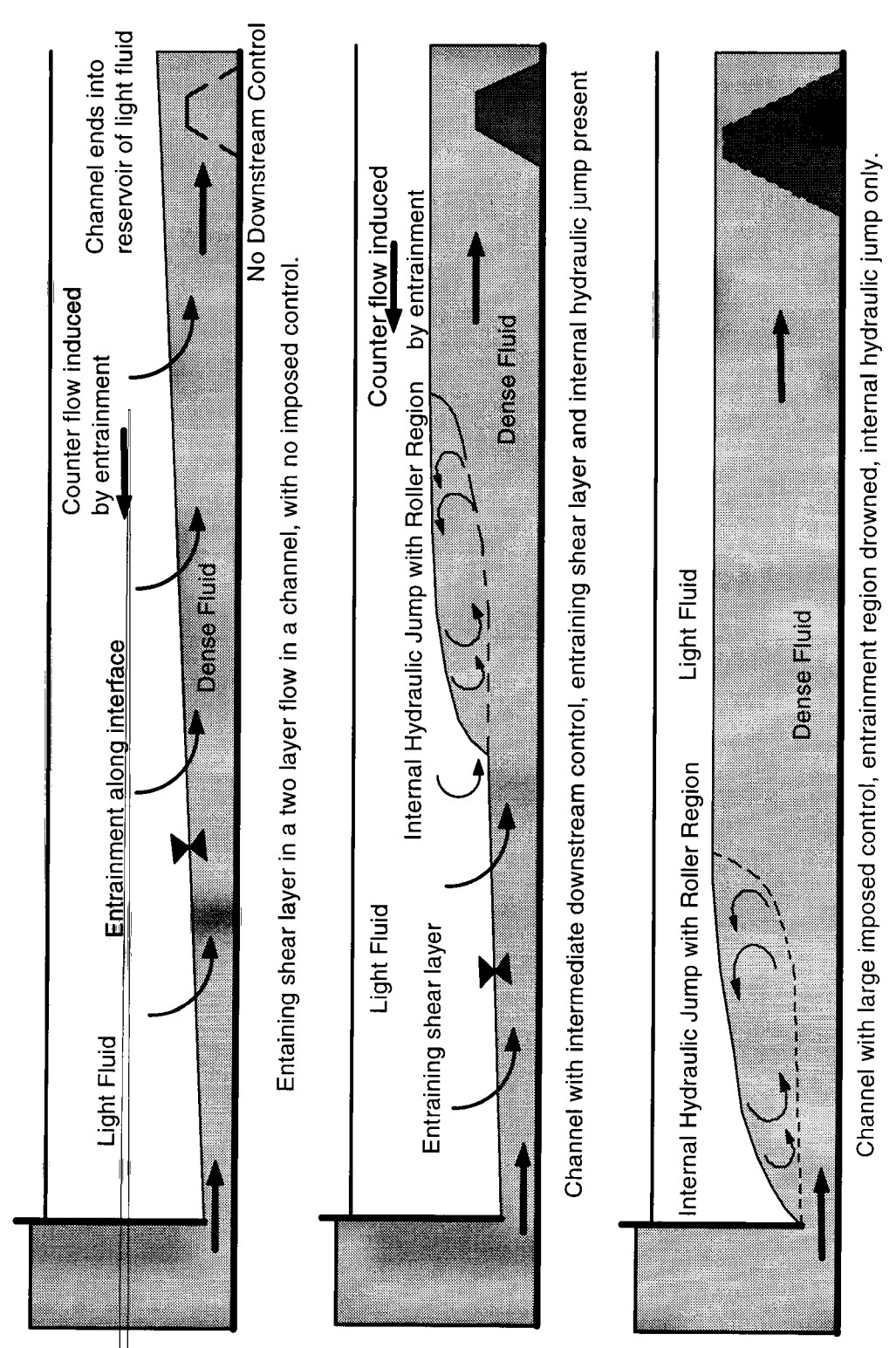


Figure 3.2: Flow regimes in two layer flow in a channel, as described by Wilkinson & Wood (1971)

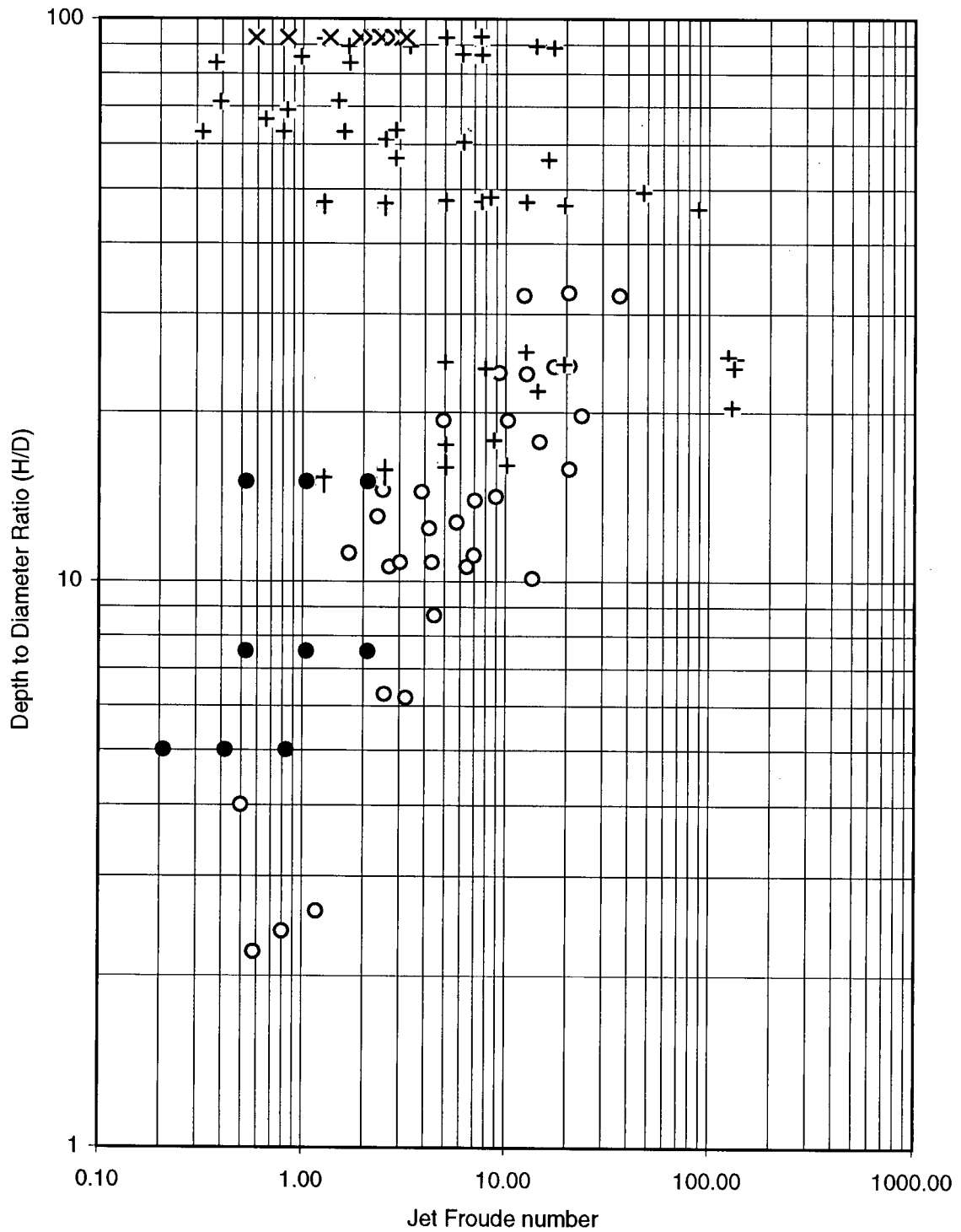


Figure 3.3: Comparison of the experiments of Lee & Jirka (1981) (o), Wright et al. (1991) (+), MacLatchy (1993) (•), and Fisher (1995) (x), by jet Froude number ( $F$ ) and depth to diameter ratio ( $H/D$ ).

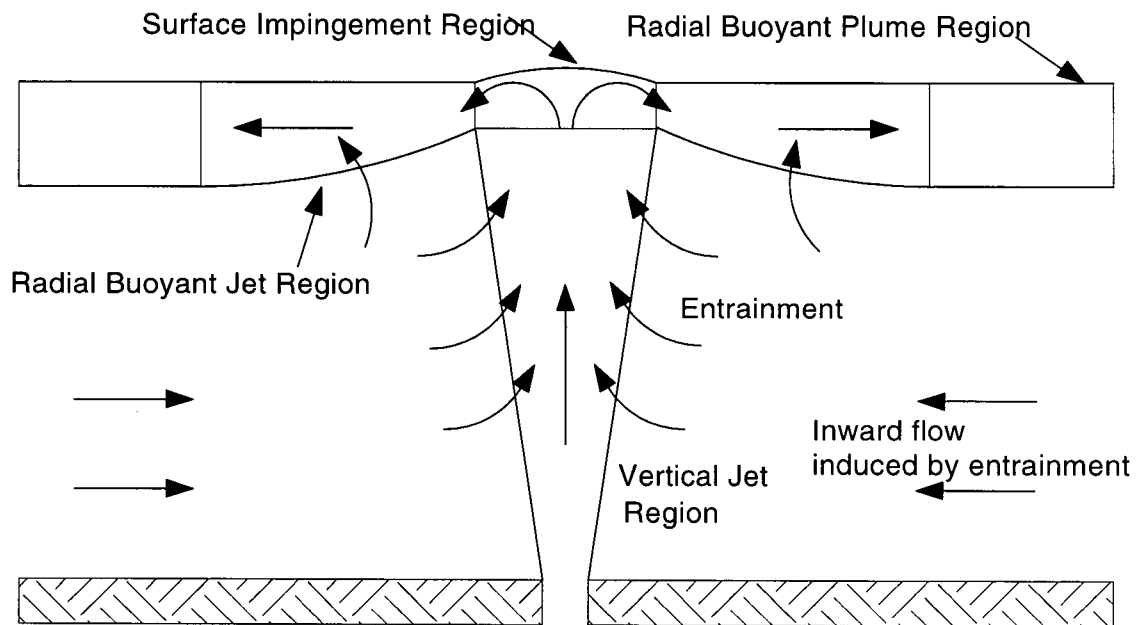


Figure 3.4A: Generalized definition sketch of flow regions of a vertical buoyant jet in shallow water.

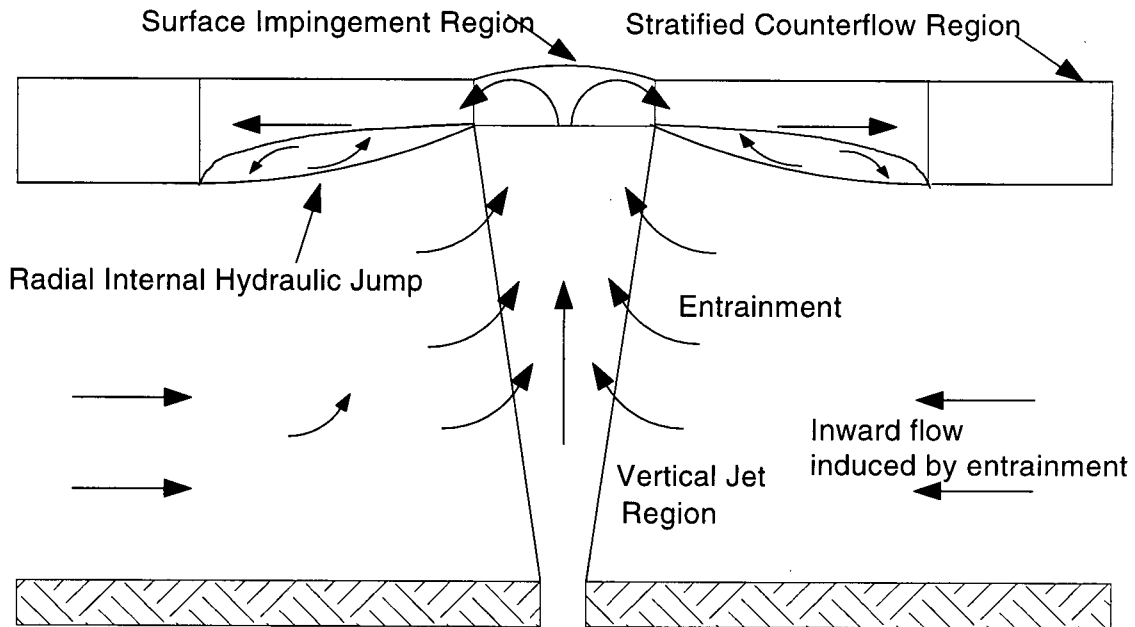


Figure 3.4B: Definition sketch of flow regions of a vertical buoyant jet in shallow water, as defined by Lee & Jirka (1981).

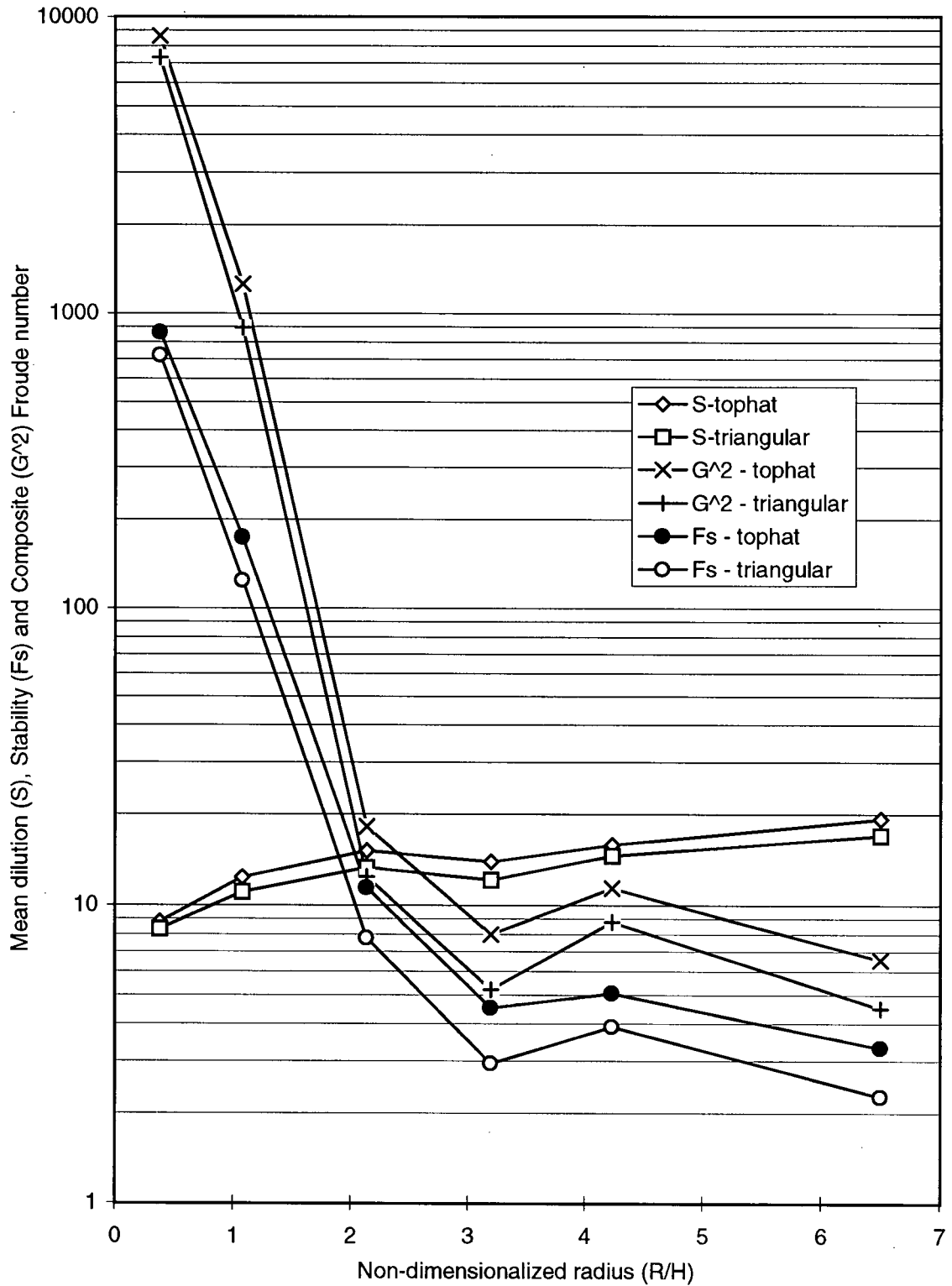


Figure 3.5: Estimated mean dilution, and stability and composite Froude numbers for assumed top-hat and triangular velocity profiles for Lee & Jirka (1981) experiment 9.

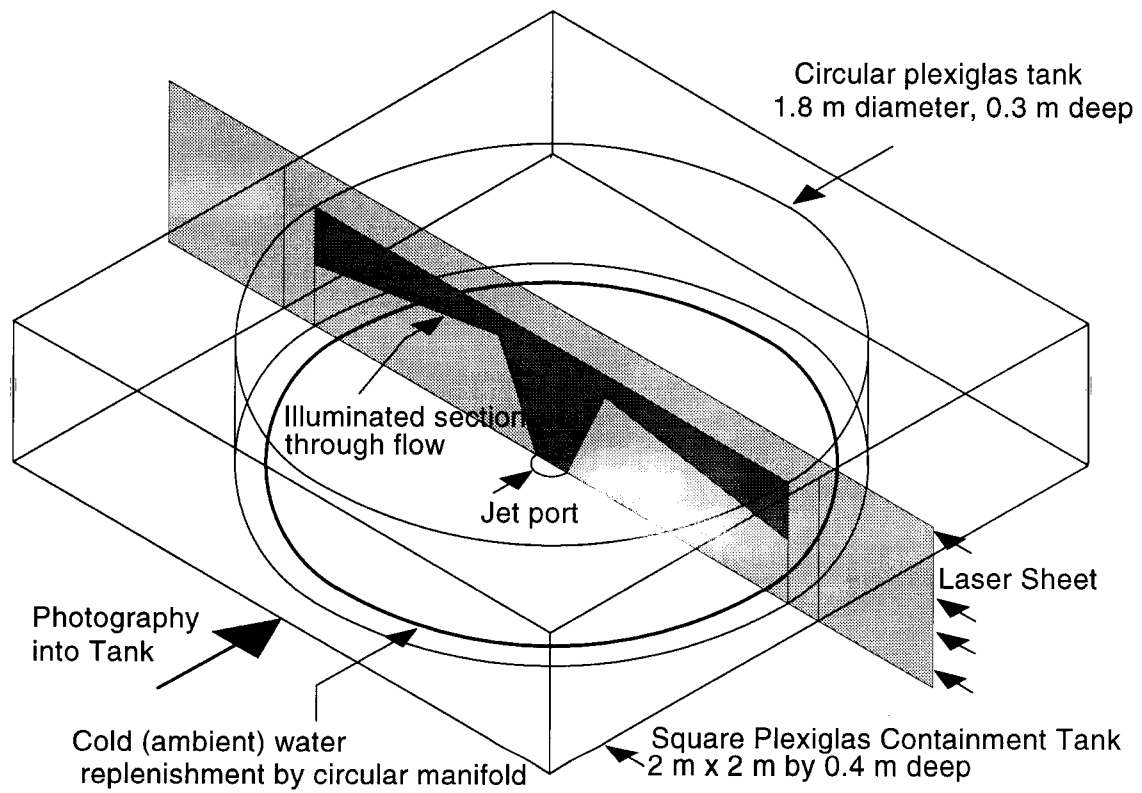


Figure 3.6. Experimental apparatus of MacLatchy (1993).

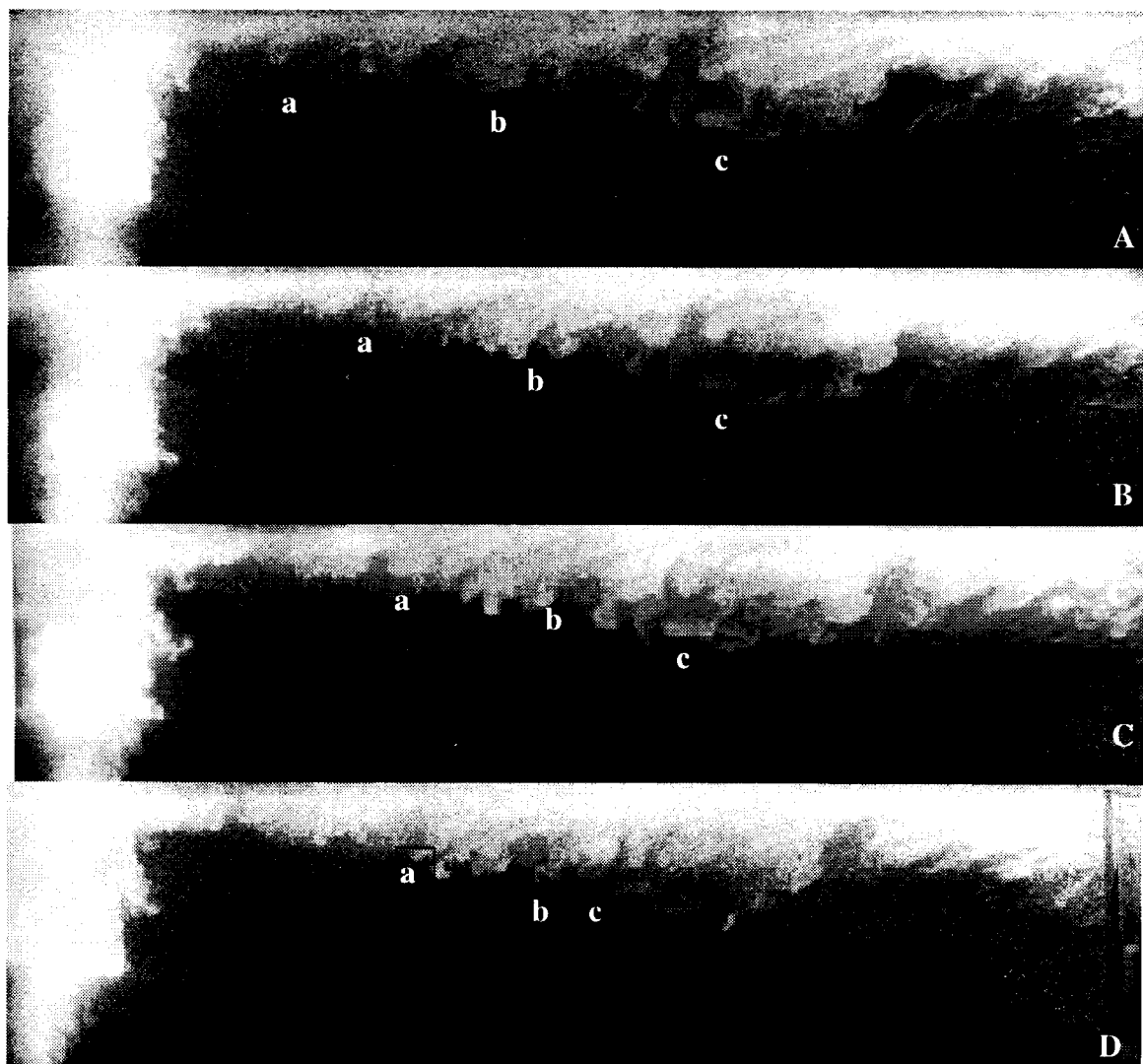


Figure 3.7: Flow visualization of radially spreading upper layer from MacLatchy (1993).  
 $F_o = 50$ ,  $F = 2$ ,  $H/D = 15$ . Time interval 0.4s, approximate scale 1.6cm = 10cm.

Captions **a** and **b** mark vortex cells that move across sequence of photographs, feature marked **c** is a wisp of fluid caught between lower and upper layer flow and consequently does not move significantly.

## Chapter 4

### Experiments

#### 4.1 Introduction

The important independent (or initial) parameters of a vertical buoyant jet discharged in shallow water are; port diameter ( $D$ ), total ambient water depth ( $H$ ), jet port velocity ( $U_o$ ), dimensionless density difference ( $\Delta\rho/\rho_o$ ), and gravity constant ( $g$ ). These parameters control the behaviour of the radially spreading flow that is expressed in the following dependent parameters; dilution ( $S$ ), and upper layer depth ( $h$ ). The dependent parameters are also functions of the radial (downstream) distance ( $R$ ). The independent parameters can be combined into the dimensionless groups of; depth to diameter ratio ( $H/D$ ), dimensionless radial distance ( $R/D$ ), jet Froude number ( $F = U_o/\sqrt{gD}$ ) and jet densimetric Froude number ( $F_o = U_o/\sqrt{g(\Delta\rho/\rho_o)D}$ ). The two dependent parameters can then be expressed as a function of these four independent dimensionless groups;  $h/D, S = f(H/D, R/D, F, F_o)$ .

The experimental strategy followed in the present study was to investigate the effect upon the upper layer depth and dilution, as functions of radial distance ( $R/D$ ), of varying the three initial parameters ( $H/D, F, F_o$ ). This was accomplished by using various jet flow rates, port diameters and density differences for a vertical jet discharged at the center of a circular tank of constant depth. From the upper layer depth and dilution such secondary parameters as the composite Froude number and bulk Richardson number may be determined. These parameters are indicative of conditions in the radially spreading surface flow.

The original scaling of the apparatus was designed to achieve as large a diameter as possible, 1.8m being the largest physically practical in the location available. The depth of the tank and jet diameters used were selected to ensure that the depth of the

surface flow was large enough to be properly measured with the instruments intended, an Acoustic Doppler Velocimeter and thermistor array (details in the following section). Actual flow rates used were a balance between desired Froude numbers and available capacities of both hot and cold water supplies.

## **4.2 Instrumentation and Equipment**

The experimental tank previously used for flow visualization by MacLatchy (1993) and described in Chapter 3, was used for both the velocity and density experiments discussed in this chapter. Additional instruments and equipment were added to take the necessary measurements. A computer controlled profiling mechanism was employed to position the Acoustic Doppler Velocimeter (ADV) and thermistor array to collect velocity and temperature data at the desired locations.

### **4.2.1 Experimental Tank**

To experimentally investigate the radially spreading upper layer, it was necessary to produce a radially spreading surface jet. This was accomplished by discharging a vertical jet upwards at the center of a circular tank (refer to figure 4.1). The circular boundary of the tank ensures symmetrical spreading of the upper layer, which is allowed to spill out of the tank at the circular wall. The circular experimental tank is situated inside a square containment tank to receive the outflow from the circular tank and to facilitate flow visualization.

Previous studies, see chapter 3, have used configurations that have not had symmetrical boundaries, have used negatively buoyant jets impinging on a solid surface, or have used half round jets placed adjacent to a solid surface. All these configurations could alter the flow behaviour from that of a radially spreading surface flow on a symmetrical free surface. The negatively buoyant jet on a solid surface, and the half-round jet adjacent to a solid boundary could expect boundary layer and friction effects to alter the velocity structure of the spreading flow. This in turn would influence

entrainment and spreading of the flow. Non-symmetrical boundaries could bias the flow in one direction more than another, a true symmetrical, radial flow might not exist.

Because the circular tank was relatively small in volume, the available ambient fluid in the tank would have been quickly depleted by entrainment into the jet. Thus a method whereby the ambient was continually recharged to replace lost fluid, and maintain steady state conditions for a long enough duration to complete each experiment, was designed. Using a cold water supply in the lab, a supply line was run through a control valve and flow meter, and then split into two lines that were connected to two diffuser like discharge tubes in the bottom outside edge of the circular tank. These diffuser tubes were installed such that they discharged straight inwards toward the vertical jet, to approximate the gross flow of the ambient fluid toward the center to replace entrained fluid. To minimize mixing created by jets from the ring diffuser, synthetic air filter material was placed over each port of the ring diffuser.

The replenishment flow also prevents a recirculated layer of mixed jet and ambient fluid from forming below the radially spreading jet and propagating inward toward the center of the tank. The flow visualization experiments discussed in chapter 3 (MacLatchy, 1993) suggest that the radially spreading flow is internally supercritical, and a continuous interface is not present. Internal long waves are thus blocked, which prevents the physical presence of the wall from having an effect upon the upper layer, beyond its immediate vicinity. The combination of these two factors allows the radial flow within the bulk of the tank to behave as if an infinite ambient were present. A local control of the free surface of the upper layer flow over the wall exists, but an internal control is not imposed.

When the replenishment flow was not provided and the surface flow was contained within the tank walls (starting water level below top of tank) the previous flow visualization study (MacLatchy, 1993) found that there was no indication of an internal hydraulic jump. Since it was not allowed to spill out of the tank the warm surface jet fluid

would build up against the tank wall. Gradually an intermediate layer of this fluid would move back toward the center of the tank and re-circulate, but the surface layer itself was still visible as a separate entity and did not contain an internal hydraulic jump. This intermediate layer formed in order to satisfy the entrainment demands of the vertical and radial jet, it was not part of the radial jet, and did not represent a roller region or other part of an internal hydraulic jump. Rather it signified the gradual replacement of the ambient, lower layer fluid by partially diluted jet fluid as the original ambient fluid was consumed by the jet.

The maximum flow rates were limited by the capacity of the water supplies in the laboratory. Most critical was the available hot water supply, that, from a 2.5 cm domestic line, was capable of supplying a maximum flow of from 2 to 2.5 l/s (30 to 37.5 USGPM) depending on other demands. Steady state water temperature varied with flow rate and range between 20°C and 45°C. Temperature of the cold water supply varied between 7°C and 14°C, with a maximum flow rate of approximately 6 l/s. Flow rates used in experiments were checked to ensure that the vertical jet was fully turbulent at the jet nozzle, that is the jet Reynold's number was greater than 4000.

To allow investigation of the effect of the ratio  $H/D$ , a series of jet nozzles of different diameters were fabricated. These nozzles were equipped with standard fittings for attachment to the circular tank and connection to the hot water line. The three jet diameters used in this investigation were 2, 4 and 6 cm, corresponding to  $H/D$  ratios of 15, 7.5 and 5 respectively.

The circular experimental tank was 30 cm deep with a diameter of 183 cm. The square containment tank was 213 cm by 213 cm by 34 cm deep. Both tanks were constructed from clear Plexiglas GM. Ball type valves were used throughout for control of the ambient recharge, jet discharge, and water levels in the square containment tank.

#### 4.2.2 Acoustic Doppler Velocimeter

To obtain velocity profiles for use in calculating flow rates, Richardson numbers, and other quantities, an instrument was needed that would minimize disturbance of the upper layer while still providing accurate point measurements of the velocity field. The instrument used was an Acoustic Doppler Velocimeter (ADV) supplied by Sontek Inc. of California. ADVs are based on the same principle as a Laser Doppler anemometer, but instead use the Doppler shift of an acoustic signal reflected off particles moving with the water in order to determine water velocity. The specific instrument used in this study was equipped with an upward looking, three dimensional head. The head had a focal length of 5 cm, and the instrument stem entered the water some 10 cm to the side of the area being measured, to keep the disturbance this caused away from the measurement volume. The signal from the instrument is focused on a sample volume approximately 4 mm in diameter and 8 mm tall, refer to figure 4.2 for a sketch of the ADV. As the ADV is capable of measuring at frequencies of up to 25 Hz it was theoretically possible to measure turbulent fluctuations in the flow. The ADV was controlled by, and data from it was stored on, a 486 laboratory computer.

As stated above, the ADV measures the three dimensional velocities in a finite volume of fluid. In order to obtain a velocity profile through the flow a series of points had to be measured. To accomplish this the ADV was mounted to a mechanical traversing mechanism that could position the ADV both vertically and horizontally in a vertical plane on the centerline of the experimental tank. This mechanism operates by way of vertically and horizontally mounted screw shafts, each driven by a computer controlled stepper motor, and moves in the same plane as the flow visualization described in chapter 3 (MacLatchy, 1993). The mechanism could position the ADV with an accuracy of 1 mm each way both horizontally and vertically. After the required quantity (1500 samples for stable averages) of velocity data had been acquired at a point in the profile the ADV was moved to the next point, and data acquisition was repeated.

Each velocity profile was composed of 22 points with 20 of these points concentrated in the upper part of the tank. These uppermost 20 points were spaced vertically at intervals of 5 mm, starting at a depth of 5 mm and proceeding downward. Due to the disruption of the ADV signal by the water surface it could not measure closer than 5 mm to the surface of the water. Thus, a depth range of 5 mm to 100 mm was intensively measured. The area below this was well below the region of interest in the upper layer and consequently only 2 more points were placed in this lower region at depths of 135 mm and 210 mm. Because of the physical configuration of the ADV, measurements could not be made at any greater depth.

There were a minimum of 5 vertical profiles in each experiment, experiments with smaller jet diameters had more vertical profiles, as the profiles were located in multiples of the jet diameters. For A series experiments ( $D = 6$  cm) vertical profiles were measured at distances of 2.5, 4, 6, 8, and 10  $R/D$ . B series experiments ( $D = 4$  cm) had vertical profiles located at 2.5, 4, 6, 8, 10 and 15  $R/D$  from the center of the tank. C series experiments ( $D = 2$  cm) profiles were located at 4, 6, 8, 10, 15, 20 and 25 port diameters downstream from the tank centerline.

The functioning and accuracy of the ADV was verified by testing the instrument in the large experimental flume in the Civil Engineering Hydraulics Laboratory at UBC. Two different flow rates were used and the measurements of the ADV were compared to those provided by a propeller type current meter. Unfortunately, this was only able to verify the accuracy of the ADV to within 20%, as the propeller meter was much less accurate than the ADV and could not provide any better indication of the ADV's capabilities. The ADV was well immersed in the flow in the flume, it is possible the ADV's accuracy is reduced when working in proximity to a free surface with wave action, since the movement of the free surface may scatter or distort the sound waves emanating from the upward looking ADV head. This behaviour was observed during data acquisition in proximity to the free surface during the present study.

The ADV calculates two quantities to determine how well it is working. The first is the signal to noise ratio (SNR) that provides an indication of how strong the measurement signal is to background noise. Sontek recommends a minimum SNR of 15 decibels for measuring turbulent fluctuations, in the present study SNRs were always well above 25db. The second quantity is the correlation coefficient that indicates the degree to which the velocity measurements fluctuate with time. Sontek recommends that the correlation coefficient not drop below 70% or increased error will be encountered with the measured velocities. The correlation coefficients did frequently drop below 70% when operating in proximity to the moving free surface. This is more fully discussed later in this section.

#### **4.2.3 Thermistor Array**

Temperature data used for calculation of dilutions and density profiles was obtained using a vertical array of 13 thermistors. As with the ADV measurements the majority of temperature measurements were taken in proximity to the upper layer. The first eleven thermistors, at the top of the array, were spaced at vertical intervals of 0.5 cm, to match the locations at which velocity measurements were taken. The next two thermistors were spaced at intervals of 7.5 cm below the upper ones, to acquire temperature data in the lower layer of the tank. This arrangement allowed temperature data to be acquired in the same locations as those at which the ADV had collected velocity data. A schematic of the thermistor array is included in Figure 4.2.

In order to collect data at the same points at which velocity data was collected with the ADV, the thermistor array was used in two separate vertical positions in each profile to cover a greater depth. First the array was positioned close to the surface to collect the upper portion of the profile, after which it was repositioned deeper in the tank to fill out the profile and cover the remaining points measured with the ADV. This

actually provided more measurement points than with the ADV, the extra points were omitted during data processing to ease calculation of quantities involving both data sets.

Thermistors with an e-folding time of 0.1 seconds (time for the thermistor to respond to  $1/e$  of a change in temperature) and capable of a resolution of  $0.1^{\circ}\text{C}$  were used. The thermistor array was connected to a signal conditioner/amplification unit with a gain of 500. The data from the amplifier unit was then fed to a 16 channel analog to digital (A to D) data acquisition card in the same computer as was used to control the profiler mechanism. Two of the remaining three channels on the A to D card were used for the thermocouples that monitored the tank and jet temperature and the last channel monitored the reference cold junction on the amplification unit to compensate for changes in ambient air temperature or humidity, that would otherwise cause the thermistor calibration to drift. The array was mounted in, and was positioned by, the same profiling mechanism as was used to position the ADV probe. Temperature data from the array was collected at an approximate frequency of 10 Hz.

The thermistor array was calibrated frequently using water baths at two temperatures, hot and cold. Initially calibration values were set to the standard published values for the equipment. Voltages were back calibrated from these values and the temperature data sets collected from each of the water baths. These voltages were then used in conjunction with the known temperatures of the water baths, measured with a mercury thermometer with precision of  $0.1^{\circ}\text{C}$ , to obtain the new calibration values. The calibration formula for the thermistors was assumed to be linear, these calibrations were incorporated into the data collection program that operated the thermistor array.

In spite of the reference cold junction incorporated in the signal conditioning/amplifying unit it was found that the calibration of the thermistor array would change significantly when there was a change in the weather, e.g. hot and dry to cool and wet. Hence, the array was recalibrated whenever such a change occurred in the weather, or at a minimum when every two or three experiments were completed.

The error in calibration of each thermistor is estimated to be approximately  $0.2^{\circ}\text{C}$ . When combined with the resolution error of the thermistors the error in any given temperature measurement with a thermistor could be as high as  $0.3^{\circ}\text{C}$ . In the case of experiments employing relatively small temperature differences between the jet and ambient this could introduce significant errors into the calculations of temperature flux and dilutions based on temperature measurement. These factors will be discussed more fully in section 4.4.4.

In addition to the thermistor array used for profiling in the tank, two thermocouples were used to measure the temperatures of both the replenishment flow and the jet temperature in the nozzle prior to entering the tank. Both these thermocouples had an accuracy of  $0.1^{\circ}\text{C}$  and were not subject to the calibration drift problem experienced with the thermistor array.

### **4.3 Experiments**

The details of the seven experiments carried out in this study are provided in table 4.1. In series B there were 3 experiments performed, in series A & C, 2 experiments each. Each of these experiments had three replicates or trials to investigate repeatability and to allow estimation of the variability between individual trials. Details of these experiments are provided in Table 4.1. Figure 4.3 provides a comparison of the jet Froude number and depth to diameter ratio for each of the experiments carried out in the present study, with those of Lee & Jirka (1981) and Wright et al. (1991). Experiments C1 and C2 ( $H/D = 15$ ) of the present study are approximately in the middle of the range of  $H/D$  and  $F$  investigated by Lee & Jirka, and fall just below the range investigated by Wright et al. (1991). The other experiments occupy the lower range investigated by Lee & Jirka (1981). In figure 4.4 the experiments of these studies are replotted by densimetric Froude number and depth to diameter ratio. As for figure 4.3 the experiments of the present study

are approximately in the middle of the range of these parameters as investigated by Lee & Jirka (1981) and fall below the range investigated by Wright et al (1991).

The two A series experiments had a jet nozzle diameter of 6 cm ( $H/D = 5$ ) and both had regular jet Froude numbers of 0.9, with two different densimetric Froude numbers. The three B series experiments used a jet nozzle diameter of 4 cm ( $H/D = 7.5$ ) with two of the experiments having jet Froude numbers of 0.9 and one of 1.5, each had a different densimetric Froude number. The C series was composed of two experiments with the 2 cm diameter port giving a depth to diameter ratio of 15, the jet Froude numbers were 2 and 4 and again the densimetric Froude numbers were different between experiments.

Additional details of the experiments conducted are also contained in table 4.1, including the initial momentum and buoyancy fluxes, and jet ( $l_Q$ ) and momentum ( $l_M$ ) length scales. In addition the replenishment flows and their estimated momentum/energy fluxes are provided for comparison to these quantities for the jets.

It was originally intended that certain experiments have duplicate densimetric Froude numbers while other parameters were varied, it proved difficult to accomplish this in practice. For example, experiments C1 & C2, while meant to have different jet Froude numbers were designed to have identical densimetric Froude numbers. Due to the vagaries of the hot water supply, where the temperature available varied depending on flow rates, it was not possible to reliably control the mixed temperature of the jet and achieve exactly the desired densimetric Froude number. As a result experiment C1 has a densimetric Froude number of 46.3 while experiment C2 is 58.9, a difference of almost 30%. Similarly experiments B3 & B4 were originally intended to share the same densimetric Froude number.

The range of flow conditions investigated for all experiments in this study are such that buoyancy is not of importance in the vertical jet region. The momentum length scale  $l_m$  varied from 74 cm to 218 cm for the experiments of the present study and all

were much greater than the depth (30cm). However, this does not preclude buoyancy being an important factor in the radially spreading regions in some of the experiments, where buoyancy would be acting against entrainment and upper layer growth. Also, the vertical jets of all experiments were fully turbulent at the exit from the nozzle.

#### **4.3.1 Experimental Procedure**

Prior to commencing each experiment the tank was filled with cold water and the temperature was measured, the temperature of the hot water supply was also measured. A spreadsheet, with a look up table, then converted the desired density difference (relative to the cold, ambient water) of the desired densimetric Froude number to the required temperature for the jet. Then by knowing the total flow required for the regular Froude number of that experiment, and the proportions of hot and cold water to use in the jet to achieve the desired temperature, the appropriate hot and cold water flow rates were calculated. These were the flow rates employed in the experiment.

However, because the final steady state temperature of the jet could not be predicted with complete accuracy, as the hot water supply steady state temperature varied with flow rate, temperature of the incoming water to the boiler, and other factors that are not known, the actual densimetric Froude number for the experiment could not be determined until steady state conditions had set in, approximately 20 minutes into each experiment. Since fine adjustment of the flow rates would cause a new steady state jet temperature, and would be impractical to do, the actual densimetric Froude number was usually different from that intended for the experiment. The final actual densimetric Froude number was calculated using the temperatures measured in the tank, and the same flow rates were used for each trial of an experiment to ensure that they were true replicates of their predecessors.

The replenishment flow rates were initially estimated with a preliminary model developed by G. Lawrence. These replenishment rates had been used in the flow

visualization experiments discussed in Chapter 3. Experience gained in the flow visualization study discussed in Chapter 3 (MacLatchy, 1993), had shown that the structure and behaviour of the radially spreading flow was not sensitive to the replenishment flow rate used, and hence the approximate replenishment rate to employ for each jet flow rate was known. As for the flow visualization experiments it was considered desirable to avoid over providing the replenishment flow to prevent the upper layer flow from being carried out of the tank by any circulation caused by this replenishment. Subsequently some investigations were carried out to determine what effect the replenishment flow was having on measured velocities in the tank, this is discussed in section 4.4. Comparison of the replenishment flow rates used for each experiment with the dilutions obtained, discussed in chapter 5, show that the replenishment rates were less than the flows being entrained by the jets.

Conducting an actual experiment was relatively straight forward. The profiler moved according to a predetermined program to place the ADV at the desired points for measurement of velocity. Data acquisition was for 60 seconds at a frequency of 25 Hz (1500 samples). Preliminary investigations had shown that this was of sufficient duration to provide stable averages when the data was processed later. Measurements started at the uppermost point in each profile, then proceeded downward. Profiles were taken sequentially starting at the one closest to the center of the tank, 2.5 D for A & B series, 4 D for C series, and then at positions moving outward from the first profile. While each experiment was underway the flow meters for both the jet and replenishment flows were checked frequently to ensure that fluctuations in flow rates had not occurred. In a few cases other water demands in the laboratory building had appreciably changed flow rates with the result that experiments had to be abandoned and recommenced at another time. In a similar manner the temperatures in both the jet and ambient water (lower portion of the tank) were constantly monitored by thermocouples. This data was collected by the

computer controlling the profiler and was used to ensure that there was not excessive drift in these temperatures, and hence a change from the desired buoyancy of the experiment.

Once the velocity profiling was complete the ADV probe was removed from the profiling mechanism and the thermistor array was put in place. Temperature profiling would then proceed in a manner similar to that as for velocity measurements. Unlike the ADV where each point in the velocity profile had to be measured individually, the thermistor array was capable of measuring temperatures at thirteen points at one time. Profiling proceeded outward from the point nearest to the vertical jet. At an approximate frequency of 10 Hz data was collected for 2.5 minutes at each profile position for a set of 1500 measurements from each thermistor. Flow rates were left unchanged from those used for the ADV portion of the experiment and were monitored to make sure that no variations had arisen.

Typically each velocity profile in an experiment took 23 minutes to complete, while each temperature profile only required 6 minutes. If no difficulties were encountered during the course of an experiment, it normally took 2.5 hours for an individual A series experiment (per replicate), 3 hours for a B series and 3.5 for a C series.

#### ***4.4 Data Processing and Calculations***

##### **4.4.1 Velocity Data**

The first steps in the processing of the ADV data simply involved the conversion of the data from the file format used by the ADV to that used in the graphical and data-processing software package PV Wave to calculate the desired quantities. Without going into laborious detail the velocity data was extracted from the data file by the extraction program provided by Sontek for the ADV. Next a Visual Basic program converted the files from the constant column width format the extraction routine provides the data in, to

comma separated variable (CSV) format necessary for PV Wave. Up to this point no actual analysis of data has taken place.

Once in a format acceptable to PV Wave, actual analysis begins. Because PV Wave is intended for intense data processing, and can readily handle vectors and arrays of data with single commands, most quantities are easily calculated. The three velocity components U, V, W are the radial, tangential and vertical components respectively. The following quantities are calculated from the 3 dimensional velocity data provided by the ADV:

Average of each velocity component at each depth  $d$ :  $\bar{U}_d, \bar{V}_d, \bar{W}_d$

Average of the square of each component, including turbulent fluctuations:

$$\overline{(U_d)^2} = \overline{(\bar{U}_d + u'_d)^2}, \quad \overline{(V_d)^2} = \overline{(\bar{V}_d + v'_d)^2}, \quad \overline{(W_d)^2} = \overline{(\bar{W}_d + w'_d)^2}$$

$$m_d = \overline{(U_d)^2} \quad (4.1)$$

The quantity  $m_d$  is the contribution to the total average kinetic energy made at depth  $d$ . The above quantities were used in calculating the total momentum flux of the upper layer flow. Figure 4.5 provides a schematic of many of the quantities measured and/or calculated to familiarize the reader with their orientation in the actual flow.

In order to properly calculate the volume and momentum fluxes the velocity at the surface must be estimated, since it was not possible to measure velocity any closer than 5 mm to the surface. The surface (maximum) velocity was estimated using the solution for velocity profiles developed by Chen (1980) and discussed in chapter 3. The parameters of the profile were adjusted until the synthesized profile achieved a good fit to the actual velocity data, the surface velocity was then estimated using the fitted profile. Because Chen's profile model was intended for an infinite depth ambient, and a return flow in the ambient was ignored, some adjustment of the model was necessary. The average lower layer velocity was added to the velocity data so that the velocity converged on zero in the lower layer:

$$\frac{U(R, z) + U_L}{U_{\max}(R) + U_L} = F(\xi) \quad (4.2)$$

Where  $U(R, z)$  is the velocity at some depth  $z$  in the profile located at  $R$ ,  $U_{\max}(R)$  is the maximum velocity in the profile at  $R$ , and  $U_L$  is the average lower layer velocity.  $F(\xi)$  is the numerical solution of Chen (1980) described by equation 3.14, while  $\xi = az/R$  is the dimensionless parameterization of the depth. In order to fit the theoretical profile solution to the actual data,  $U_{\max}$  and  $a$  were adjusted until a good fit to the actual data was found, as indicated by the correlation coefficient  $R^2$ , calculated between the actual data and points on the synthesized curve.

Generally the fit between the synthesized curve and actual velocity data was best for velocities measured above the interface (positive) and close to the surface. At larger radii the fit between the theoretical curve and actual data became increasingly worse for the points in the vicinity of the interface. This is demonstrated by Figure 4.6 which plots the actual data and fitted theoretical profiles for  $R/D = 2.5$  and  $15$  from experiment B4. In cases where a good fit to the majority of the velocity data was not possible the theoretical profile was fit to the top 4 or 5 points (nearest to the surface) to provide the best estimate of the surface velocity. The maximum velocities synthesized from Chen's theoretical profile are plotted for all experiments in Figure 4.7.

A three point moving average was used to smooth the velocity profile. This was used to overcome some variability that appeared to occur in ADV measurements near to the surface, discussed in section 4.4.4.2. The velocity was averaged from the initial value at that location and the velocities immediately above and below it. The moving average was calculated as:

$$(U_d)_A = (U_{d-1} + U_d + U_{d+1})/3 \quad (4.3)$$

Profile smoothing started with the second measured point in the profile, at a depth of 1cm. The first measured point was not “smoothed”, nor was the estimated point at the surface.

#### 4.4.2 Temperature Data

The temperature data from the thermistor array and the thermocouples monitoring the tank and jet temperatures were converted to a CSV format for use in PV Wave in a similar manner as for the velocity data. In fact, the same visual basic program was utilized with only a minor change to account for the 15 columns of data from the thermocouple array as compared to the 4 columns from the ADV data extraction routine. Actual processing of the temperature data occurred within PV Wave routines.

Surface (maximum) temperatures for each profile were estimated using the same theoretical curve fitting technique described above for the velocity profiles except that the temperature data was fit to:

$$\frac{T(z,R) - T_A}{T_S(R) - T_A} = F(\xi) \quad (4.4)$$

The maximum or surface temperature in the profile located at radius  $R$  is  $T_S(R)$ ,  $T_A$  is the ambient temperature, and  $T(z,R)$  is the temperature at some depth  $z$  in the profile at  $R$ . The surface temperatures synthesized from the fitted theoretical profile are plotted in Figure 4.8.

As had been done for the velocity profiles, the temperature profiles were smoothed by a three point moving average identical to equation 4.3, this removed the small irregularities arising from inaccuracies in thermistor calibration.

#### 4.4.3 Calculated Quantities

From the raw temperature data, the time averaged temperature is calculated at each depth. The minimum time averaged dilution is taken from the thermocouple closest to the surface. The formula for calculating this dilution is:

$$S_{\min} = (T_J - T_A) / (T_s - T_A) \quad (4.5)$$

Where:  $S_{\min}$  = minimum time averaged dilution (at surface).

$T_J$  = Temperature of jet discharge.

$T_A$  = Temperature of ambient (tank).

$T_s$  = Temperature at water surface (top of radially spreading layer).

The total momentum flux occurring at each profiling position (profile  $i$ ) was calculated by summing the individual contributions at each depth  $d$  from the surface to the depth at which the radial velocity becomes negative ( $d_n$ ).

Recall that the first measurement point closest to the surface is at a depth of 0.5 cm ( $\Delta z_o = 0.5$  cm) and measurements occur at intervals of 0.5 cm ( $\Delta z = 0.5$  cm) thereafter. The total momentum flux ( $m_i$ ) for the radially spreading upper layer measured in the profile at radius  $r_i$  is the sum of the momentum (per unit width) at the individual depths ( $m_d$ ) multiplied by the depth increment and total width ( $2\pi R_i$ ), the momentum flux contribution (per unit width) from the estimated surface velocity is  $m_s = U_s^2$ :

$$m_i = 2\pi r_i \left( (0.5\text{cm}) \sum_{0.5\text{cm}}^{d_n} m_d + (0.25\text{cm}) m_s \right) \quad (4.6)$$

The depth increment of 0.25cm is used for  $m_s$  to reflect that this value occurs at the surface and the depth over which it acts in the summation is half (0.25cm) that of the successive measurements, which are spaced at intervals of 0.5cm each. The remainder of the  $m$  values are summed from the 0.5 cm depth to the depth at which the velocity changes sign  $d_n$ . This formulation also applies in equations 4.7 and 4.8.

The average dilution of the whole radially spreading upper layer is calculated based on the temperature flux of the upper layer. The volume flux could also be used to determine the bulk dilutions but is more prone to error, the temperature flux is likely to have less overall error, this will be more completely discussed in section 4.4.4. The

average radial velocities are summed from the surface to the depth ( $d_n$ ) at which the average radial velocity changes sign, from an outward to an inward flow. The total volume flux of the upper layer measured in the profile at radius  $r_i$  is:

$$\mu_i = 2\pi r_i \left( (0.5\text{cm}) \sum_{0.5\text{cm}}^{d_n} U_d + (0.25\text{cm}) U_s \right) \quad (4.7)$$

The temperature flux is similarly calculated:

$$Tf = 2\pi r_i \left( (0.5\text{cm}) \sum_{0.5\text{cm}}^{d_n} (T_d - T_A) U_d + (0.25\text{cm}) (T_s - T_A) U_s \right) \quad (4.8)$$

The subscripts  $d$  and  $s$  denote the values of temperature ( $T$ ) and velocity ( $U$ ) at a depth  $d$  and at the surface respectively. The bulk dilution can be calculated by two different means, from the volume flux or by calculating the average temperature of the upper layer from the temperature flux. By volume flux the bulk dilution is:

$$S = \mu / Q_o \quad (4.9)$$

The average temperature is the temperature flux (equation 4.8) divided by the volume flux (equation 4.7):

$$T_{AVG} = \frac{2\pi r_i \left( (0.5) \sum_{0.5}^{d_n} (T_d - T_A) U_d + (0.25)(T_s - T_A) U_s \right)}{2\pi r_i \left( (0.5) \sum_{0.5}^{d_n} U_d + (0.25) U_s \right)} \quad (4.10)$$

The bulk dilution calculated from the average temperature is then:

$$S = (T_j - T_A) / (T_{AVG} - T_A) \quad (4.11)$$

The bulk dilutions as calculated from the volume flux are plotted against the bulk dilutions calculated from the temperature flux for comparative purposes in Figure 4.9. For the most part the dilutions calculated by these two methods are similar, with the

exception of those for experiments A1 and A2, where the volume flux based dilutions are less than those calculated from the temperature flux. For reasons discussed in section 4.4.4, the bulk dilution calculated from equation 4.9, involving both the temperature flux and volume flux, is considered more reliable.

The minimum and average dilutions, and the momentum flux are the primary quantities calculated from the density and velocity profiles obtained from the experiments. There are two further quantities useful in describing or determining conditions in the radially spreading upper layer. These are the composite Froude Number and the bulk Richardson Number.

The composite Froude number ( $G^2$ ) is calculated using the depth averaged velocities in the upper ( $U_u$ ) and lower layer ( $U_l$ ), the depth of each layer and the average reduced gravitational constant. The bulk dilution obtained from the temperature flux was employed to predict the upper and lower layer flows rather than directly employing the velocity data, as a means of circumventing the errors that appeared to be present in the velocity data, this is discussed more fully in section 4.4.4. The composite Froude number at each radius  $R$  is then calculated as follows, recall that  $H$  is the total depth of water and we will define the interface depth ( $h$ ) as the depth where the radial velocity changes direction ( $d_n$ ):

$$U_U = SQ_o/h \quad (4.12)$$

$$U_L = \frac{(S-1)Q_o}{H-h} \quad (4.13)$$

$$g' = g'_o/S \quad (4.14)$$

$$G^2 = \frac{U_U^2}{g'h} + \frac{U_L^2}{g'(H-h)} \quad (2.29)$$

The average velocity and depth of the upper layer and  $g'$  are used in calculating the bulk Richardson number:

$$R_i = \frac{g'h}{(U_U - U_L)^2} \quad (4.15)$$

These quantities are the ones of most importance in describing the conditions in the radially spreading flow. In addition the initial momentum flux and temperature flux were calculated as (respectively):

$$M = U_o^2 A_o = U_o Q_o \quad (4.16)$$

$$Tf_o = (T_J - T_A)U_o A_o = \Delta T_o Q_o \quad (4.17)$$

#### 4.4.4 Errors and Discrepancies

In this section the errors associated with the experimental measurements and calculations are discussed. Firstly, the apparent discrepancy between the momentum measured in the radially spreading flow and the initial momentum flux of the vertical jet is discussed, along with its implications in the following sub-section (4.4.4.1). Similarly the discrepancy between the measured and initial temperature fluxes is discussed and it is shown, by comparison to the discrepancy in the momentum flux, that most of this error arises in the velocity measurements (also in 4.4.4.1). Thus the quantities calculated from the temperature flux appear to be subject to less error than if calculated directly from the velocity profiles. Later in this section, the sources of error in the velocity measurements with the ADV and in the temperature measurements are discussed, in sub-sections 4.4.4.2 and 4.4.4.3 respectively, and the magnitudes of these errors are estimated. The overall errors on results from the present study are discussed in section 4.4.4.4.

#### 4.4.4.1 Momentum and Temperature Fluxes

The variation of  $m/M$  with non-dimensionalized radius was averaged over all experiments, and is plotted in figure 4.10. In general the averaged  $m/M$  increased gradually with radius, although there was considerable scatter in the data.

The gradual increase in momentum with distance may represent a transformation of energy from potential energy, in the form of free surface elevation, to kinetic energy ( $\alpha U^3$ ) and hence to momentum ( $\alpha U^2$ ). As an estimate of the magnitude of this effect the following sample calculation was made, if the radial flow has a mean velocity of 10 cm/s and the free surface decreases in elevation by only 0.05 cm, conversion of this potential energy to momentum is sufficient to accelerate the flow to 14 cm/s, neglecting radial spreading and entrainment. The momentum is effectively doubled by this small conversion of potential energy. Such a free surface change would not be visually detectable. Hydrostatic pressures or water depths were not measured as part of the present study.

The error in velocity measurements can at least be estimated from the discrepancy between the calculated momentum flux in the radial flow and the initial momentum flux ( $D_k$ ). This neglects the legitimate energy losses that should be present due to viscous dissipation of momentum, but would still provide a reasonable means of estimating the errors in the velocity measurements. Since the momentum is proportional to the velocity components squared, it was assumed that the discrepancy in the radial velocity profile measurements would be proportional to the square root of the discrepancy in the overall momentum flux. Thus, the ratio of the measured velocity to the actual velocity was assumed to be proportional to the square root of the ratio of the measured momentum to the initial momentum.

$$D_U = \frac{U_m}{U_A} \propto \sqrt{\frac{m}{M}} \propto \sqrt{D_k} \quad (4.18)$$

By extension the discrepancy between the measured volume flux and what the actual volume flux should be can be estimated as:

$$D_Q = \frac{Q_m}{Q_a} \propto \sqrt{D_k} \quad (4.19)$$

In a similar manner as for the momentum flux, the discrepancy in the measured temperature flux can be estimated as:

$$D_T = \frac{Tf}{Tf_o} \quad (4.20)$$

The ratio of the measured temperature flux to the initial temperature flux ( $Tf/Tf_o$ ) was averaged over all experiments and is also plotted as a function of radius in figure 4.10, for comparison to the momentum flux discrepancy ( $m/M$ ). As for the momentum flux discrepancy the ratio of measured to initial temperature flux increased gradually with radius. The patterns of the two quantities appear nearly identical. Unlike the momentum flux however, it is expected that the temperature flux in the upper layer should be conserved.

By comparing the discrepancies between the momentum flux and its initial value and the equivalent quantity for the temperature flux it is possible to make some statements about the errors in the temperature flux and the sources of those errors and their effects on such quantities as the bulk dilution. In figure 4.11 the individual temperature flux discrepancies are plotted as function of the corresponding square root of the individual momentum flux discrepancies. As can be seen from this figure the two quantities are very closely correlated, indicating that the majority of the error in the temperature flux probably arises from error in the velocity measurements. The correlation coefficient for the temperature flux discrepancy to the square root of the momentum flux discrepancy was 78%. Thus, errors in the temperature measurements appear to be only a small proportion of the error in the temperature flux.

If it is assumed that the error in velocity measurements is proportionally constant with depth within a profile, then the errors (or corrections) in the volume flux and temperature flux arising from the velocity measurements can be expected to largely cancel out. This is the case as the volume flux is the integral of the radial velocity over the depth of the upper layer while the temperature flux is the integral of the product of velocity and temperature over the depth of the upper layer. Recalling equation 4.10 where the flux averaged temperature is:

$$T_{AVG} = \frac{2\pi r_i \left( (0.5) \sum_{0.5}^{d_u} (T_d - T_A) U_d + (0.25)(T_S - T_A) U_S \right)}{2\pi r_i \left( (0.5) \sum_{0.5}^{d_u} U_d + (0.25) U_S \right)} \quad (4.10)$$

Thus if the error in velocity measurements is proportional constant over the depth of the profile the error should cancel out in the calculation of average temperature. The remaining source of error in calculating the temperature flux will then be in the temperature measurements themselves. As has already been discussed in this section the discrepancy in calculated temperature flux is well correlated to the square root of the discrepancy of the momentum, which is assumed to be indicative of the discrepancy in velocity measurements. Therefore it is reasonable to expect that the calculation of the average temperature of the upper layer is relatively unaffected by errors in the velocity profile and provides the best means to calculate bulk dilution.

#### 4.4.4.2 Error in Velocity Measurements

In the previous section it was argued that most of the error in the measured temperature flux arose from the velocity measurements, acquired with the ADV. One source of error in these velocity measurements was a combination of how the ADV was employed, and how the ADV functions. The instrument when initially activated measures the distance to any boundary directly in the “view” of the ADV head, in this case the

water surface. This measured boundary distance is used by the ADV to correct for sound waves reflected by this boundary, that might otherwise be interpreted as part of the velocity signal. Of necessity, this initialization took place when the tank was full but before the jet had been turned on, as the surface disturbances (ripples) from the jet would have prevented the ADV from "finding" the surface. This created a problem when the ADV was moved from the initialization point to other points in the profile as part of the process of measuring velocities in the upper layer. The instrument was not "aware" of this movement away from its original position and the change in the boundary distance, signal correction continued to use the initial boundary distance. It was impractical to reinitialize the instrument for every point in the profile as the experiment would have to have been suspended to do so. This was one probable source of error, the instrument continued to process the signal using a boundary distance that was not correct.

In addition to the boundary measurement problem another source of error with the ADV was that there were surface disturbances created when the vertical jet was in operation. Movement of the surface could have created additional distortion of the reflected sound signal and "confused" the instrument. It was noted that during the course of velocity measurements in the upper layer, while still relatively close to the surface, that the velocity signal fluctuated at a very high frequency and low correlation coefficients were noted during data acquisition. Different experiments experienced these problems to varying degrees. This was particularly been the case for the A series experiments where the jet is relatively large in relation to the depth, large surface waves were noted and there appears to be a fairly large error in the energy flux at small radii for these two experiments.

Qualitative evidence that the above discussion is a valid explanation is provided by the correlation coefficients calculated by the ADV itself. Within 3 to 4 cm of the surface the correlation coefficients were often less than the recommended 70%. As the probe was moved away from the surface, or to larger radii, the correlation coefficients

would improve. Unfortunately there was no way to operate the instrument in proximity to the surface without this problem occurring. However, the velocity averages produced by the ADV contained no obvious anomalies and were stable with time, this problem appears to have been a systematic one.

Despite the difficulties with velocity measurement, the ADV remained the best instrument for measuring velocities in the radially spreading flow, due to its small size and sampling volume, and its increased accuracy over a propeller meter or equivalent. Laser Doppler Anemometers were not a practical option due to the optical problems that would be encountered with the circular tank wall and alignment with the desired points in the profiles. Also the velocity measurements had to be made quickly due to the large number of measurements required and the limited duration of experiments, this also ruled out the use of a Laser Doppler Anemometer.

Upper layer depths were determined from the zero crossing point where the radial velocity changed direction in the velocity profile. In most cases the velocity profiles cross from positive to negative radial velocities at a relatively shallow angle. Under these conditions a relatively small error in the magnitude of the measured velocities could shift the zero crossing, and change the upper layer depth, by a significant amount, possibly as much as 5 mm. This error will tend to be larger at larger radii, since at small radii the velocity profiles tend to be steeper in the vicinity of the interface.

#### **4.4.4.3 Error in Temperature Measurements**

The thermistors used in the profiling array were capable of a precision of  $0.1^{\circ}\text{C}$ . As previously mentioned the calibration error was approximately  $0.2^{\circ}\text{C}$  for a combined error of up to  $0.3^{\circ}\text{C}$ . This is the potential error of an individual thermistor. In calculating the error of the average temperature, calculated from the temperature flux, it must be considered that that portion of the array of thermistors within the upper layer is contributing to the resulting average temperature. To some degree it can be expected that some of the error from individual thermistors will be averaged out, some will read high,

some low, but when the total input from the array is averaged some of this error will be eliminated. The temperature measurements are flow weighted so that there is not equal weighting for each thermistor. Individual thermistor error will still have some influence, but the highest temperatures, which are the least subject to error, coincided with the highest velocities, and would be weighted the most heavily. It appears likely then that the error of the average temperature is smaller, perhaps of the order of  $0.1^{\circ}\text{C}$ .

The smallest average temperature recorded in these experiments was in the A series (A2) where at the outermost profile the average (excess above ambient) temperature was approximately  $0.6^{\circ}\text{C}$ . With an estimated error of  $0.1^{\circ}\text{C}$  in the average temperature, this suggests a maximum error of slightly less than 20% in the bulk dilution calculated from temperature in this profile. Average temperatures are much higher for all other experiments, generally all above  $1^{\circ}\text{C}$ , but the estimate of 20% error is probably still valid when other contributing factors are considered, such as whether or not the error in velocity measurements, which weight the temperatures in temperature flux calculation, is truly proportional throughout the profile.

The surface temperature, used to calculate the minimum or surface dilution, is subject to a larger error since it depends entirely on one temperature measurement and is not averaged over a group of thermistors. This measurement likely has a larger error, perhaps approaching the  $0.3^{\circ}\text{C}$  value identified as the potential error for an individual thermistor. However, the surface temperatures are also higher than the average temperature of the upper layer flow so the degree of error is approximately 30% for minimum (surface) dilutions.

#### **4.4.4.4. Overall Error and Repeatability**

The standard deviations of the results (dilutions, composite Froude numbers and bulk Richardson number) of each replicate for each experiment was between 10% and 20%. This variability was greater for the A series experiments than for B series, and for the B series compared to the C series. Thus the variability in results between experiments

decreased with increasing  $H/D$  ratio. The larger flows involved in the experiments with larger port diameters may have been harder to reproduce accurately from one replicate to another and also produced more surface waves and activity, likely increasing the error in velocity measurements made by the ADV. One profile (at  $R/D = 10$ ) had to be eliminated from one of the replicates of experiment B2 due to an apparent problem, discovered after the fact, where jet flow rates dropped for a period of approximately two minutes. This may have been due to other water uses in the laboratory building. In general the replicates of each experiment produced similar results.

The flow meter used to measure and control the jet discharge was found to have a calibration error whereby it overestimated flows by approximately 10%. This error was compensated for when setting the flows for each experiment. However, the flow rates could fluctuate during the course of experiments, and there was still some degree of error in replicating the flow rates from one trial to another. These effects combined could produce an error estimated at up to 5%.

Based on the preceding factors the following estimates of errors in the results were made. As its error depends primarily on errors in temperature measurement the temperature flux based bulk dilution has an estimated error of up to 20%. The time averaged minimum or surface dilution is attributed an error of up to 30%. Composite Froude numbers and bulk Richardson numbers, which rely on a combination of velocity data and dilution estimates in their calculation, and which are functions of velocity squared, were estimated to have errors of up to 50%. Upper layer depths (or interface depths) that are taken from the velocity profiles are assumed to have an error of less than 2 mm, the percentage error declines as the upper layer grows in thickness with radial distance.

Momentum imparted to the tank by the replenishment injection and its effect on the velocity profile is not considered, though generally the energy of the artificial replenishment is much smaller than the energy of the jet, less than 6%. The energy

imparted to the experimental tank by the replenishment flow and its effect on the velocity profiles are discussed in the following section.

#### ***4.5 Investigation of Replenishment Flows***

The validity of this experimental study depends on the replenishment flows not creating a situation that alters the radially spreading flow from that which occurs in an infinite ambient environment. One major concern is that the replenishment flow should not have been larger than the flow required for entrainment into the radially spreading jet. This could have the effect of lifting the upper layer and carrying it out of the tank, changing the velocity profile and affecting dilution calculations. Equally as important is that the replenishment flow should not introduce enough energy into the tank that it sets up a circulation or promotes mixing, this requires that the flow be sufficiently baffled that velocities are kept low and do not influence the jet.

To determine the possible effect of the replenishment flow the tank was operated with just the replenishment flow running. Rhodamine dye was mixed with the replenishment flow and the flow patterns and velocities observed. The replenishment flow rate for which this was done was equivalent to the largest one used in any of the experiments, that being 5.68 l/s (90 USGPM).

Observations of the flow patterns, made possible by the dye, indicated that the majority of the flow exiting the ring diffuser, with no vertical jet operating, went almost directly up the walls of the circular tank and out of the tank, i.e. the shortest path out of the tank. Only a relatively small proportion of the replenishment flow was directed inward to the center of the tank and location of the vertical jet nozzle. This flow pattern would not have a significant effect on the flow patterns induced by the vertical jet.

In addition, the rate that the dye front advanced at, in conjunction with ADV measurements in the vicinity of the ring diffuser, showed that the velocities in this area were on the order of 1 cm/s. From this the energy or momentum flux imparted to the tank

by the replenishment flow can be estimated. The momentum flux of the flow is the product of the velocity and flow rate, for this case the flow rate was  $5700 \text{ cm}^3/\text{s}$ , with a velocity of about  $1 \text{ cm/s}$ , this indicates the momentum flux of the replenishment flow is of the order of  $5700 \text{ cm}^4/\text{s}$ . This largest replenishment flow rate was used for experiment C2, experiments A1 and A2 were similar with replenishment flow rates of  $5100 \text{ cm}^3/\text{s}$ . The corresponding momentum flux for the vertical jet in experiment C2 is  $98600 \text{ cm}^4/\text{s}$ , so the momentum input to the tank from the replenishment flow is approximately 6% of that from the vertical jet itself. It seems reasonable then that the vertical jet, with its much higher momentum, should dominate the flow conditions in the experimental tank. The momentum flux of the replenishment flow for the other experiments was calculated in a similar manner.

Experiment	A1	A2	B2	B3	B4	C1	C2
Initial Flow Rate ( $Q_o$ ) ( $\text{cm}^3/\text{s}$ )	1960	1960	708	708	1180	278	557
Port Diameter (D) (cm)	6.0	6.0	4.0	4.0	4.0	2.0	2.0
Jet Froude number ( $F$ )	0.9	0.9	0.9	0.9	1.5	2.0	4.0
Initial Densimetric Froude num. ( $F_o$ )	27	39	20	26	37	46	59
Jet Reynolds number	$3.6 \times 10^4$	$3.6 \times 10^4$	$2.0 \times 10^4$	$2.0 \times 10^4$	$3.3 \times 10^4$	$1.6 \times 10^4$	$3.1 \times 10^4$
Jet Temperature ( $T_J$ ) ( $^{\circ}\text{C}$ )	21.3	17.6	22.6	17.6	20.2	20.9	31.7
Ambient Temperature ( $T_A$ ) ( $^{\circ}\text{C}$ )	15.2	14.4	9.7	8.3	8.8	6.9	9.4
Initial Reduced Gravity ( $g'_o$ ) ( $\text{cm}/\text{s}^2$ )	1.25	0.54	2.08	1.16	1.64	1.83	4.53
Jet Nozzle Area ( $A_o$ ) (cm)	28.3	28.3	12.6	12.6	12.6	3.14	3.14
Initial Jet Velocity ( $U_o$ ) (cm/s)	69	69	56	56	94	89	177
Initial Buoyancy Flux ( $B_o$ ) ( $\text{cm}^4/\text{s}^3$ )	2445	1058	1474	822	1941	510	2521
Initial Momentum Flux ( $M_o$ ) ( $\text{cm}^4/\text{s}$ )	$1.4 \times 10^5$	$1.4 \times 10^5$	$4.0 \times 10^4$	$4.0 \times 10^4$	$1.1 \times 10^5$	$2.4 \times 10^4$	$1.0 \times 10^5$
Jet Length Scale ( $l_Q$ ) (cm)	5.32	5.32	3.54	3.54	3.54	1.77	1.77
Momentum Length Scale ( $l_M$ ) (cm)	143	218	74	99	138	87	111
Replenishment Flow ( $Q_R$ ) ( $\text{cm}^3/\text{s}$ )	5060	5060	2850	2850	4430	2850	5700
Replenishment Momentum Flux ( $M_R$ ) ( $\text{cm}^4/\text{s}$ )	4500	4500	1425	1425	3450	1425	5700

Table 4.1: Details of experiments performed in the present study.

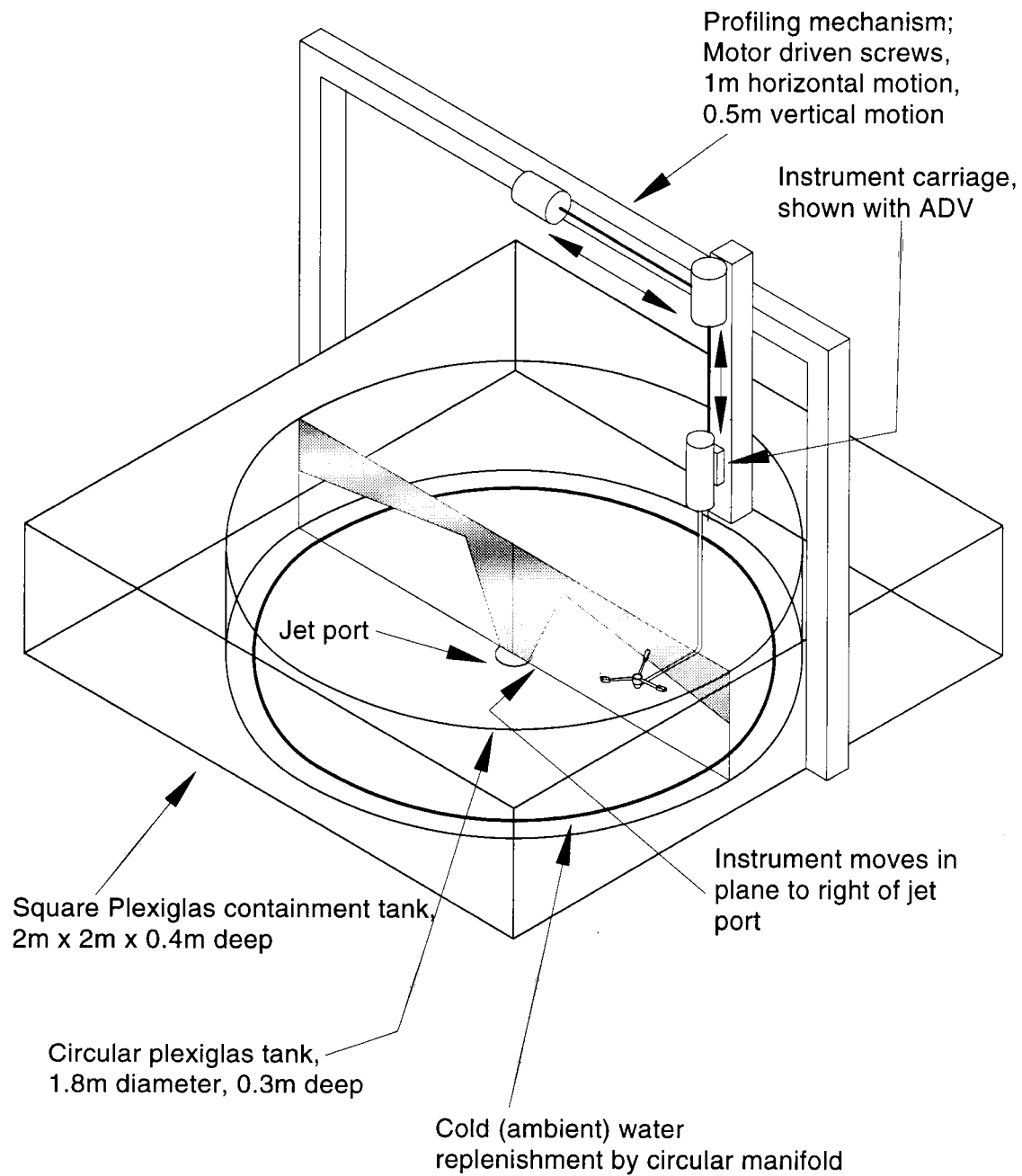


Figure 4.1: Schematic of tank and profiling mechanism

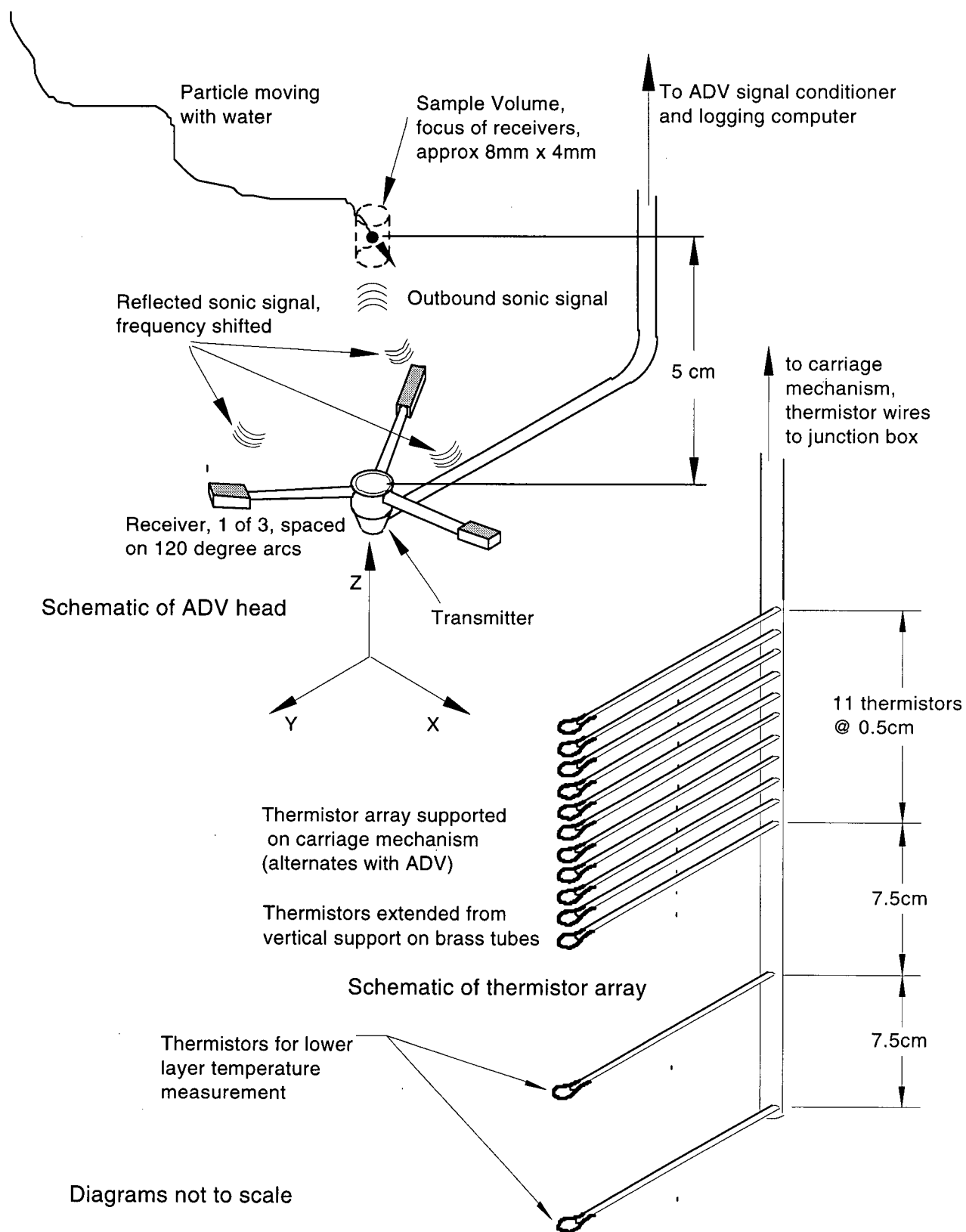


Figure 4.2: Schematic diagrams of ADV head and thermistor array.

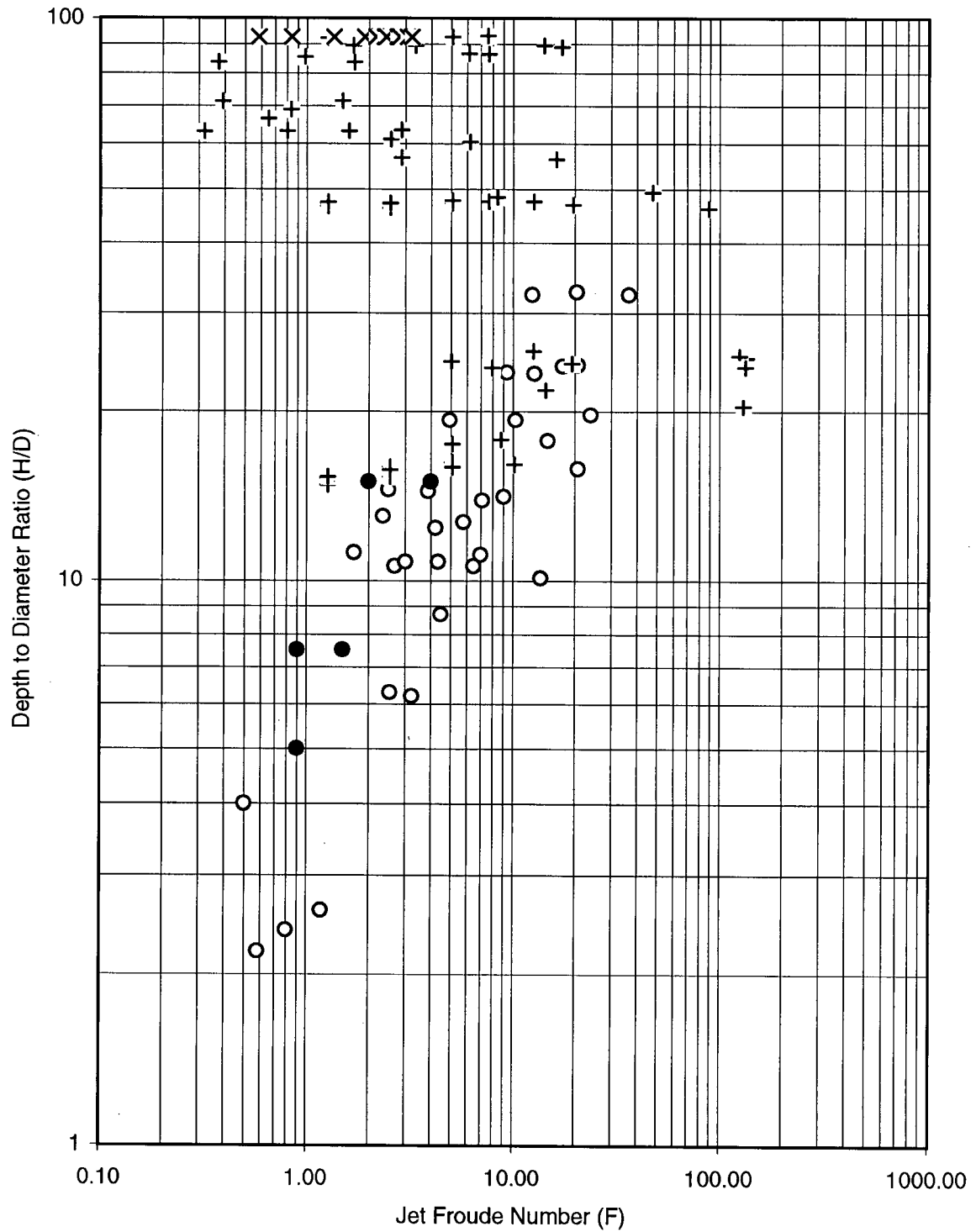


Figure 4.3: Comparison of the experiments of Lee & Jirka (1981) (o), Wright et al. (1991) (+), Fisher (1995) (x), and the present study(•), by jet Froude number ( $F$ ) and depth to diameter ratio ( $H/D$ ).

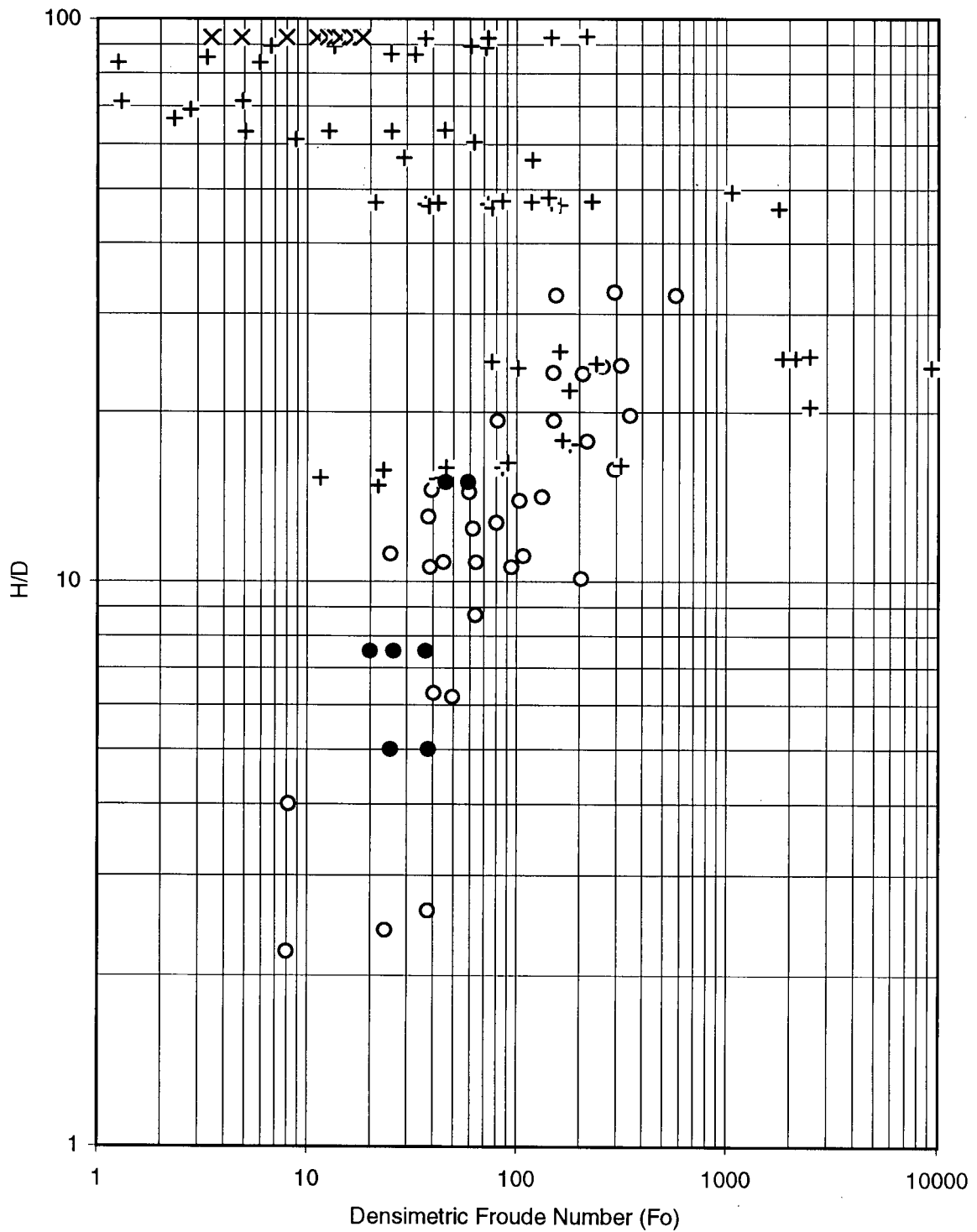


Figure 4.4: Comparison of the experiments of Lee & Jirka (1981) (o), Wright et al. (1991) (+), Fisher (1995) (x), and the present study (•), by densimetric Froude number ( $F_o$ ) and depth to diameter ratio ( $H/D$ ).

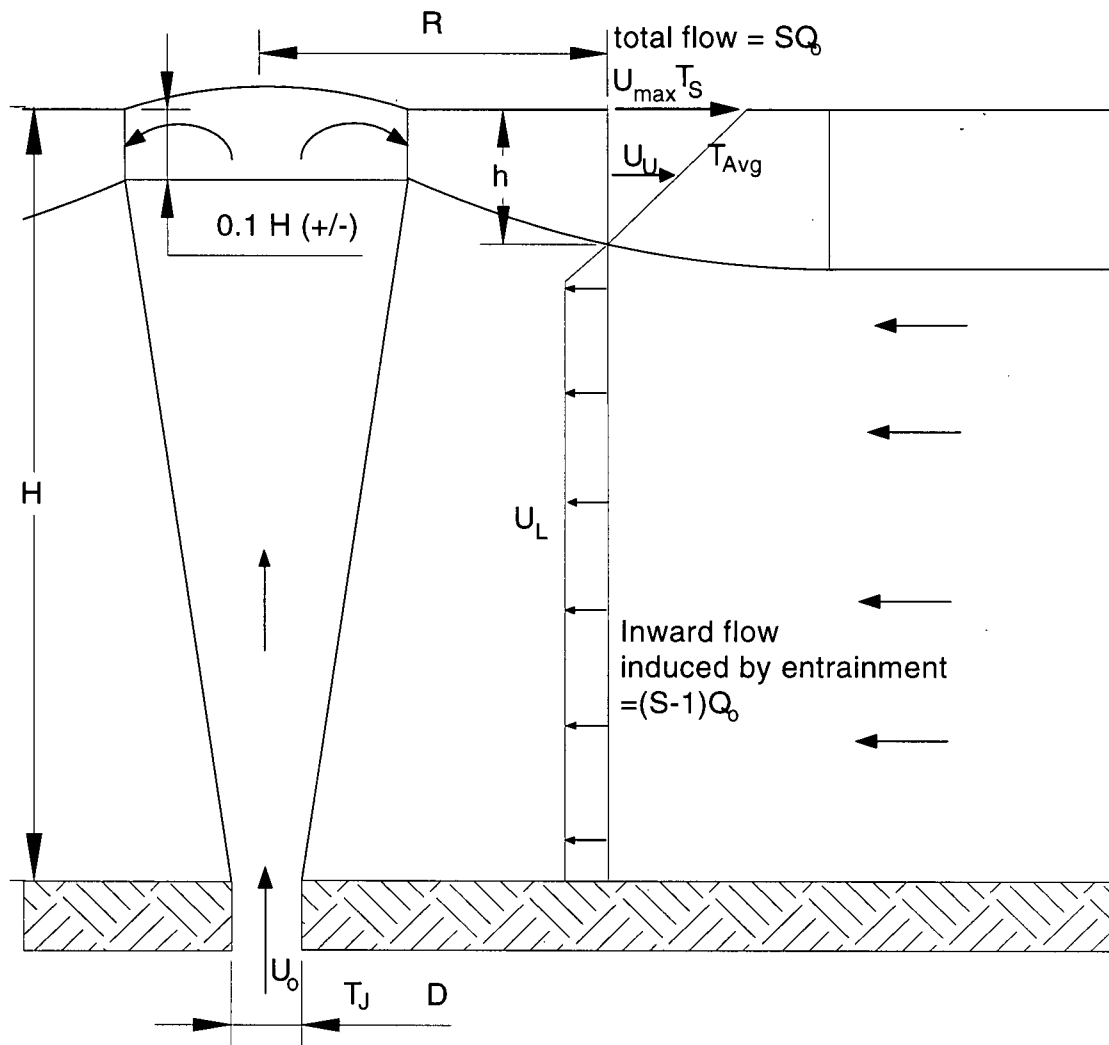


Figure 4.5: Definition sketch of quantities.

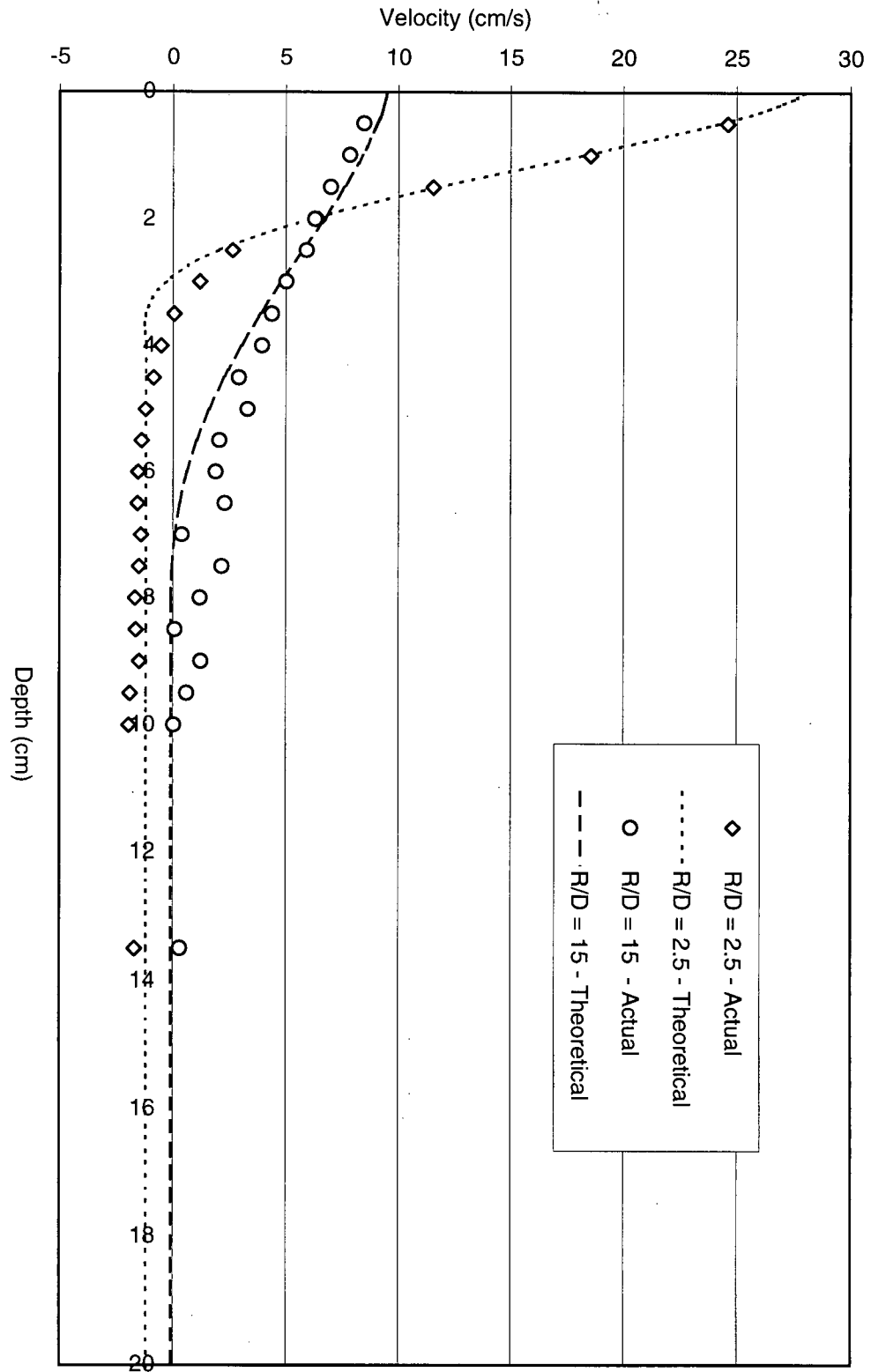


Figure 4.6: Sample plot of velocity data from experiment B4 at R/D of 2.5 and 15 superimposed with theoretical velocity profile of Chen (1980)

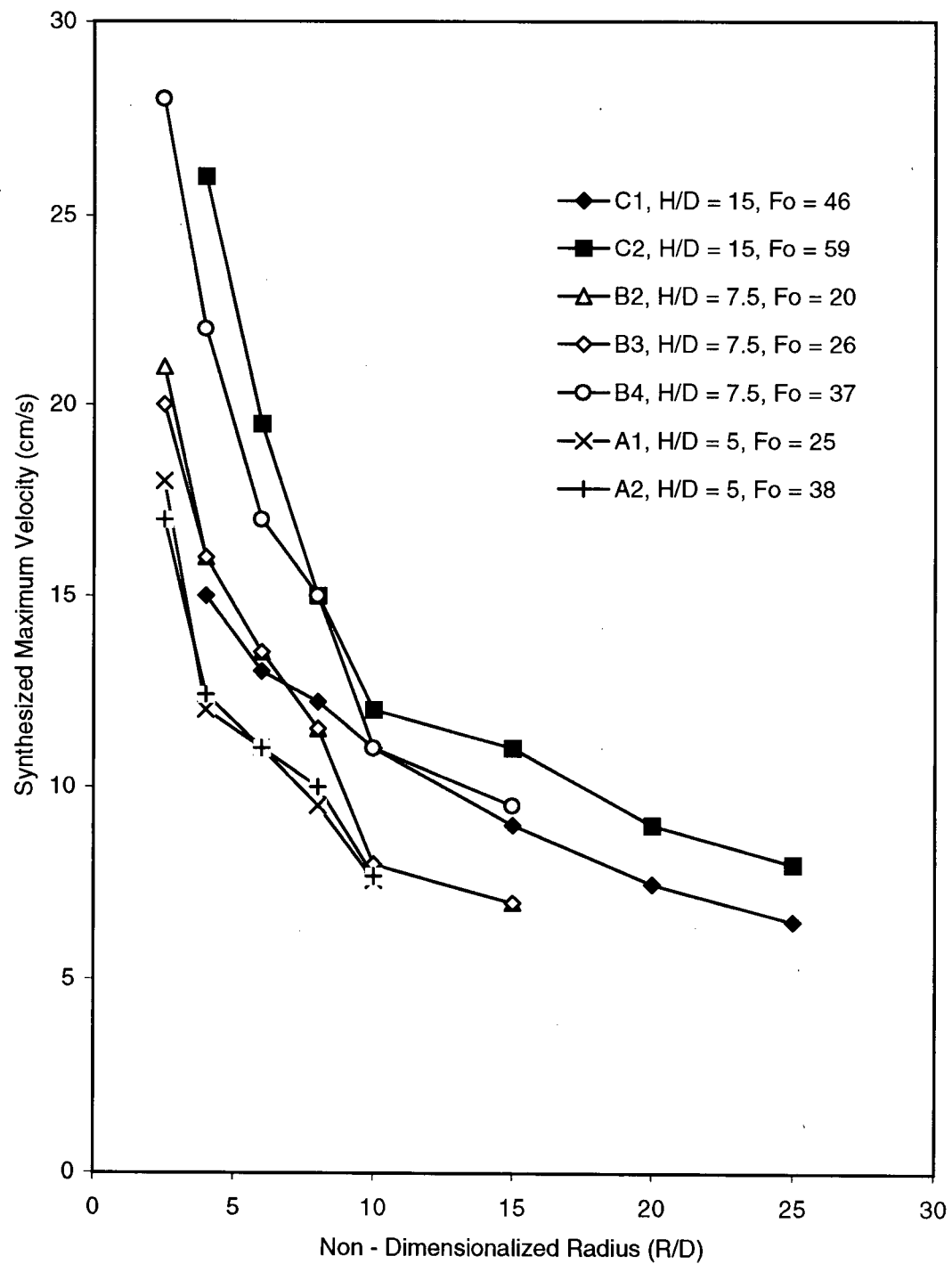


Figure 4.7: Maximum velocities calculated from fitted theoretical velocity profile of Chen (1980), for all experiments.

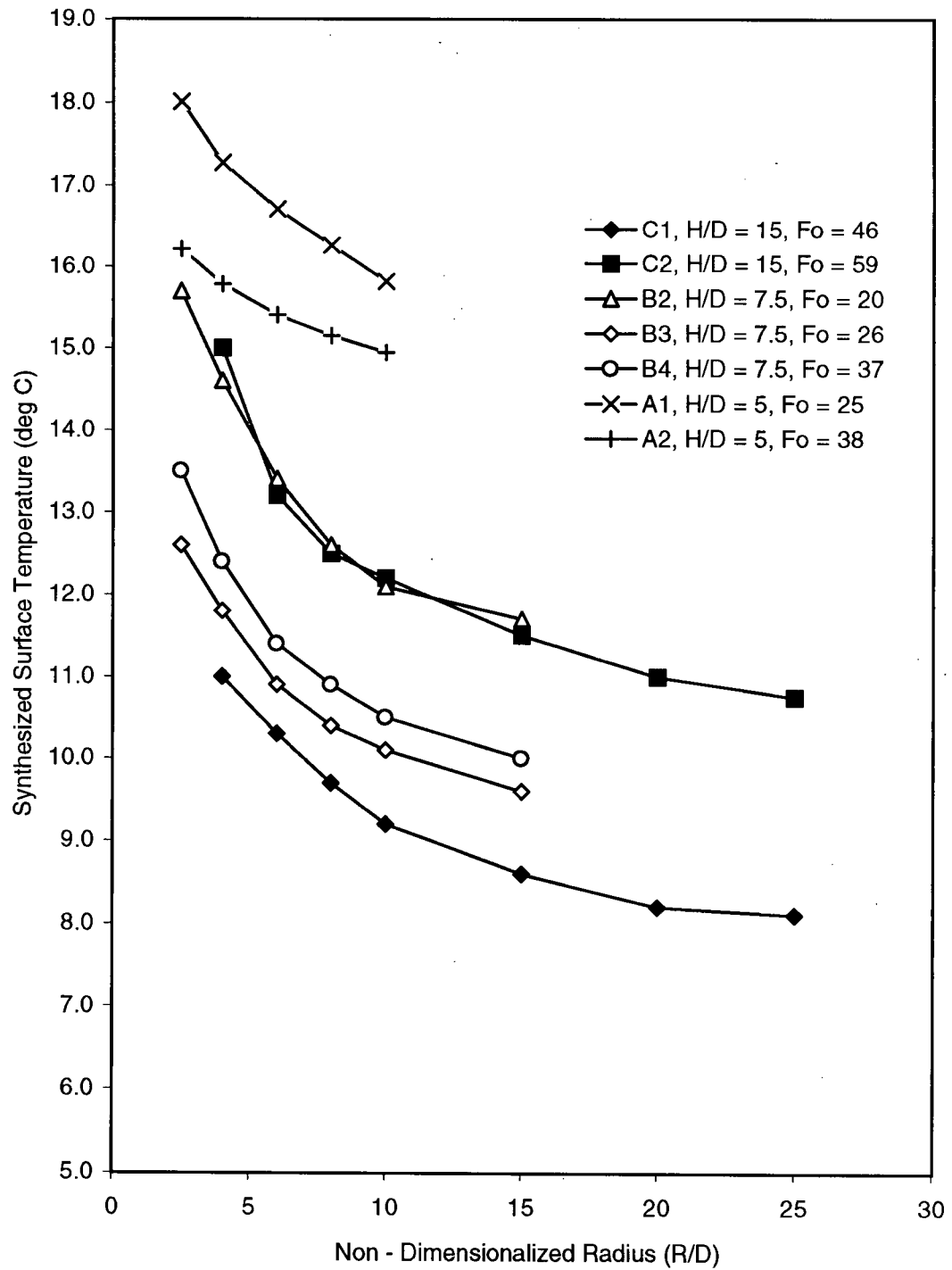


Figure 4.8: Surface (Maximum) temperatures calculated from fitted theoretical temperature profile of Chen (1980), for all experiments.

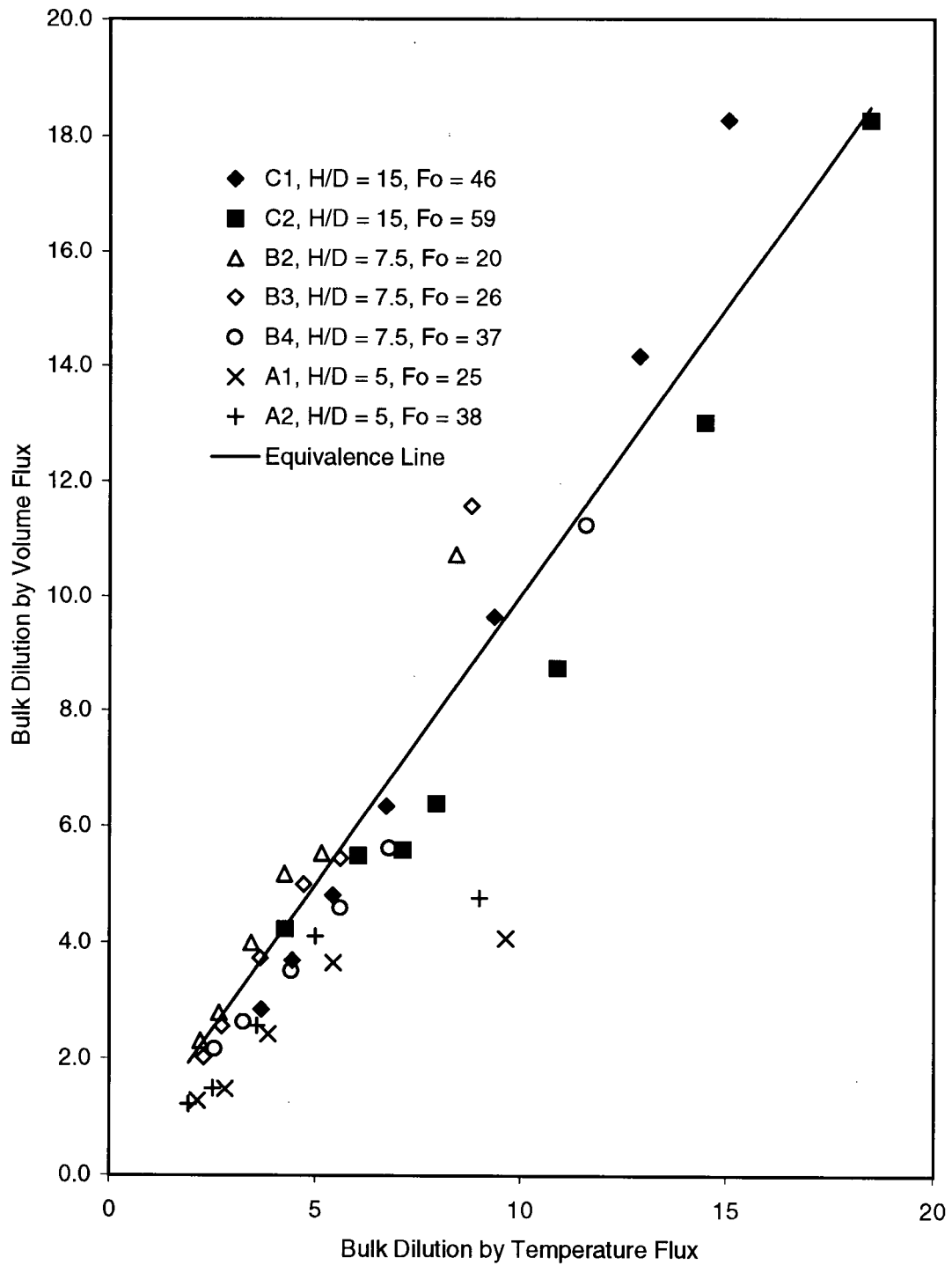


Figure 4.9: Comparison of bulk dilution calculated by volume flux with bulk dilution calculated by temperature flux.

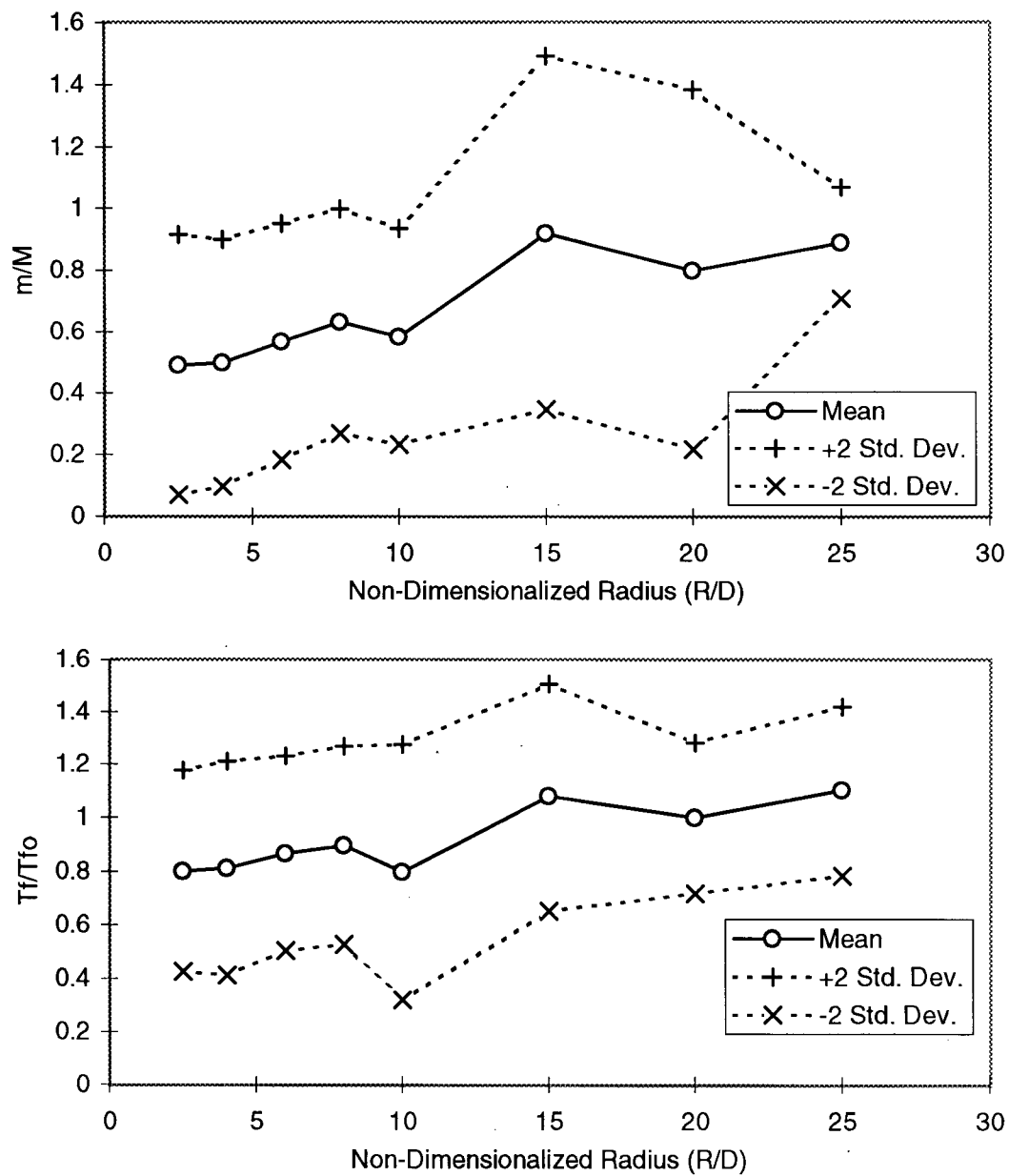


Figure 4.10: Plot of momentum flux discrepancy ( $m/M$ ) and measured temperature flux discrepancy ( $T_f/T_{f0}$ ), as function of radius, averaged over all experiments.

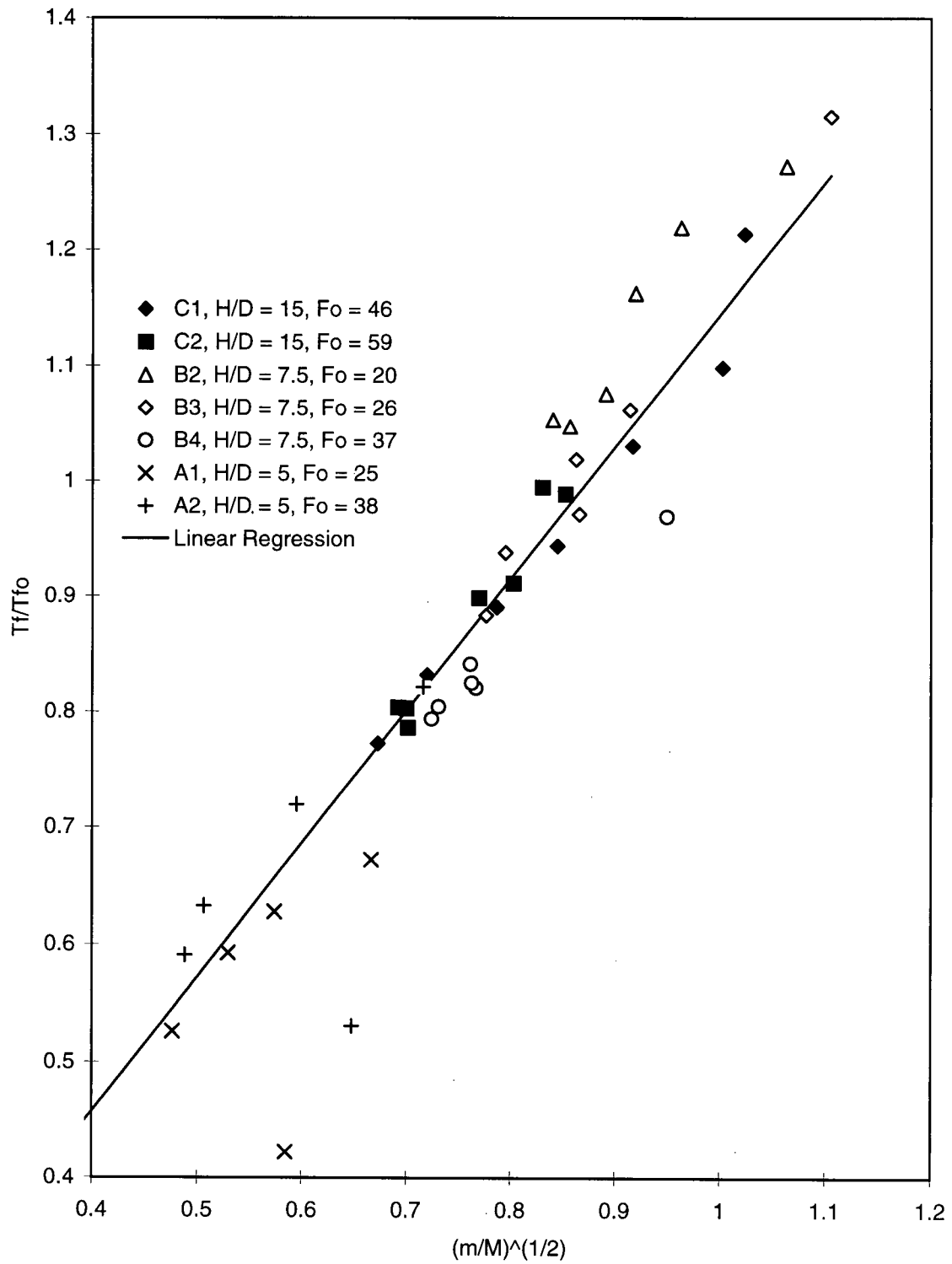


Figure 4.11: Temperature flux discrepancy as function of square root of momentum flux discrepancy.

## Chapter 5

### Results and Discussion

#### **5.1 Introduction**

In this chapter the results arising from the experiments of the present study are developed and discussed. The most important results obtained from the present study are the relationships for the variation of the mean and minimum dilution and depth of the upper layer with radial distance. From these quantities, any of the other quantities useful in describing the radially spreading flow may be obtained, for instance the stability or composite Froude numbers.

Once the dilution involving the vertical jet was removed, as discussed in the following section, the bulk dilution data from all experiments collapsed to a reasonably consistent linear relationship based on non-dimensionalized radius. Similarly the minimum dilution was also found to be a linear function of non-dimensionalized radius. Dilution results are discussed in section 5.2.1.

Upper layer depths, discussed in section 5.2.2, were found to depend on the depth to diameter ratio ( $H/D$ ) and jet Froude number ( $F$ ), and increased in a parabolic manner with radius.

Both the stability Froude number and composite Froude number were very large ( $\gg 1$ ) for all experiments starting at small radius, and remained greater than 1 to the largest radius that measurements were made at in the present study, though they did decrease with radius. These two quantities indicate that an internal hydraulic jump was not present in the radially spreading flow, this is more fully discussed in section 5.2.5.

## 5.2 Results

### 5.2.1 Dilutions

The average dilutions calculated for each of the experiments is presented in figure 5.1. These dilutions are plotted against the total trajectory length ( $z/D$ ), which includes the vertical jet length and the distance into the radially spreading flow. From this plot it is immediately apparent that the mean or bulk dilution increases in an approximately linear manner with distance. Within each series of experiments, the densimetric Froude number and regular jet Froude number were varied, some minor differences in the dilution curves between experiments within a series is apparent. This suggests that one or other of these quantities may have a minor effect on the bulk dilution experienced by the radially spreading flow, though a systematic relationship for either of these quantities could not be determined. These minor differences between experiments may also be caused by scatter in the experimental data. Error bars are plotted only for experiment C1 to avoid cluttering the plot, the magnitude of these error bars are representative of those of the other experiments.

For comparative purposes, the predicted average dilution for a vertical free jet is superimposed on the bulk dilution results for the radially spreading flows. In order to develop an expression for the vertical jet dilution, the original data utilized by Fisher et al. (1979) for the region of  $z/l_0 < 15$  was analyzed. This data of measured dilution with distance within the zone of flow establishment was obtained from the studies of Hill (1972), Crow and Champagne (1971) and Albertson et al. (1950). The length of vertical jet available for entrainment was assumed to be 90% of the total depth, based on Lee & Jirka's (1979) predictions that the thickness of the surface impingement region was on the order of 10% of the total depth. The resulting formula for vertical jet dilution, which takes into account the surface blocking depth being approximately 10% of the total depth, is:

$$S_v = 0.254 \left( \frac{H}{D} \right) + \exp \left( -0.125 \frac{H}{D} \right), \quad 2 \leq H/D < 15 \quad (5.1)$$

This formula was obtained with a regression analysis of the data from the three studies mentioned above and has a coefficient of determination ( $r^2$ ) of 0.92. The data used in obtaining equation 5.1 and the equation are plotted in figure 5.2. The first term of equation 5.1 is the linear expression for dilution (equation 2.12) modified to an expression of  $H/D$  instead of  $z/l_q$  and assuming a blocking depth 10% of the total depth. Equation 5.1 has an initial value of 1 at  $H/D$  of 0, reflecting the theoretical expectation that  $S = \mu/Q_o = Q_o/Q_o = 1$  when the length of the vertical jet is zero ( $H/D = 0$ ). Of course, if the water were extremely shallow it may not be reasonable to expect that the radial flow would exist as conceptualized. Equation 5.1 implicitly assumes that entrainment into the vertical jet is unhindered by whatever conditions are occurring in the radial flow. As  $H/D$  becomes large equation 5.1 asymptotes to the linear relationship for dilution (represented by the dotted line in figure 5.2) beyond the zone of flow establishment. When the depth is great enough for the vertical jet to achieve established flow then equation 2.12 can be used to predict the vertical jet dilution at the entrance to the surface impingement region.

The bulk dilution curves for the radially spreading flow begin below the predicted dilution for the vertical free jet, see figure 5.1. This can be explained as follows. Firstly, as mentioned above, the dilution in the vertical jet region is probably less than for a free jet due to the physical configuration of the flow. Next it should be considered that in the surface impingement region little or no entrainment and dilution is occurring. So, the vertical free jet dilution curves should cut off at  $z/D$  of 5 for the A series experiments, 7.5 for the B series, and 15 for the C series. Actually, the cut off of vertical jet entrainment should occur even before this when the surface impingement region is considered, the portion of the jet trajectory through this region is inactive in terms of entrainment of ambient fluid. Theoretically, entrainment and dilution would not recommence until the

exit from the surface impingement region, which would be very close to where the dilution curves for the radially spreading flow begin. The transition from the vertical jet dilution curve to the radial jet dilution curve would take the form of a flat, horizontal line between the two curves representing a region in which little or no dilution is occurring.

The minimum dilution results follow a similar pattern as that for the bulk dilutions, though as one would expect the minimum dilution is less than the bulk dilution obtained, refer to figure 5.3. As in figure 5.1, error bars are plotted for only one experiment, these are representative of the errors for the other experiments. Again, the corresponding dilution curve for a vertical free jet is superimposed on the graph for comparative purposes. Note that the surface dilution occurs at a much slower rate than the dilution for the vertical jet region. It is interesting that the minimum dilutions calculated for the radially spreading jet happens to start almost right on the curve for the average dilution for the vertical jet. However, as was explained for the case of the average dilutions, entrainment into the vertical jet ceases at a  $Z/D$  less than the corresponding  $H/D$  for each series of experiments, due to the vertical flow entering the surface impingement region. Recall that it has been supposed that within the surface impingement region the flow becomes well mixed but no additional dilution occurs. This implies that the jet fluid is uniformly blended within the surface impingement region, and the average dilution is then equal to the minimum dilution upon exit from the surface impingement region, entrainment commences again at the bottom of the surface layer and a dilution (i.e. concentration) gradient is re-established. Also, the complete mixing within the surface impingement layer would result in the minimum dilution of the flow exiting the layer being greater than the minimum dilution of the flow entering the layer.

To facilitate analysis of the radial dilution data the dilution that occurs in the vertical jet region was removed, to remove the effect of the different  $H/D$  ratios and allow direct comparison of all experiments.

The vertical jet dilutions calculated using equation 5.1 were 1.8 for series A, 2.3 for series B and 4.0 for series C. By subtracting the appropriate vertical jet dilution ( $S_v$ ) from the bulk dilution ( $S$ ) the dilution data should then represent that of a radial jet as if it originated at the surface, and the vertical portion were not present, the resulting dilution data is referred to as the radial dilution ( $S_R$ ). The radial jet dilution is plotted against non-dimensionalized radius ( $R/D$ ) in figure 5.4. With the vertical jet dilution removed the dilution data collapses to a reasonably close grouping of data. The line of best fit to this data was:

$$S_R = S - S_v = 0.576 \left( \frac{R}{D} - 2.85 \right) \quad (5.2)$$

The coefficient of determination ( $r^2$ ) was 0.90 for this line of best fit, which is plotted with the data in figure 5.4. The right hand side of equation 5.2 within the brackets can be expressed as a new quantity, the effective radius  $R'$ , essentially a coordinate shift to a virtual origin for the radial flow:

$$R' = \frac{R}{D} - 2.85 \quad (5.3)$$

The value of  $R/D = 2.85$  for the virtual origin of the radially spreading flow represents the value obtained from the best fit to the dilution data, where  $S_R = S - S_v = 0$ . When the effective radius is substituted into equation 5.2 it then becomes:

$$S_R = S - S_v = 0.576R' \quad (5.4)$$

That the radial dilution varies linearly with radial distance is a reasonable result and is consistent with the equations used for predicting dilution in vertical jets, where mean dilution beyond the zone of flow establishment is a linear function of distance. Equation 5.4 indicates that the rate of increase in dilution with distance is much greater in

the radial flow than for a vertical jet. Recall equation 2.12 where the bulk dilution for a vertical jet,  $S = 0.25z/l_0 = 0.28z/D$ , the results for the radial flow, equation 5.2 indicate that dilution occurs at a rate of  $0.576R/D$ , approximately twice as fast for an equivalent distance. This is partially explained when the available surface area for entrainment is considered, with a vertical jet the characteristic width of the jet velocity profile is  $0.107z$ , so at any given location the surface area for an infinitesimal length ( $dz$ ) of vertical jet that entrainment can occur into is of the order of  $2\pi(0.107zdz) = 0.67zdz$ . With the radial jet the available surface area is  $2\pi R dR = 6.3R dR$ , so a much greater surface area is available to the radial jet. This comparison used the characteristic width of the velocity profile of the vertical jet where the velocity in the vertical jet decreases to  $1/e$  of the centerline value. Even if a width two or three times greater were assumed for the vertical jet, the radial jet would still have much greater surface area through which entrainment could occur. Of course surface area is not the only factor, the characteristic velocities are also important in entrainment.

The complete expression for bulk dilution is, when equation 5.1 is substituted into equation 5.4:

$$S = 0.254 \left( \frac{H}{D} \right) + \exp \left( -0.125 \frac{H}{D} \right) + 0.576R' \quad (5.5)$$

Some small differences remain between experiments, possibly due to differences in jet or densimetric Froude numbers or measurement errors, but these differences proved hard to factor out in a systematic fashion. Despite the inability to remove the minor differences between experiments, equation 5.4 predicts the radial dilution well, for the range of densimetric and jet Froude numbers investigated in this study.

The minimum dilution data was analyzed in the same manner as described above for the bulk dilution data. The relationship obtained for the minimum dilution is of the same form as that for the bulk dilution:

$$S_{\min} - S_v = S_{R\min} = 0.47 \left( \frac{R}{D} - 2.5 \right) \quad (5.6)$$

This equation is plotted with the experimental data in figure 5.5. The coefficient of determination of the linear regression was 0.82. The resulting fit is not as good as for the bulk dilution data, and the virtual origin is slightly different. It was not possible to factor out the small differences between experiments by investigating either Froude numbers or depth to diameter ratios.

### 5.2.2 Upper Layer Depths

For the purposes of the present investigation the interface between the radially spreading upper layer and the return flow in the lower layer was defined as occurring where the radial velocity changed direction ( $h$ ). Because of some irregularities in the radial velocity profiles in the vicinity of the interface, particularly at profiles closest to the tank wall, the velocity profiles were first smoothed by a moving average that progressed downward from the top most point in the profile.

The interface depths ( $h$ ) for each experiment are plotted as a function of the non-dimensionalized radius ( $R/D$ ) in figure 5.6. In figure 5.7 the interface depth has been non-dimensionalized by the jet port diameter ( $h/D$ ) and plotted against the non-dimensionalized radius ( $R/D$ ). The slope (growth rate) of the upper layer appears to increase with increasing radius. The initial slope of the interface is larger for experiments with smaller  $H/D$  ratios. As the upper layer accounts for a relatively greater proportion of the total depth with smaller  $H/D$  ratios, the increased shear encountered in these cases may account for the faster upper layer growth rates. While not directly proportional to radius it is apparent that the upper layer depth increases with increasing radius, the effect is non-linear and appears to be parabolic. It is apparent that there is an  $H/D$  ratio effect, so this quantity should appear in any expression for  $h/D$ . Similarly the differences between

experiments sharing the same depth to diameter ratio suggests that the jet Froude number has an effect as well.

The non-linearity of the upper layer depths suggested that they would be a parabolic function of the effective radius. A theoretical development of the upper layer growth expression from Ho & Heurre (1984) is described in Appendix A. From this theoretical development the general form that was investigated for the upper layer depths was:

$$\frac{h-h_o}{H} = c \frac{R-R_o}{H} + \frac{1}{2} c^2 \left( \frac{R-R_o}{H} \right)^2$$

For consistency with the bulk dilution results (equation 5.4) the effective radius as defined by equation 5.3 was used where  $R_o = 2.85D$ . The growth rate coefficient  $c$  was shown by Lawrence et al. (1991) to be of the order of 0.14 for a mixing layer, this value was used in the investigation of upper layer depths. Depths corresponding to radii from less than 6 port diameters ( $R/D < 6$ ) were eliminated from each of the series prior to the analysis since these points exhibited a high degree of curvature and were thought to be subject to influence from the surface impingement region. The resulting equation of best fit for the data was:

$$\left( \frac{h-h_o}{H} \right) = 0.10 \frac{R-R_o}{H} + \frac{1}{2} \left( 0.10 \frac{R-R_o}{H} \right)^2 \quad (5.7)$$

The line of best fit, and the data from which it was obtained, are plotted in figure 5.8. The linear regression had an  $r^2$  value of 0.79. The value of  $c$  obtained (0.10) is slightly lower than that reported by Lawrence et al. (1991), but is of the same order of magnitude. Thus the upper layer depth data conforms well to the theoretical extension of Ho & Heurre's (1984) theory for the growth of mixing layers. The growth of the upper layer is governed by the velocity ratio between the upper and lower layer. The theoretical

initial upper layer depth, corresponding to the virtual origin at  $R_o = 2.85D$  was also a product of the linear regression and was:

$$\frac{h_o}{H} = 2F^2 \left( \frac{H}{D} \right)^{-1} \quad (5.8)$$

Interestingly equation 5.8 can be expressed as a kind of Froude number, when the expression for the jet Froude number is substituted in and equation 5.8 is simplified:

$$\frac{h_o}{H} = 2 \frac{U_o^2}{gD} \left( \frac{D}{H} \right) = 2 \frac{U_o^2}{gH} = 2F_H^2 \quad (5.9)$$

This new Froude number ( $F_H$ ) can be considered an expression of the initial strength of the vertical jet to the total water depth. The non-dimensionalized initial upper layer depth ( $h_o/H$ ) is proportional to the square of this “depth” Froude number ( $F_H$ ). For a given depth, the initial upper layer depth increases with the square of the initial jet velocity.

There remains some scatter in the data plotted in figure 5.8. This is likely a reflection of the sensitivity of the upper layer depths to error in the velocity profiles, from which the upper layer depths were determined. An error of relatively small magnitude in the velocity profiles could displace the apparent interface depth significantly, since in most velocity profiles the radial velocity changes from positive to negative at a relatively shallow angle.

### 5.2.3 Velocity and Temperature Profiles

Except for the differences in the magnitudes of the radial velocities and the upper layer depths where the radial velocity changed direction, the velocity profiles were very similar amongst all experiments. Figure 5.9, from experiment B2, is typical of the velocity profiles found for all experiments, the composite velocity profiles for all experiments are contained in Appendix C. These profiles are in the raw form prior to the

application of the moving average for profile smoothing, which was discussed in Chapter 4. Generally the velocity varied nearly linearly over the depth, except for some curvature in the vicinity of the interface and presumably at the surface where the velocity gradient would have to become zero. While the velocity in the upper layer varies nearly linearly with depth, in the lower layer, except for a small region immediately below the interface, the velocity profile is essentially uniform.

As for the velocity profiles, the temperature profiles are similar between experiments, though the magnitudes and depths are again different depending upon the initial jet parameters. The composite temperature profiles for experiment B2 are plotted in figure 5.10, composite plots of the temperature profiles for all experiment are located in Appendix D. Again, these are raw profiles that have not been smoothed. Generally the temperature in the upper layer varies in a nearly linear fashion from a maximum to the ambient temperature in the lower layer. Some curvature is evident in the vicinity of the interface. Surface points are not plotted as they were estimated from Chen's (1980) theoretical profile, as was discussed in Chapter 4.

It was not necessary to obtain specific equations to predict the average upper layer velocity, as it is possible to calculate this quantity with the equations for bulk dilution and upper layer depth. The average upper layer velocities calculated using equations 5.5 and 5.9 are plotted against the original average upper layer velocity data in figure 5.11. This figure demonstrates that this method provides a reasonable method of estimating the average upper layer velocity, particularly at large radii (small velocity values) where the estimated and original values are very close.

### **5.2.5 Froude Numbers**

The composite Froude numbers, as plotted in figure 5.12, decrease linearly with radius when the abscissa is on a log scale. There appears to be some depth to diameter ratio effect in the slopes of the lines for each series, while the actual magnitude

(separation between lines) for individual experiments within each series appear to depend on the initial conditions of the jet ( $F$  &  $F_o$ ).

The composite Froude number values are greater than 1 over the entire range of radii for which measurements were made for all experiments. While decreasing with increasing radii, the composite Froude number values are never less than 1 for the range of radii investigated for any experiment. Equally important is that the sudden change in composite Froude number from greater than 1 to less than 1, which is a property of internal hydraulic jumps, is not present. Even if an internal hydraulic jump were to be present beyond the region where measurements were made, significant dilution would have occurred before that point is reached by the radial jet.

Comparison of the four experiments that share the same jet Froude number, experiments A1, A2, B2 and B3, where  $F = 0.9$  allows some observations of the effects of both the densimetric Froude number and  $H/D$  ratio. Increases in the densimetric Froude number result in an increase in the composite Froude number. This is not surprising when one recalls that the densimetric Froude number and the composite Froude number are very similar in form, they are restated here as a reminder. The densimetric Froude number is:

$$F_o = U_o / (g'_o D)^{1/2} \quad (2.8)$$

And the composite Froude number is:

$$G^2 = \frac{U_v^2}{g'h} + \frac{U_L^2}{g'(H-h)} \quad (3.5)$$

If the jet Froude number is held constant and only the densimetric Froude number is increased, then only  $g'_o$  is changed (decreases). Since dilutions are known to be relatively unaffected by the densimetric Froude number in the present study, we can expect a direct linkage between  $g'_o$  and  $g'$  in the radially spreading flow. It is known

from the examination of upper layer depths in the present study that a change in the densimetric Froude number has no apparent effect there. Therefore a change in the densimetric Froude number should have an almost corresponding effect on the composite Froude number ( $G^2$ ), one should expect that  $G^2 \propto F_o^2$ .

In calculating the stability Froude number the equation used was altered slightly. Instead of using the average upper layer velocity, which is the equivalent velocity assuming a top hat profile in the upper layer, the maximum or surface velocity was used. This approach was used since the upper layer does not have a uniform velocity but approximates a mixing layer, as if it were between the lower layer and an imaginary layer with a uniform velocity above it equal to the maximum velocity of the radially spreading flow. The modified versions of equation 3.6 for the stability Froude numbers becomes:

$$F_{\Delta}^2 = \frac{\Delta U^2}{g'H} = \frac{(U_{\max} + |U_L|)^2}{g'H} \quad (5.10)$$

While it is possible to calculate the composite Froude number (and the bulk Richardson number, discussed in the next section) from the time averaged velocities and upper layer depths, it may be worth considering whether this is in fact realistic or if it leads one to forget the true intermittent and discontinuous nature of the upper layer flow. For all experiments the stability Froude number (equation 5.11) was greater than 1 at all radii, refer to figure 5.13:

$$F_{\Delta}^2 = \frac{(U_{\max} + |U_L|)^2}{g'H} > 1$$

Recall from chapter 3 that the internal Froude number depends on the stability Froude number:

$$F_I = \frac{U_U(H-h) + U_L h}{\sqrt{g'h(H-h)H(1-F_{\Delta}^2)}} \quad (3.7)$$

Therefore, if the stability Froude number is greater than 1, the internal Froude number is actually complex and the flow is unstable. While it may be mathematically possible to calculate the composite Froude number under this condition, the interface doesn't really exist for internal long waves to act along and the results of internal hydraulics can't be applied, which is essentially what the flow visualization experiments of Fisher (1995) and MacLatchy (1993) had indicated. The combination of the composite Froude number remaining greater than 1, even though gradually decreasing, and the stability Froude number also being greater than 1 (i.e. no real interface) is a very strong indication that internal hydraulic jumps are not going to be present.

In Appendix A it was shown that the extension of the composite Froude number to radial flow configurations was possible when entrainment was neglected. In fact entrainment is also neglected in the definition of internal wave speeds for planar two layer flows. Whether it is still valid to use the same formulation when entrainment is occurring is not clear. However, there will still be a tendency on the part of researchers to discuss flow conditions in terms of this quantity despite its potential weakness in entraining radial flows, so its results are included here. Consideration of just what exact form a composite Froude number should take for such a radial flow may be moot though. It is clear from the stability Froude number (an inverse of the bulk Richardson number) that the interface is highly unstable and a high degree of entrainment is occurring. These conditions may effectively block the propagation of internal long waves along the interface and make the whole issue of flow criticality and the presence or not of an internal hydraulic jump irrelevant. The flow is far more jet like than it is a stratified flow in the near field.

### **5.2.6 Bulk Richardson Numbers**

For consistency with the modified definition used for the stability Froude number, where the surface or maximum velocity ( $U_{\max}$ ) was substituted for the average upper layer velocity, this modification was also made in calculating the bulk Richardson

number for the radially spreading flow. With this modification the bulk Richardson number more closely represents the velocity difference across the depth of the upper layer and the shear that is produced by this velocity difference. It can be shown that this modification also makes the bulk Richardson number an approximation of the gradient Richardson number, which is arguably more appropriate for describing the situation where velocity and density varies approximately linearly through the upper layer. The gradient Richardson number was defined as:

$$Ri_g = -\frac{g \frac{\partial \rho}{\partial z}}{\rho \left( \frac{\partial u}{\partial z} \right)^2} \quad (3.1)$$

Assuming near linear profiles over the depth of the radial flow,  $h$ , substituting discrete quantities for infinitesimal, and recognizing that the total velocity difference between the upper and lower layer is  $\Delta U = U_{\max} + |U_L|$  the following approximation can be made:

$$Ri_g = -\frac{g \frac{\partial \rho}{\partial z}}{\rho \left( \frac{\partial u}{\partial z} \right)^2} \approx -\frac{g \frac{\Delta \rho}{h}}{\rho \left( \frac{\Delta U}{h} \right)^2} \approx \frac{g'h}{\Delta U^2} \quad (5.11)$$

So the formulation of the bulk Richardson number employed here to approximate the gradient Richardson number is:

$$Ri_b = \frac{g'h}{\left( U_{\max} + |U_L| \right)^2} \approx Ri_g \quad (5.12)$$

To avoid confusion with the true gradient Richardson number as defined by equation 3.1 the approximation provided by equation 5.13 shall continue to be referred to as the bulk Richardson number as it considers the upper layer flow as a whole. However,

equation 5.13 is better adapted to linear variations in velocity and density as opposed to uniform profiles.

It appears that the bulk Richardson numbers increase approximately linearly with radius when plotted on a log scale, see figure 5.14. As the bulk Richardson number is essentially an inverse form of the composite Froude number this result is not surprising in light of the results of the previous section where the composite Froude number decreased in a linear fashion on a log scale.

For all experiments, throughout the radial extent for which measurements were made, the Richardson number is less than the recognized critical value of 0.3 (Turner (1973), Lawrence et al. (1991)) or indeed the critical value of 0.25 for the gradient Richardson number should this quantity be more appropriate. As for the stability Froude number, the results indicate that the upper layer flow does not have a stable interface, and entrainment can be expected. With increasing radius the bulk Richardson number increases toward the critical value for stability of the interface but the diameter of experimental tank was not large enough for this point to be reached.

### **5.3 Comparison to Entrainment Hypothesis**

The results of the present study are consistent with the entrainment hypothesis as discussed by Turner (1986). For stratified flows Turner (1986) suggests that the entrainment velocity should be proportional to the velocity difference between the two layers:

$$U_e \propto \Delta U \quad (5.13)$$

If the velocity difference is taken to be  $\Delta U = U_U + |U_L|$ , then:

$$U_e \propto U_U + |U_L| \quad (5.14)$$

The entrainment velocity was calculated from the dilution data using the following equation:

$$U_e = \frac{\Delta Q}{\Delta R} \frac{1}{2\pi R} \quad (5.15)$$

The entrainment velocities calculated from the experimental dilution data are plotted in figure 5.15 as a function of the velocity difference  $\Delta U$ . The first two points have been removed from each data set to eliminate the influence of any initial conditions near the surface impingement region. The entrainment velocity is a well defined linear function of the velocity difference, with a correlation coefficient of 0.91. The linear regression formula for the entrainment velocity as a function of the velocity difference is:

$$U_e = 0.13(\Delta U - 1.25) \text{ (cm/s)} \quad (5.16)$$

The entrainment coefficient (proportionality constant) relating the entrainment velocity to the velocity difference is 0.13. On first inspection the presence of a constant (intercept = 1.25 cm/s) in equation 5.17 is unusual, however it suggests that when the velocity difference has become sufficiently small the entrainment velocity becomes negligible, even though there may still be a measurable velocity difference (small velocities correspond to large radii). This is consistent with the theoretical expectation that there is a critical Richardson number above which large scale entrainment into the radially spreading surface flow will subside. A specific critical value for the bulk Richardson number has not been identified for the case of the radially spreading flow, but the relationship between the entrainment velocity and the velocity difference suggests that a critical threshold governing the cessation of large scale entrainment exists. While the entrainment hypothesis suggests that the entrainment velocity should be directly proportional to the velocity difference the result above is consistent with the principle while incorporating the concept of a critical Richardson number above which entrainment subsides.

### 5.4 Comparison to Previous Studies

The results of the present study are limited to a maximum radial distance of 1.66  $R/H$  for series C and 2  $R/H$  for series A and B. Lee & Jirka model dilution as halting at the start of the internal hydraulic jump at 0.6  $R/H$ . Wright et al. (1991) provide dilution results at a radial distance of approximately 3  $R/H$ , where they assume the cessation of entrainment into the density jump. In Table 5.1, dilution predictions made using the formulations of Lee & Jirka (1981) and the data of Wright et al. (1991) for the conditions of the experiments of the present study are compared to the maximum (farthest radii) bulk dilutions results from the present study. Also dilutions from the present study, corresponding to 0.6  $R/H$  are compared to those predicted by Lee & Jirka's formulation at  $R/H = 0.6$ , where they assume entrainment ceases. The predicted dilutions for the experiments of the present study obtained using the formulations of Lee & Jirka (1981) and Wright et al. (1991) are plotted against the measured dilutions from the present study in figure 5.16. Series A experiments could not be predicted using Lee & Jirka's or Wright et al.'s formulations as they were not able to handle the situation where the vertical jet has not become fully established before reaching the surface (i.e. for these models to work  $H > 6D$ ), so series A is not considered in these comparisons.

Complicating the comparison between the results of the present study and Wright et al. (1991) is that the model of Wright et al. breaks down when trying to predict dilutions for situations where  $l_M/H > 3$ . The numerical solution employed by Wright et al. failed to converge at large  $l_M/H$ , unfortunately most of the experiments of this study have  $l_M/H > 3$ . Attempts to make the model described in their paper work to allow comparison were not successful. For comparison to the present study the trends obtained from the experimental results of Wright et al. are utilized. This introduces some error due to extrapolation, but facilitates comparison.

Because Lee & Jirka (1981) do not allow for significant entrainment into the radially spreading flow beyond  $R/H = 0.6$ , final dilutions predicted with their model are

considerable less than those obtained in the present study at the farthest radii at which measurements were made. For the B series experiments the data of Wright et al. (1991) are similar to that obtained in the present study, but for the C series the dilutions are much higher from Wright et al. than those obtained from the present study. It should be remembered that the dilutions of Wright et al. represent final values, theoretically occurring at larger  $R/H$  than where the values from the present study were measured.

Lee & Jirka's (1981) model was able to function when reconstructed in a computer spreadsheet. In their model entrainment ceases at  $0.6 R/H$ , dilutions obtained at this distance for experiments in the B and C series are indicated in Table 5.1.

It is possible to modify the model of Lee & Jirka's (1981) formulation by moving the start of the internal hydraulic jump out to larger radii. Moving the start of the internal hydraulic jump out to the position corresponding to the last dilution measurement for the B and C series experiments ( $R/H = 2$  and  $1.66$  respectively), allows dilution to be modeled up to these larger radii. When this modification is done the dilution calculated by the model for these positions is of the same order to that measured in the present study. The values obtained with this modification of Lee & Jirka (1981) are contained in Table 5.1 for comparison to the dilution values of the present study. The upper layer depths obtained with these positions are also included, but are on the order of one half of the corresponding values obtained in the present study. Also the dilutions calculated for  $R/H = 0.6$  using Lee & Jirka's original formulations are similar to those obtained from the present study for the corresponding position. To the extent that it models entrainment into the radial flow, Lee & Jirka's formulation appears to produce reasonable results.

To extend the results of the present study to larger radii, dilutions, upper layer depths, composite Froude numbers and bulk Richardson numbers were extrapolated using equations 5.5, 5.9, 5.10 and 5.12 respectively. The results for the experiments of the present study were extrapolated using these equations and are plotted as functions of the radius non-dimensionalized by the total depth ( $R/H$ ). In addition the corresponding

approximate data from Lee & Jirka (1981) experiment number 9 ( $H/D = 11$ ,  $F = 7$ ,  $F_o = 11$ ), discussed in section 3.3.5.1, is superimposed upon the plots to allow comparison with the predictions and results of the present study.

The predicted bulk dilutions (equation 5.5) for the experiments of the present study are plotted in figure 5.17 as a function of  $R/H$ . The estimated bulk dilutions from Lee & Jirka (1981) experiment number 9, as discussed in section 3.3.5.1, are superimposed on the plot for comparative purposes. The predicted dilutions for the experiments of the present study increase linearly indefinitely. Clearly, there would be practical limits on the dilution increasing continuously in this manner, but the radial extent of the present study was not great enough to identify where the dilution relationship would change. The bulk dilution approximated for experiment 9 of Lee & Jirka (1981), which has an  $H/D$  between those of the B and C series of the present study, has an initial value higher than that of the experiments of the present study but does not increase as rapidly, and ends up much less than those of the present study at  $R/H > 3$ .

The upper layer depths, predicted with equation 5.9, become a significant proportion (approximately half) of the total depth at  $R/H$  between 3 and 4, refer to figure 5.18. Note that at small  $R/H$  the superimposed upper layer depth data of Lee & Jirka experiment 9 is similar to that of the predictions using the results of the present study. The upper layer depths of experiment 9 of Lee & Jirka (1981) ceased growing at  $R/H$  slightly greater than 2, and  $h/H$  of approximately 0.35-0.40. Thereafter there was a slight decrease in the upper layer depths for Lee & Jirka experiment. Yet this point does not mark an internal hydraulic jump, the composite Froude number remains greater than 1 to radii larger than that where the cessation of upper layer growth apparently occurs (refer to figure 5.19).

The predicted composite Froude numbers from the present study, and those estimated from Lee & Jirka (1981) experiment 9 are plotted in figure 5.19. The surface or maximum velocity was estimated as being twice the average upper layer velocity, that

was calculated using the predicted dilution (equation 5.5) and upper layer depth (equation 5.9). As  $R/H$  increases the composite Froude numbers predicted for the experiments of the present study decrease gradually, until on the order of 2-4  $R/H$  (depending upon experimental parameters), and the composite Froude number levels off and then begins increasing with  $R/H$ . The increase in composite Froude number once beyond a certain  $R/H$  coincides with the upper layer depth becoming a significant proportion of the total depth and indicates that the predictive relationships are not valid for these conditions. The composite Froude numbers from Lee & Jirka (1981) experiment 9 initially are much higher than those for the present study, probably due to the very large jet Froude number ( $F = 7$ ) for this experiment, and while generally decreasing, remain greater than 1 to the largest  $R/H$  for which data was available.

The bulk Richardson number (equation 5.12) was also predicted using the relationships obtained in the present study, and is plotted in figure 5.20. It is worth noting that the predicted/extrapolated values of the bulk Richardson number peak below that of the expected critical Richardson number (0.3 or even 0.25 if the gradient Richardson number is considered), before the values begin declining again with increasing  $R/H$ . The predictive equations are probably no longer valid in this range. The peak in the predicted bulk Richardson number is different for each experiment. Only one experiment (B2) approaches the accepted critical bulk Richardson number value of 0.3, with a peak value of the order of 0.2. It is possible that the critical value of bulk Richardson number for a radially spreading flow is considerably different from the accepted value. The values of bulk Richardson number from Lee & Jirka (1981) experiment 9 follow a similar pattern to the predictions for the experiments of the present study, and also peak well below 0.3.

Also, it should be considered that the gradient Richardson number could be a more appropriate formulation for a surface jet configuration such as in the present study, due to the velocity and density gradients that are present. Even so the Richardson

numbers predicted here fell short of the critical value of gradient Richardson number, 0.25.

### 5.5 Summary of Results

The dilution results and predictive model obtained in the present study are consistent with the entrainment hypothesis first proposed by Morton, Taylor & Turner (1956). The entrainment velocity, the rate at which ambient fluid is entrained into the radial flow, is a linear function of the velocity difference between the surface (maximum) velocity of the upper layer and the average velocity of the lower layer. Equation 5.16 and figure 5.15 indicate that there is a threshold velocity difference below which entrainment into the radial flow is curtailed:

$$U_e = 0.13\Delta U - 0.17 \text{ (cm/s)} \quad (5.16)$$

Dilution of the radial flow is a linear function of radial distance, and the dilution rate is constant for a given set of conditions:

$$S = 0.254\left(\frac{H}{D}\right) + \exp\left(-0.125\frac{H}{D}\right) + 0.576R' \quad (5.5)$$

The observed growth of the upper layer is in agreement with an extension of the model for the growth of mixing layers reviewed by Ho & Heurre (1984), see Appendix B. The upper layer growth depends on the velocity ratio between the two layers and is a parabolic function of the effective radius:

$$\left(\frac{h-h_o}{H}\right) = 0.10\frac{R-R_o}{H} + \frac{1}{2}\left(0.10\frac{R-R_o}{H}\right)^2 \quad (5.7)$$

Where:

$$\frac{h_o}{H} = 2F^2\left(\frac{H}{D}\right)^{-1} \quad (5.8)$$

The results of the present study refute the existence of an internal hydraulic jump in the radial buoyant jet region. This conceptual approach to the radially spreading surface flow is incorrect as demonstrated by the composite Froude numbers. The radial flow remains internally super-critical throughout the radial extent investigated. When the internal hydraulic jump component is removed from the model of Lee & Jirka (1981) it more realistically predicts the dilution experienced by the radially spreading surface flow. Wright et al. (1991) was conceptually correct in recognizing significant entrainment into the radially spreading flow, but the terminology used in that study in describing the radial surface flow suggests the existence of a "density jump" and is misleading if not altogether incorrect.

<b>Experiment</b>	<b>B2</b>	<b>B3</b>	<b>B4</b>	<b>C1</b>	<b>C2</b>
( $l_M/H$ )	2.5	3.3	4.6	2.9	3.70
Dilution at $R/H = 0.6$ of present study	2.8	3.0	3.6	7.6	8.9
Dilution predicted from Lee & Jirka (1981) ( $R/H = 0.6$ ) (start of internal hydraulic jump)	4.1	4.1	4.1	8.2	8.1
Maximum $R/H$ of present study	2	2	2	1.66	1.66
Dilution at maximum $R/H$ of present study	8.4	8.8	11.6	15.0	18.5
Dilution predicted by modified Lee & Jirka (1981) (maximum $R/H$ of present study)	12.3	12.2	12.2	20.5	20.4
Dilution from data of Wright et al. (1991) ( $R/H=3$ )	15	17	13	34	30
Upper layer depth at maximum $R/H$ of present study (cm)	7.8	7.5	9.2	7	9.6
Upper layer depth predicted by modified Lee & Jirka (1981) (cm)	4	4	4	3.3	3.3

Table 5.1: Comparison of results of Lee & Jirka (1981), Wright et al. (1991) and the present study.

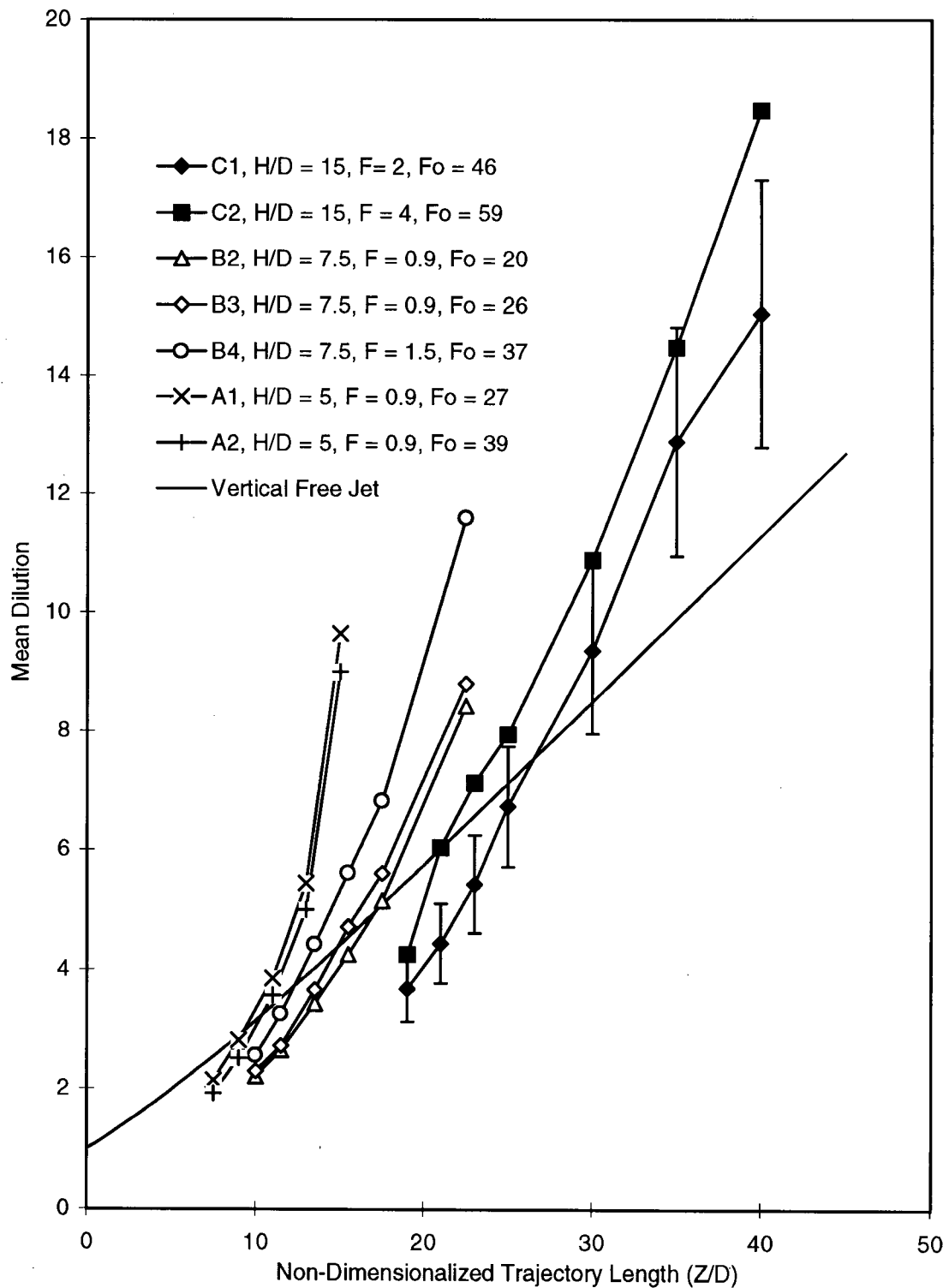


Figure 5.1: Time averaged mean dilution results for individual experiments (average of all replicates) as a function of non-dimensionalized trajectory length ( $Z/D$ ). Error bars for experiment C1 are representative of those for other experiments.

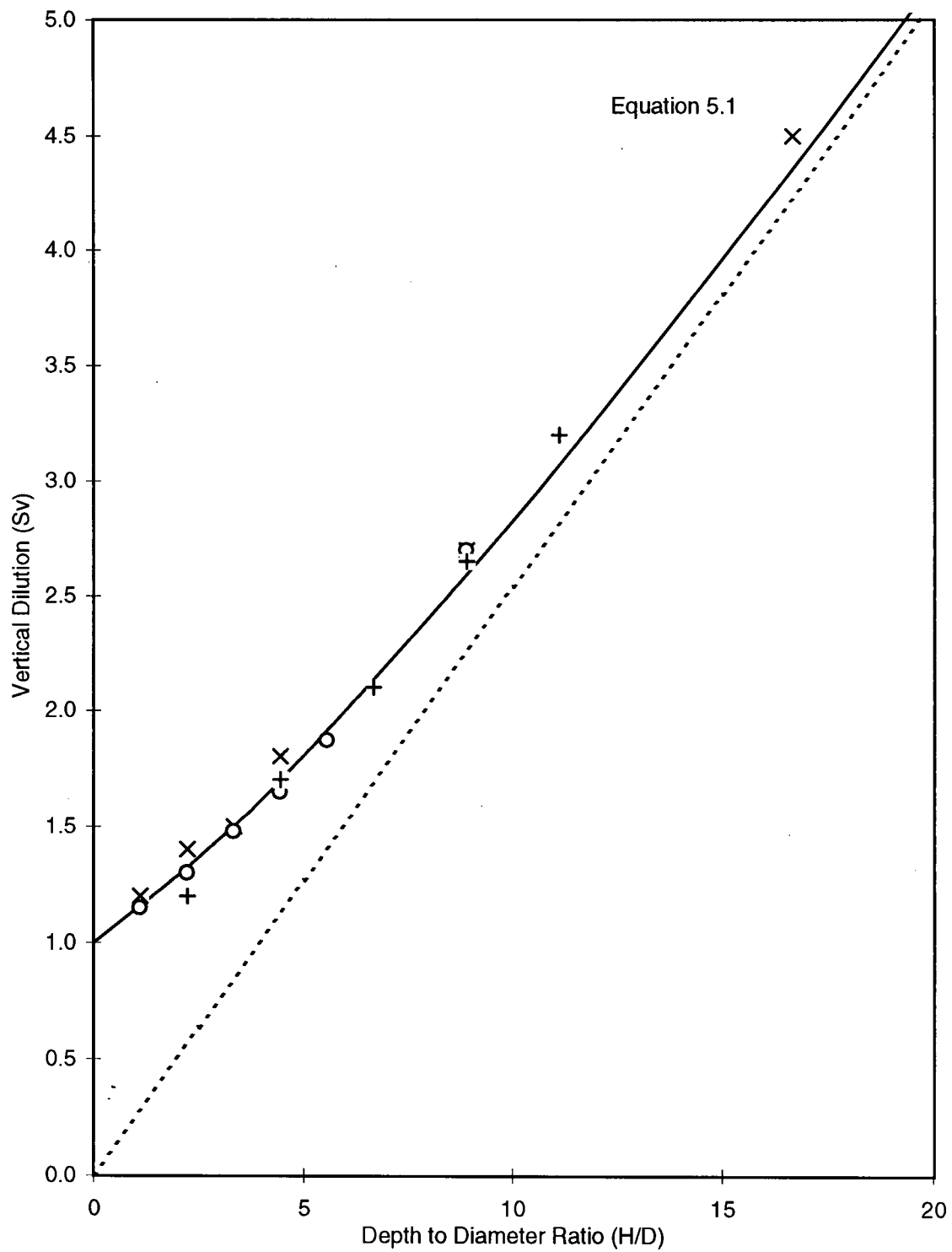


Figure 5.2: Dilution results from Hill (1972) (+), Crow and Champagne (1971) (o) and Albertson et al. (1950) (x) for the zone of flow establishment, plotted as a function of  $z/D$ .

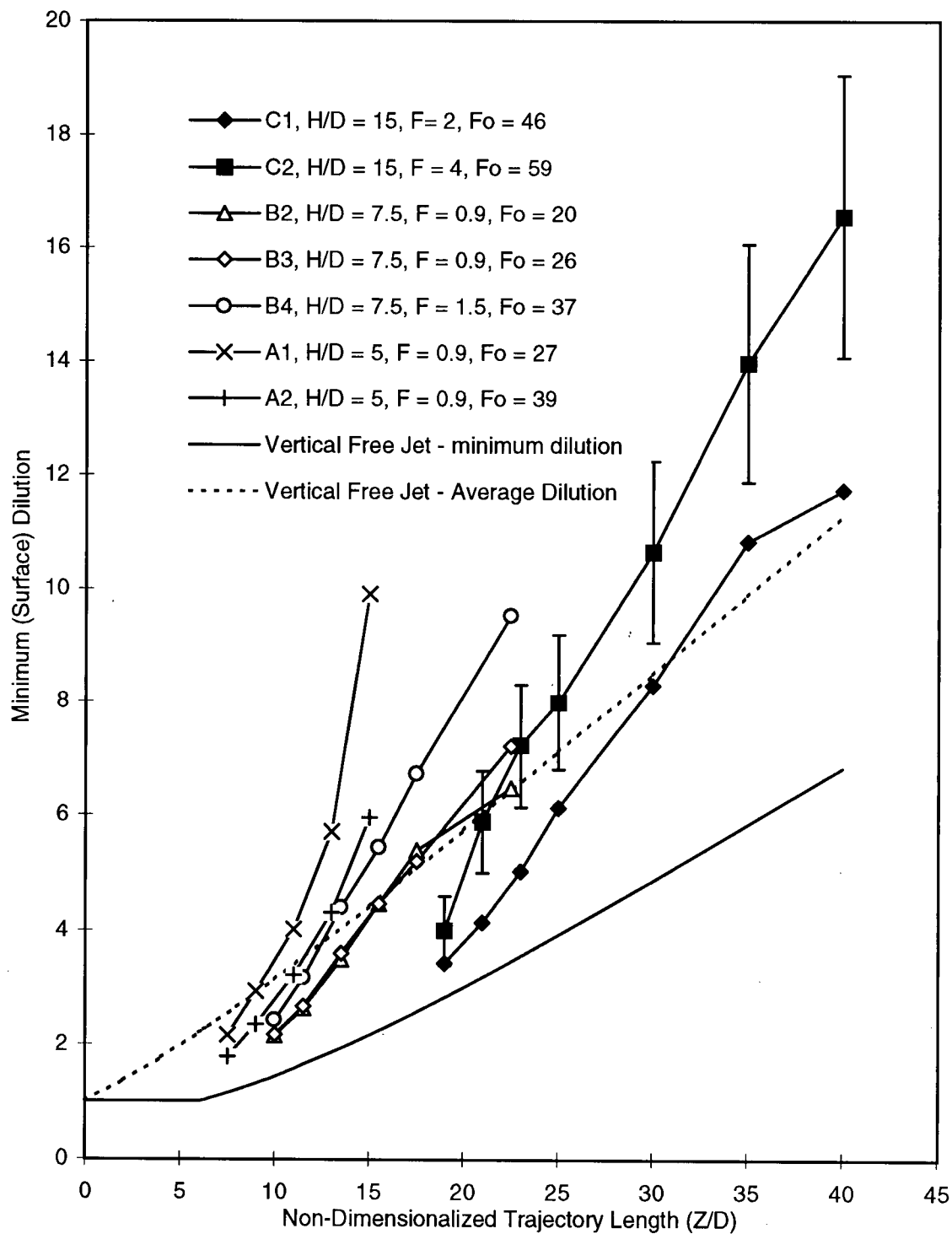


Figure 5.3: Time averaged minimum dilution results for individual experiments (average of all replicates) as a function of non-dimensionalized trajectory length ( $Z/D$ ). Error bars for experiment C2 are representative of those for other experiments.

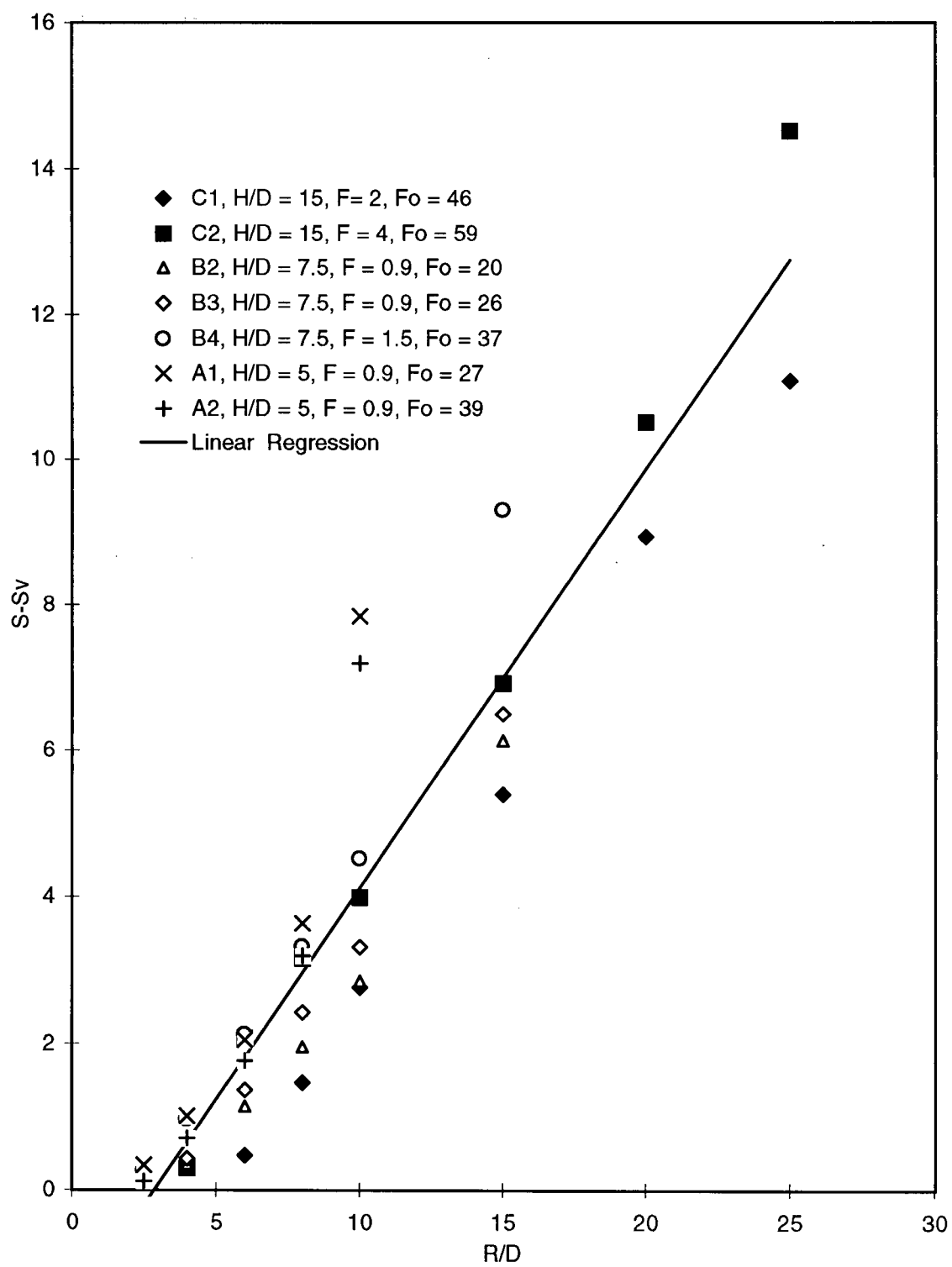


Figure 5.4:  $S - S_v$  plotted as a function of  $R/D$ .

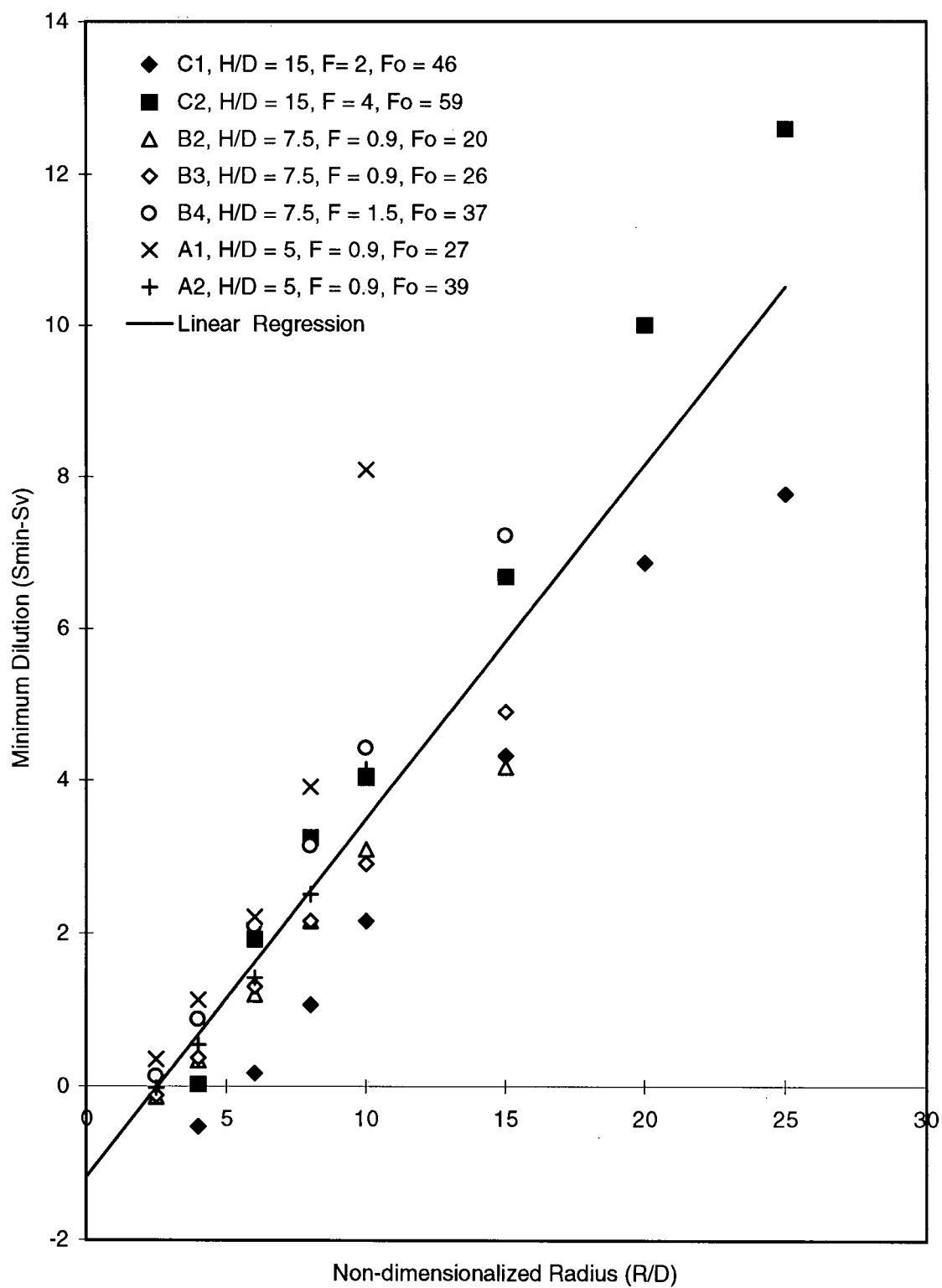


Figure 5.5:  $S_{min} - S_v$  plotted as a function of  $R/D$ .

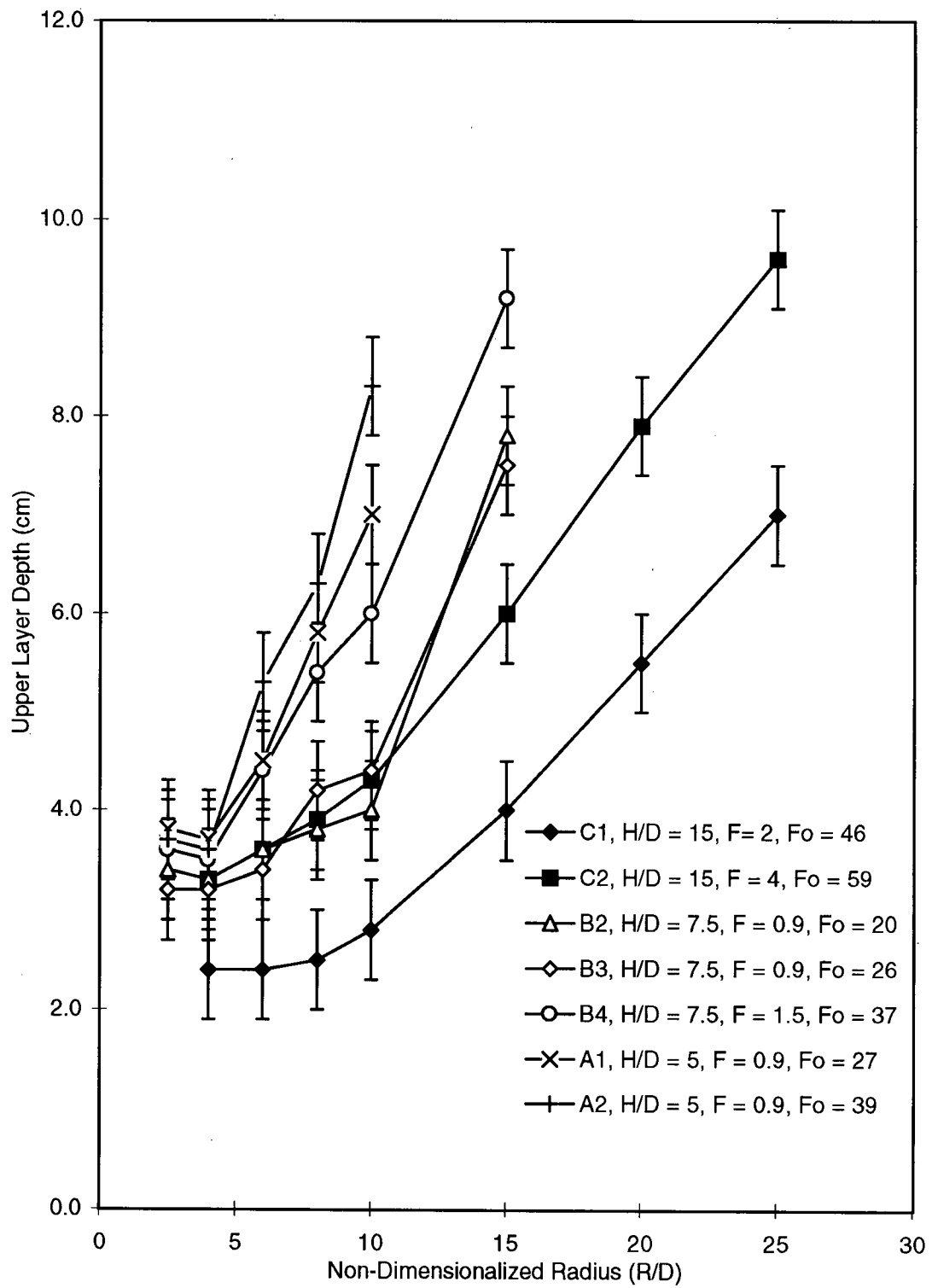


Figure 5.6: Upper layer depth plotted as a function of non-dimensionalized radius.

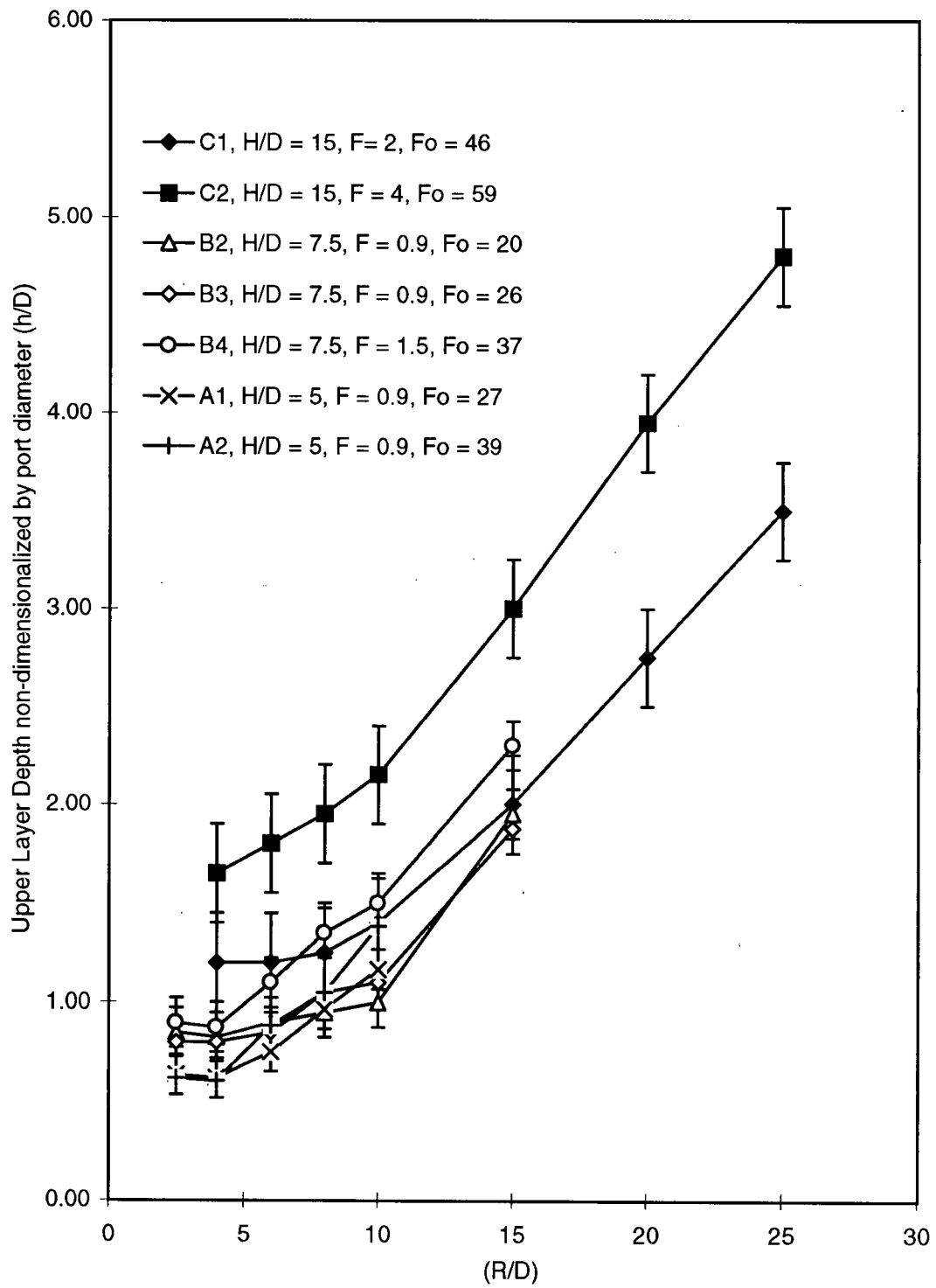


Figure 5.7: Non-dimensionalized upper layer depth ( $h/D$ ) plotted as a function of non-dimensionalized radius.

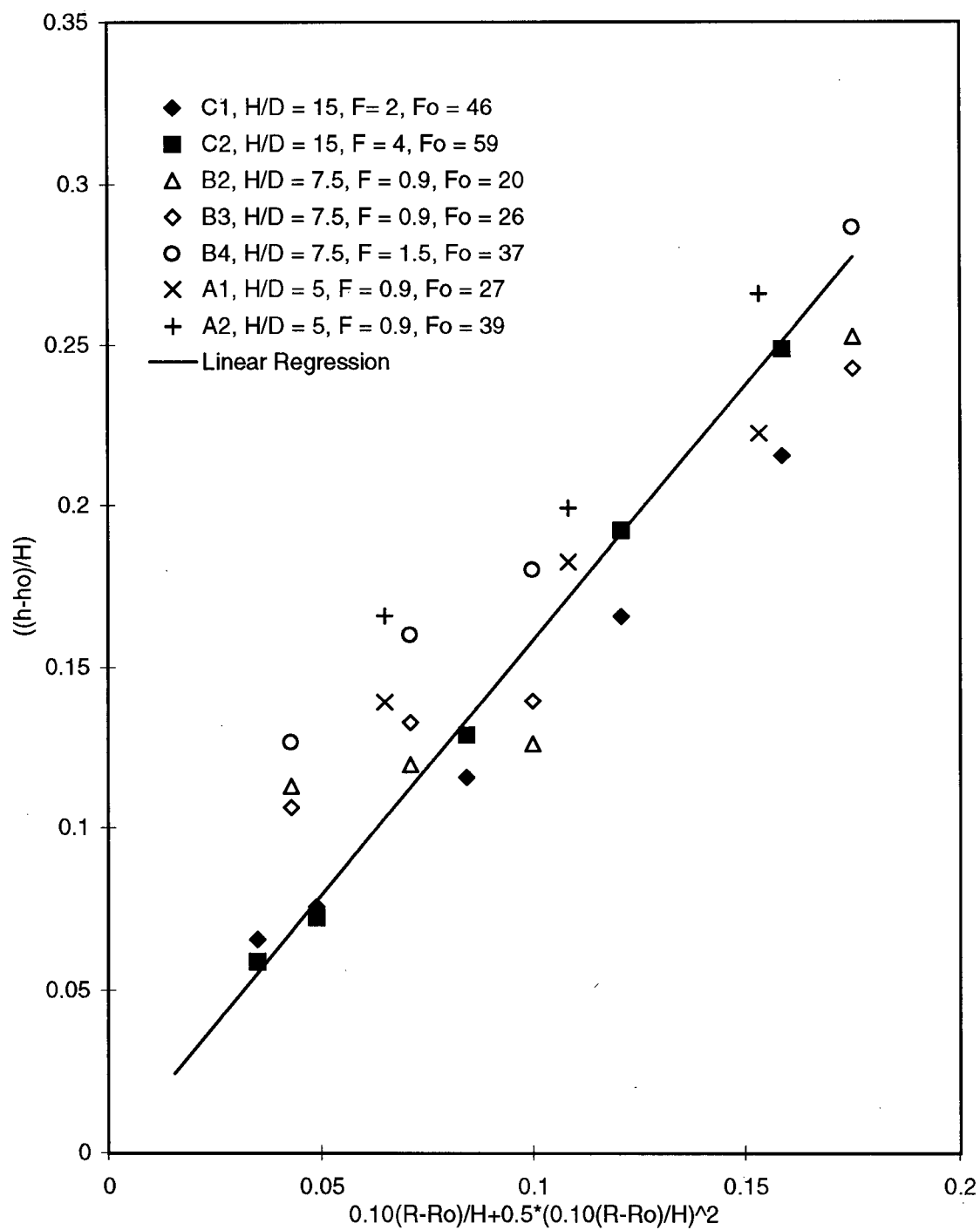


Figure 5.8:  $\left(\frac{h-h_o}{H}\right)F^{-1/2}\left(\frac{H}{D}\right)^{1/2}$  plotted as a function of  $0.10\left(\frac{R-R_o}{H}\right) + \frac{1}{2}\left(0.10\frac{R-R_o}{H}\right)^2$ .

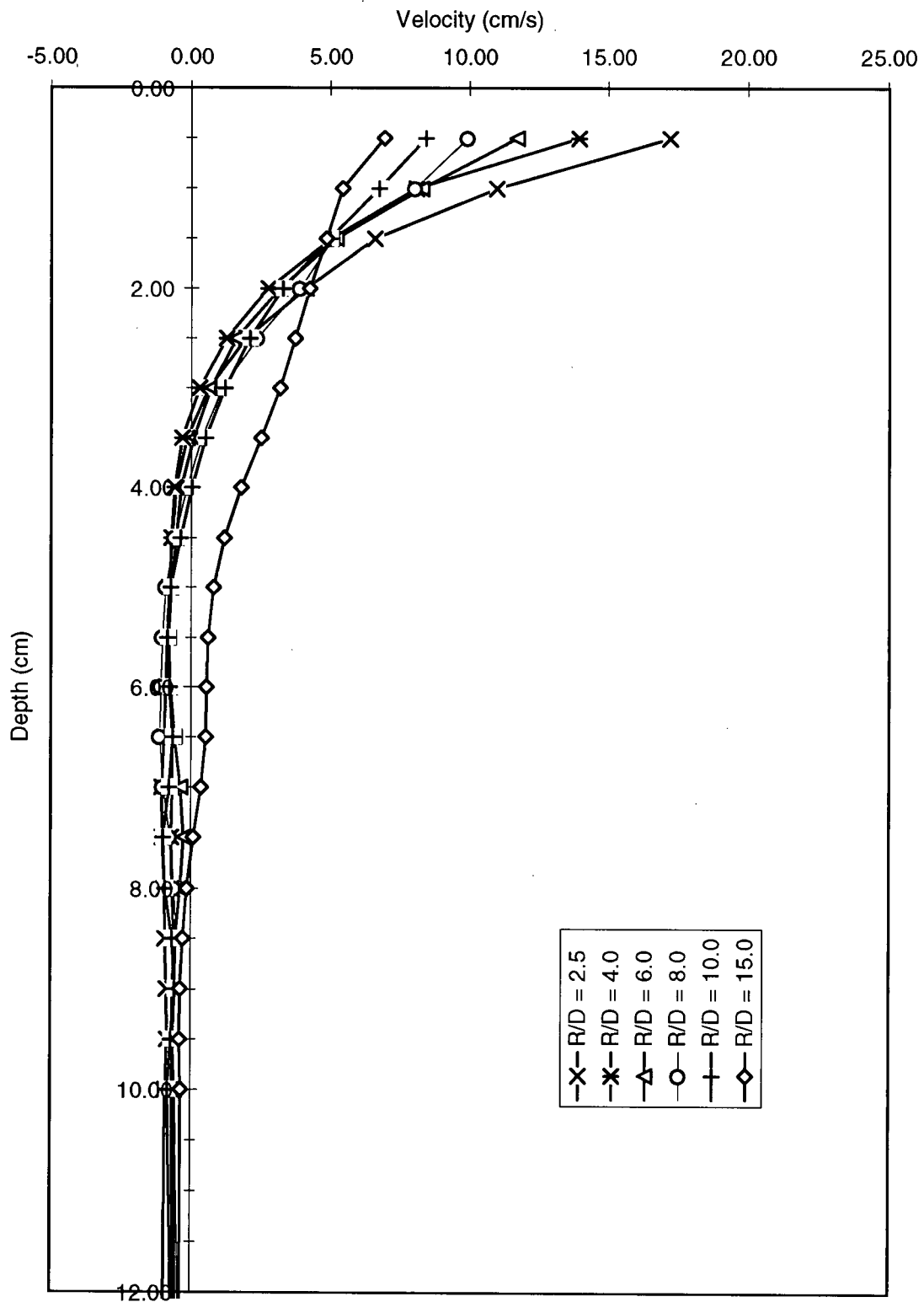


Figure 5.9: Composite plot of smoothed velocity profiles for experiment B2.

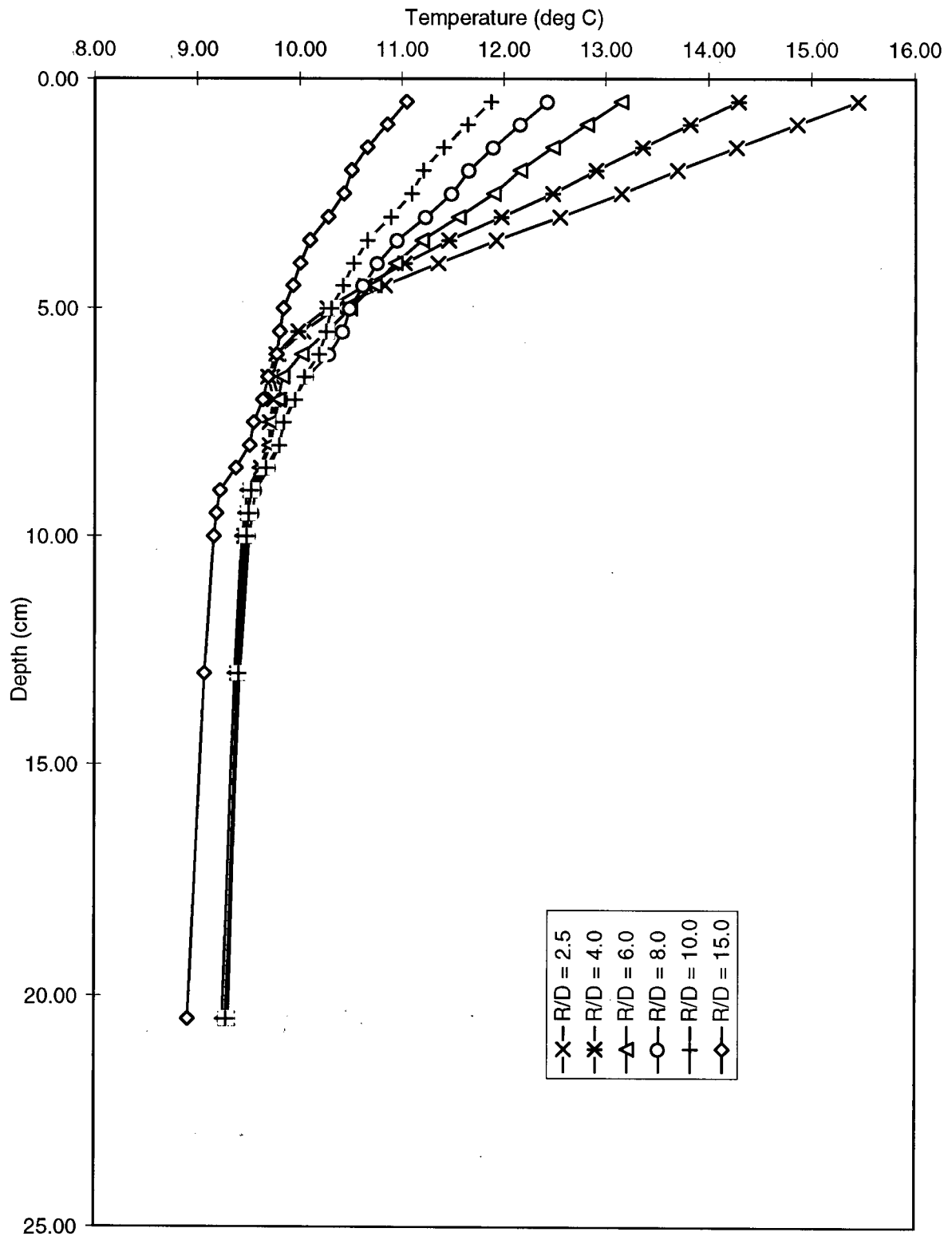


Figure 5.10: Composite plot of smoothed temperature profiles for experiment B2.

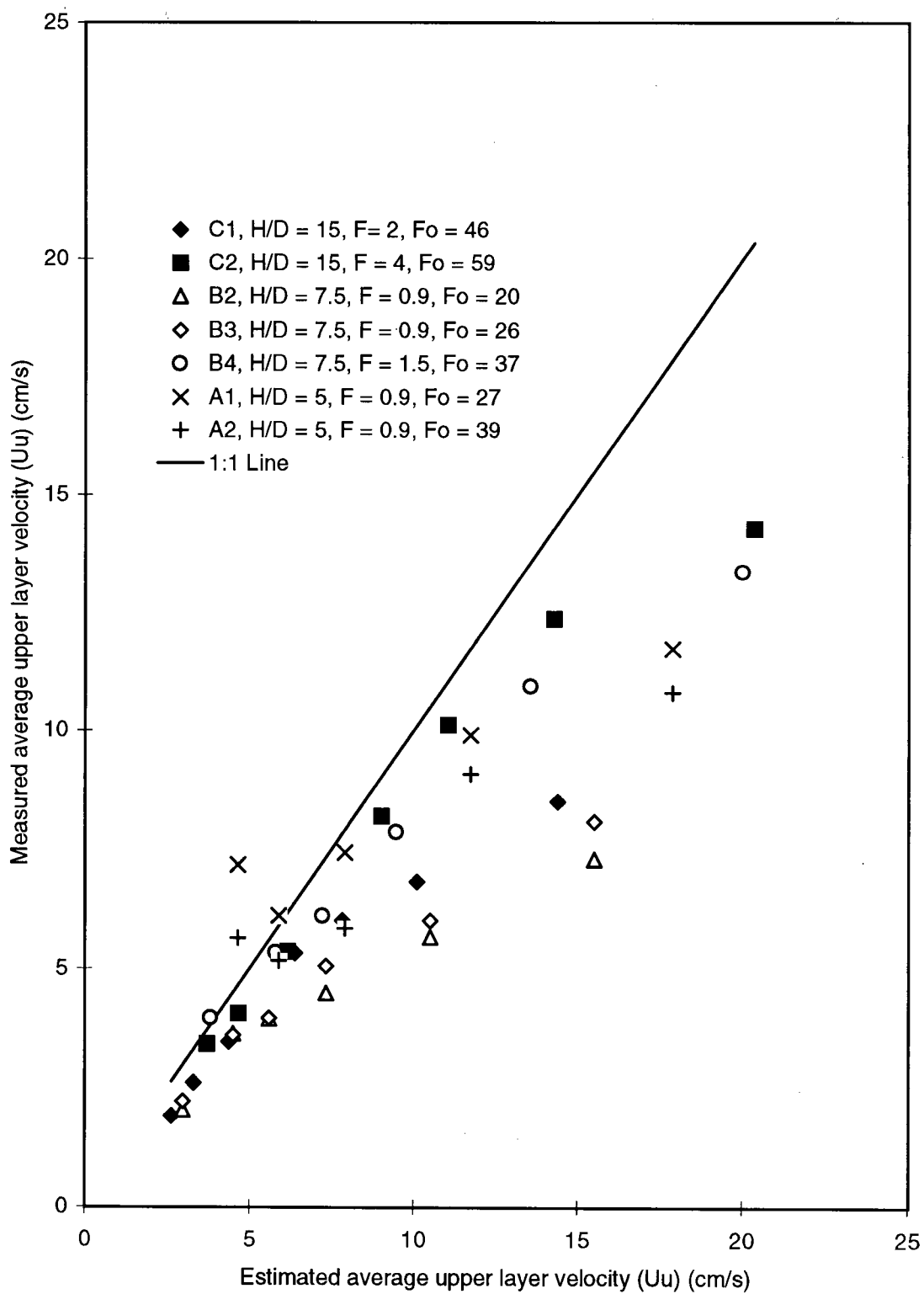


Figure 5.11: Original average upper layer velocity plotted against average upper layer velocity calculated using equations 5.5 and 5.9.

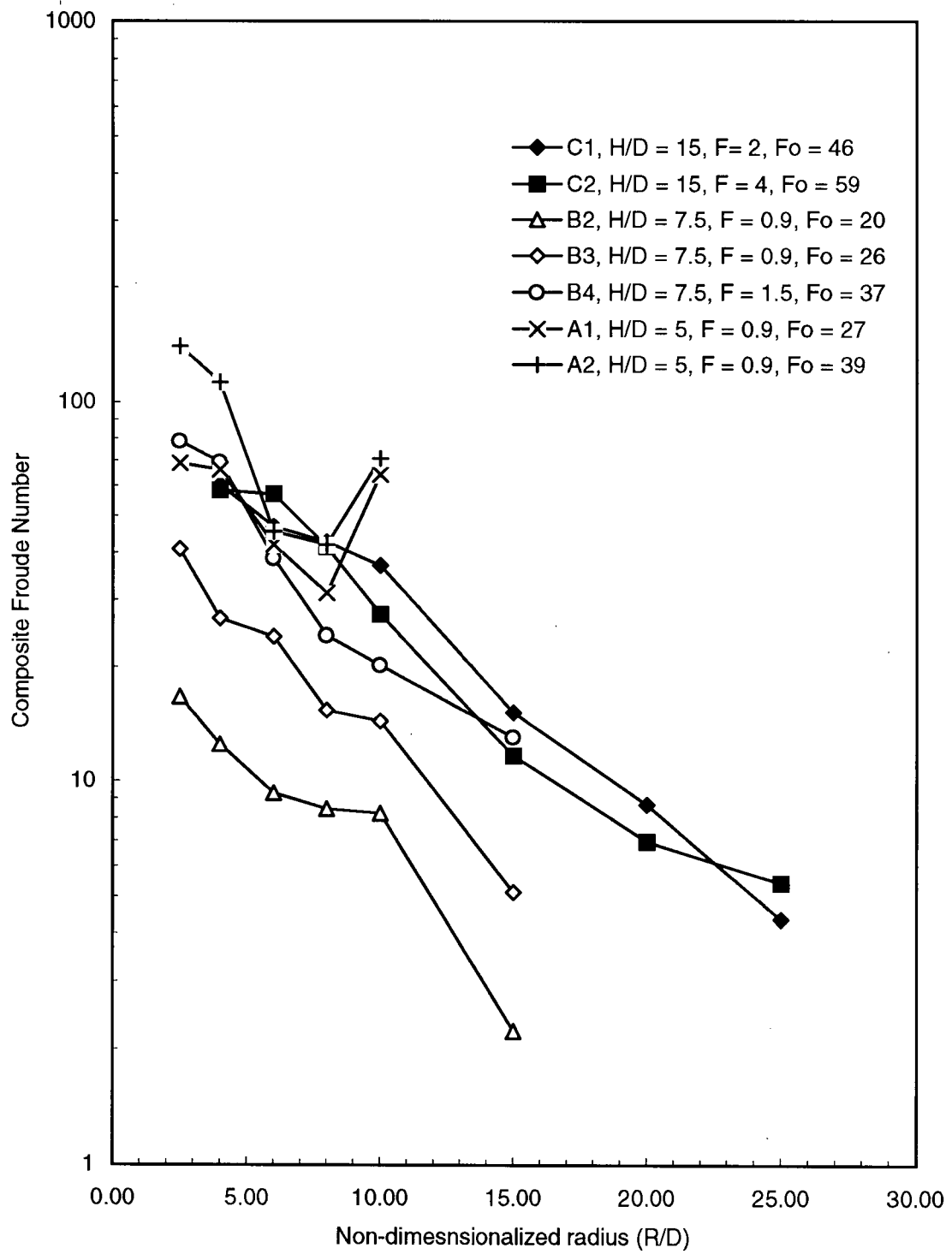


Figure 5.12: Composite Froude number as a function of non-dimensionalized radius.

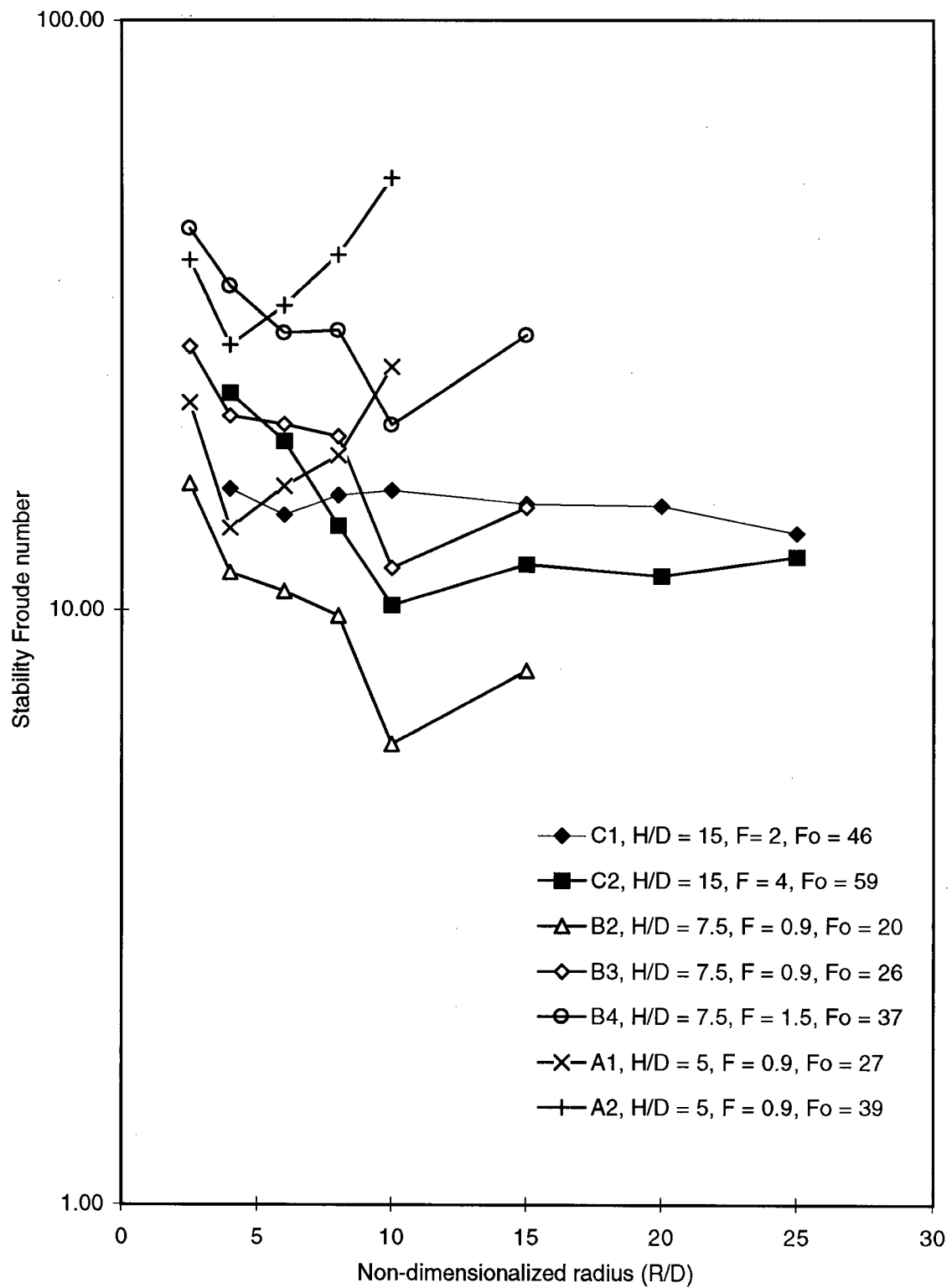


Figure 5.13: Stability Froude number plotted as a function of non-dimensionalized radius.

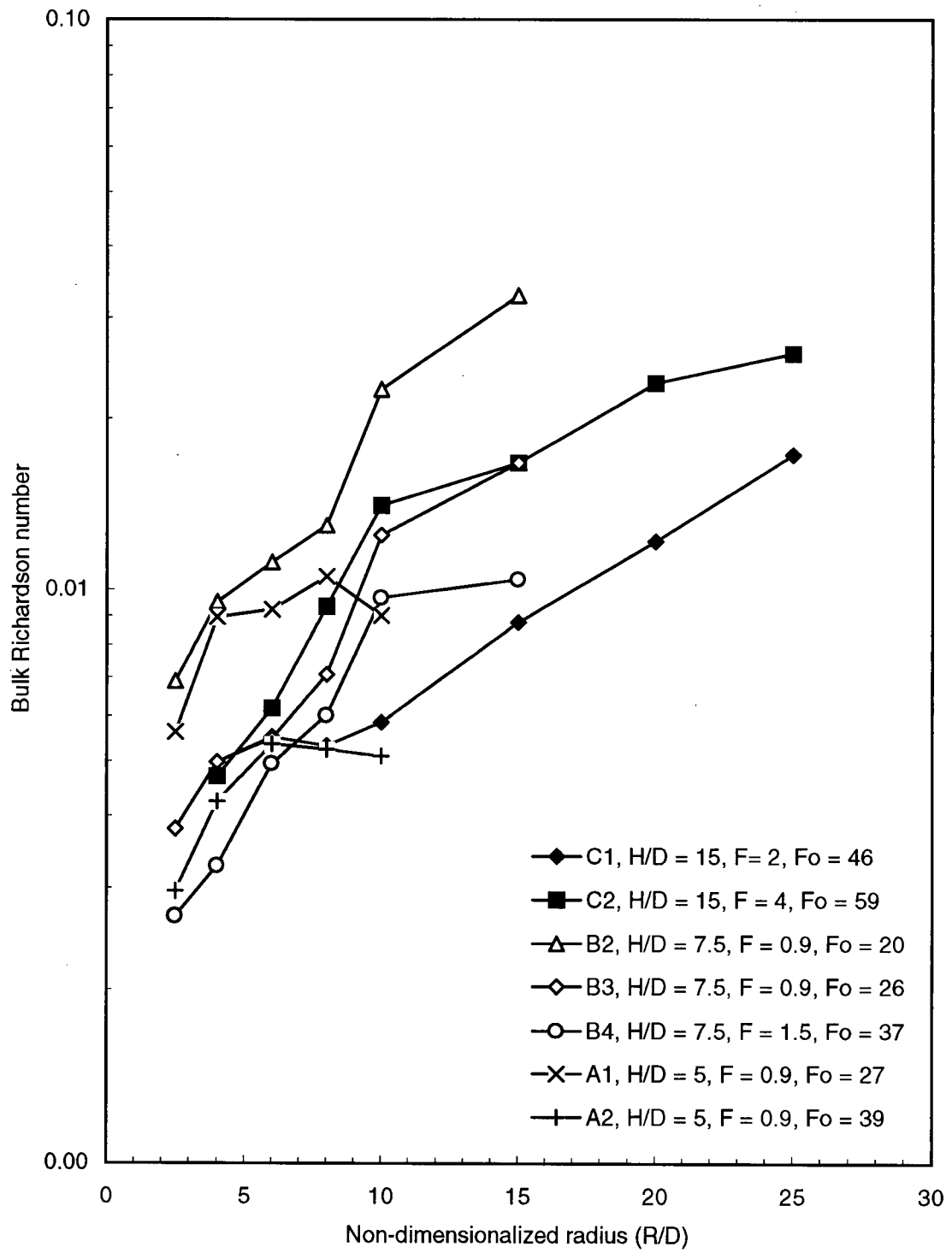


Figure 5.14: Plot of bulk Richardson number as a function of non-dimensionalized radius.

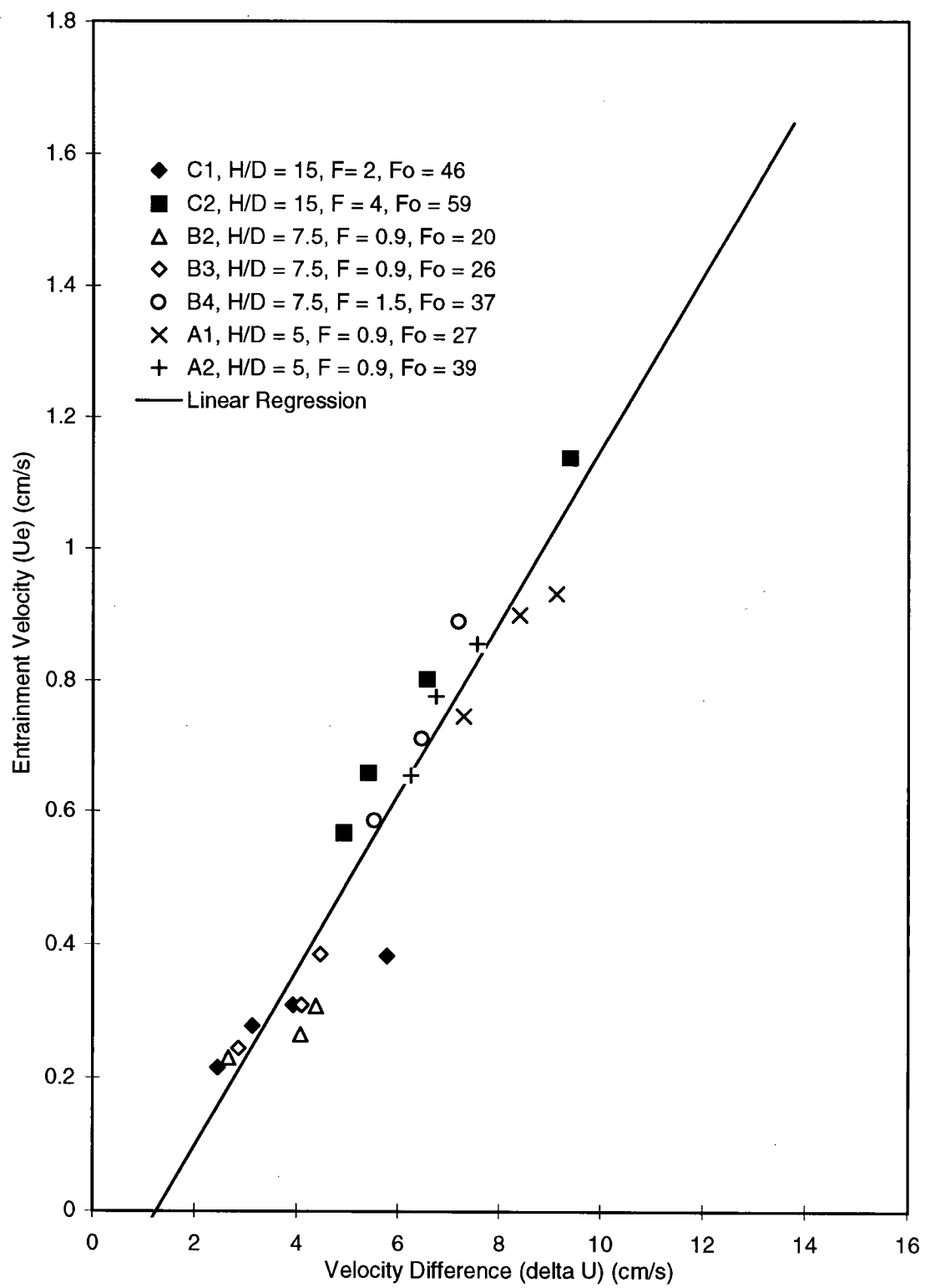


Figure 5.15: plot of entrainment velocity ( $U_e$ ) as a function of velocity difference ( $\Delta U$ ).

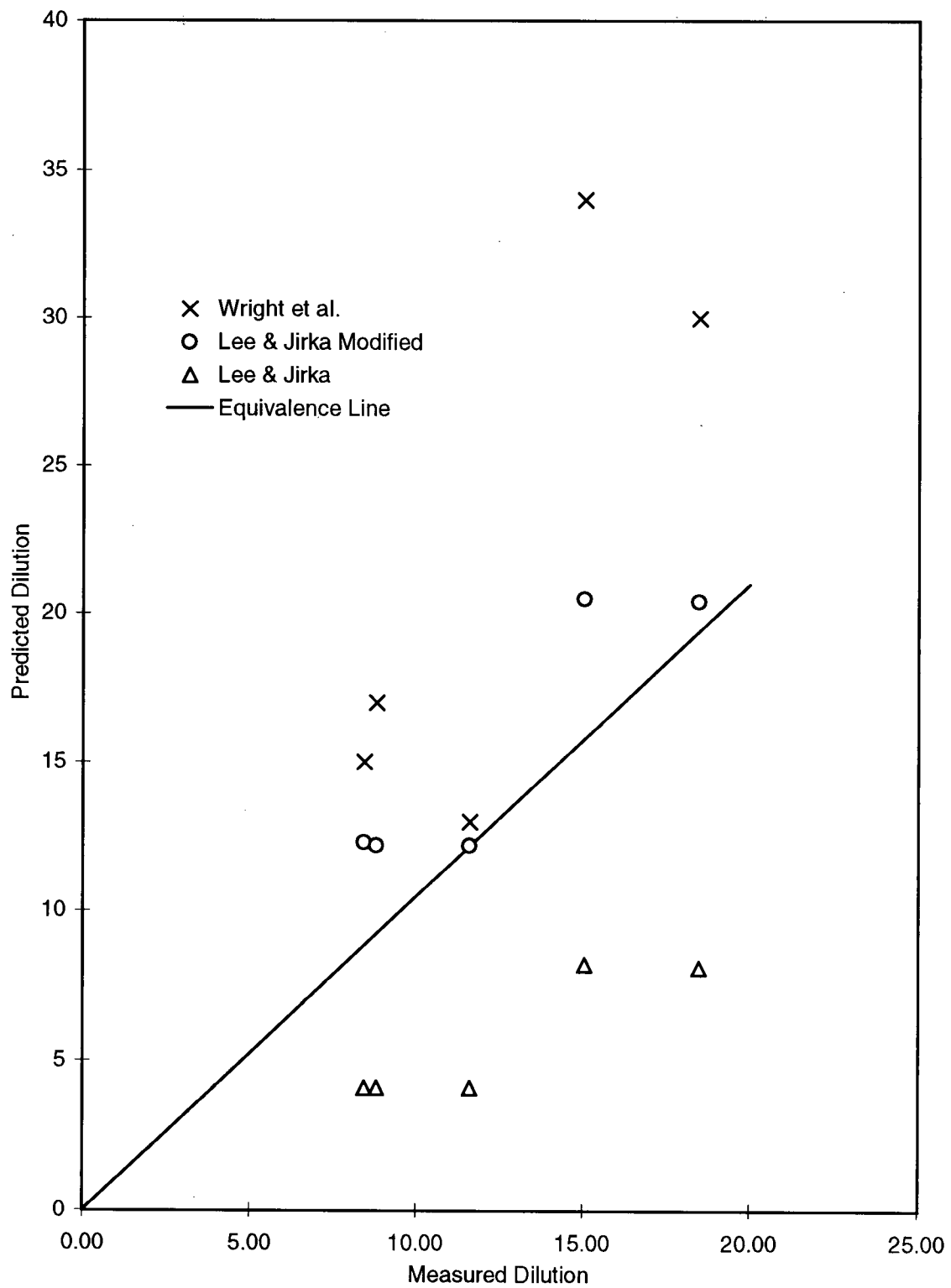


Figure 5.16: Comparison of final dilution results from Lee & Jirka (1981), Lee & Jirka modified, Wright et al. (1991) and the present study.

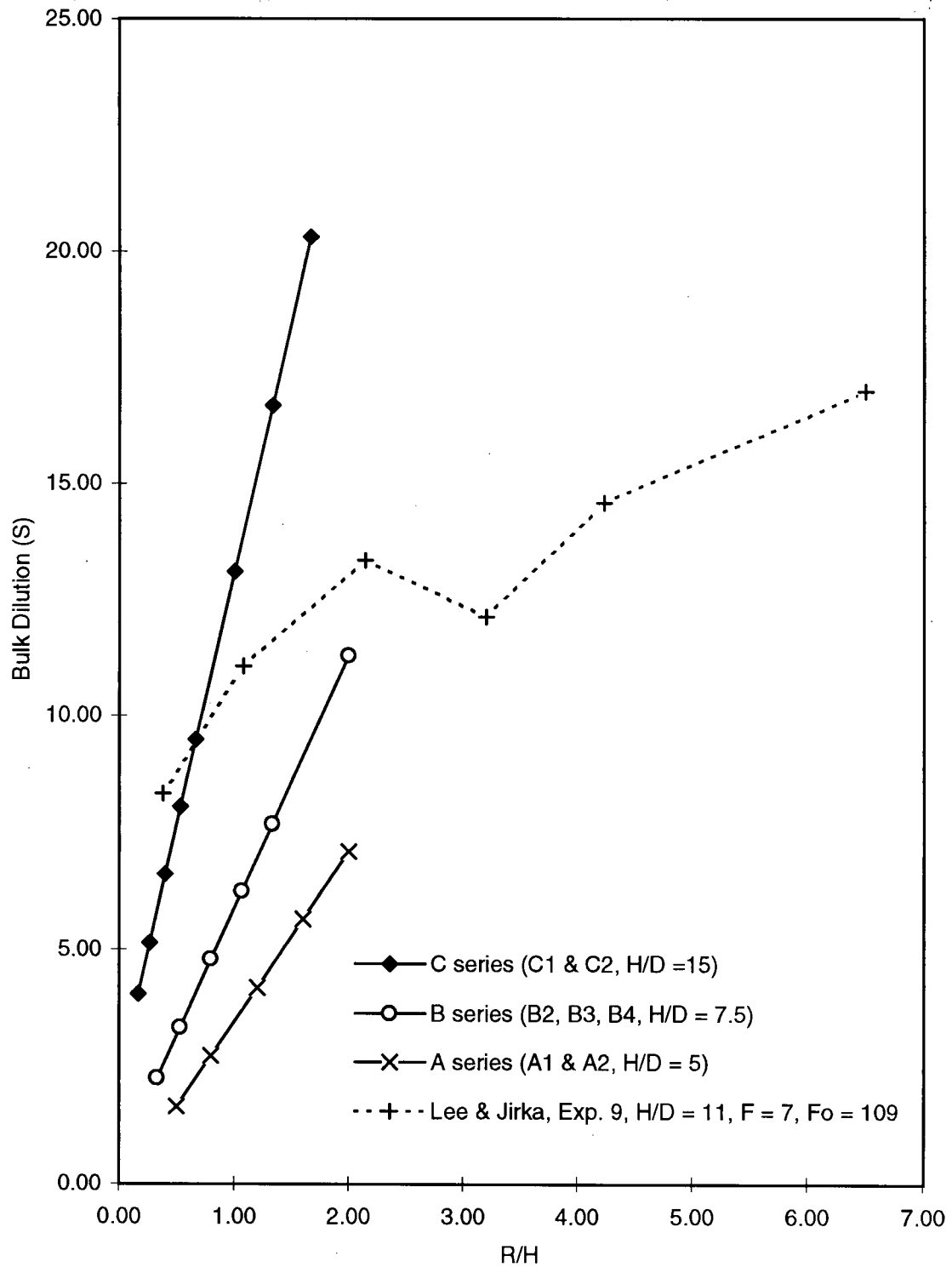


Figure 5.17: Plot of predicted bulk dilution as a function of  $R/H$ .

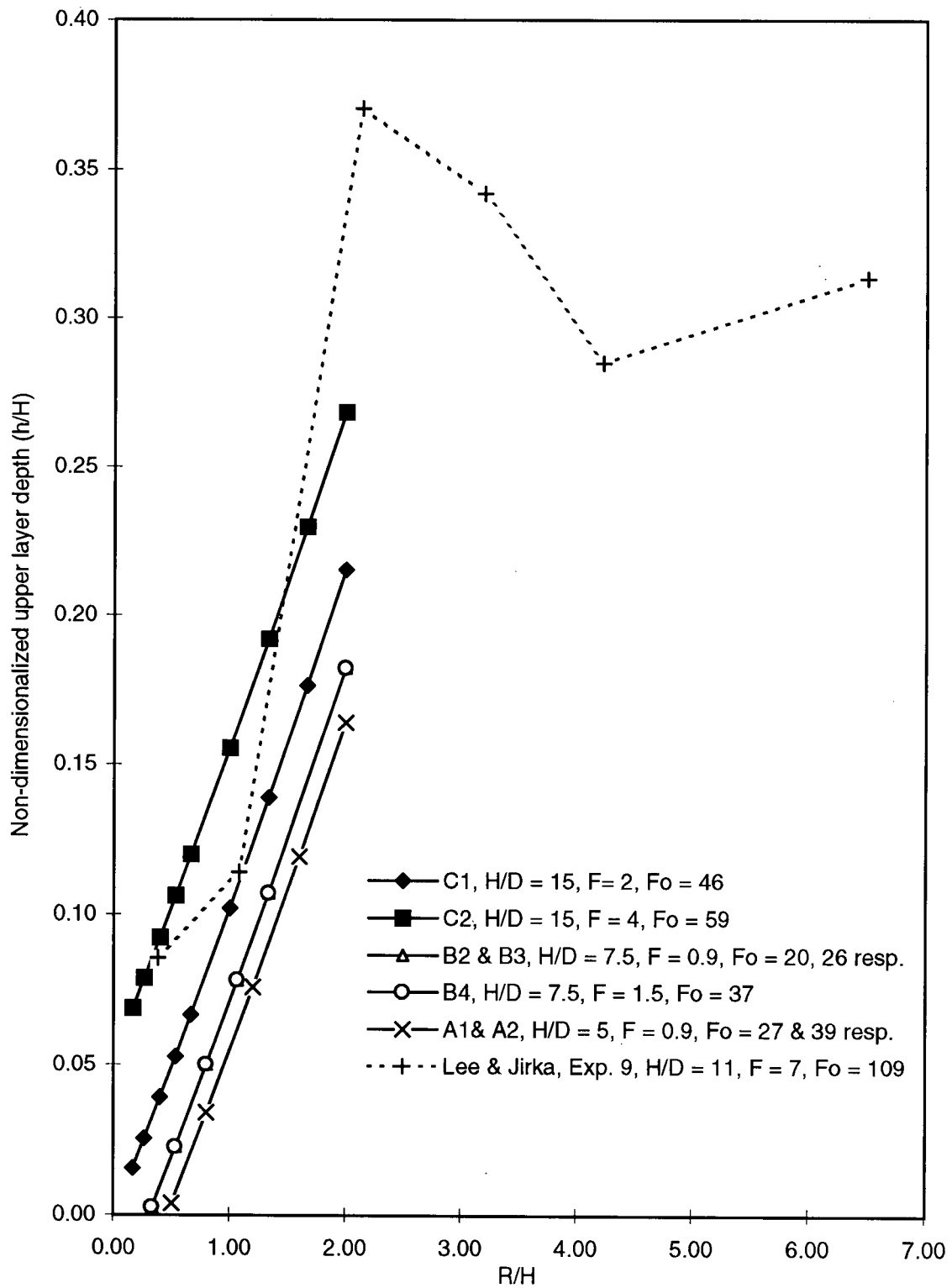


Figure 5.18: Plot of predicted non-dimensionalized upper layer depth ( $h/H$ ) as a function  $R/H$ .

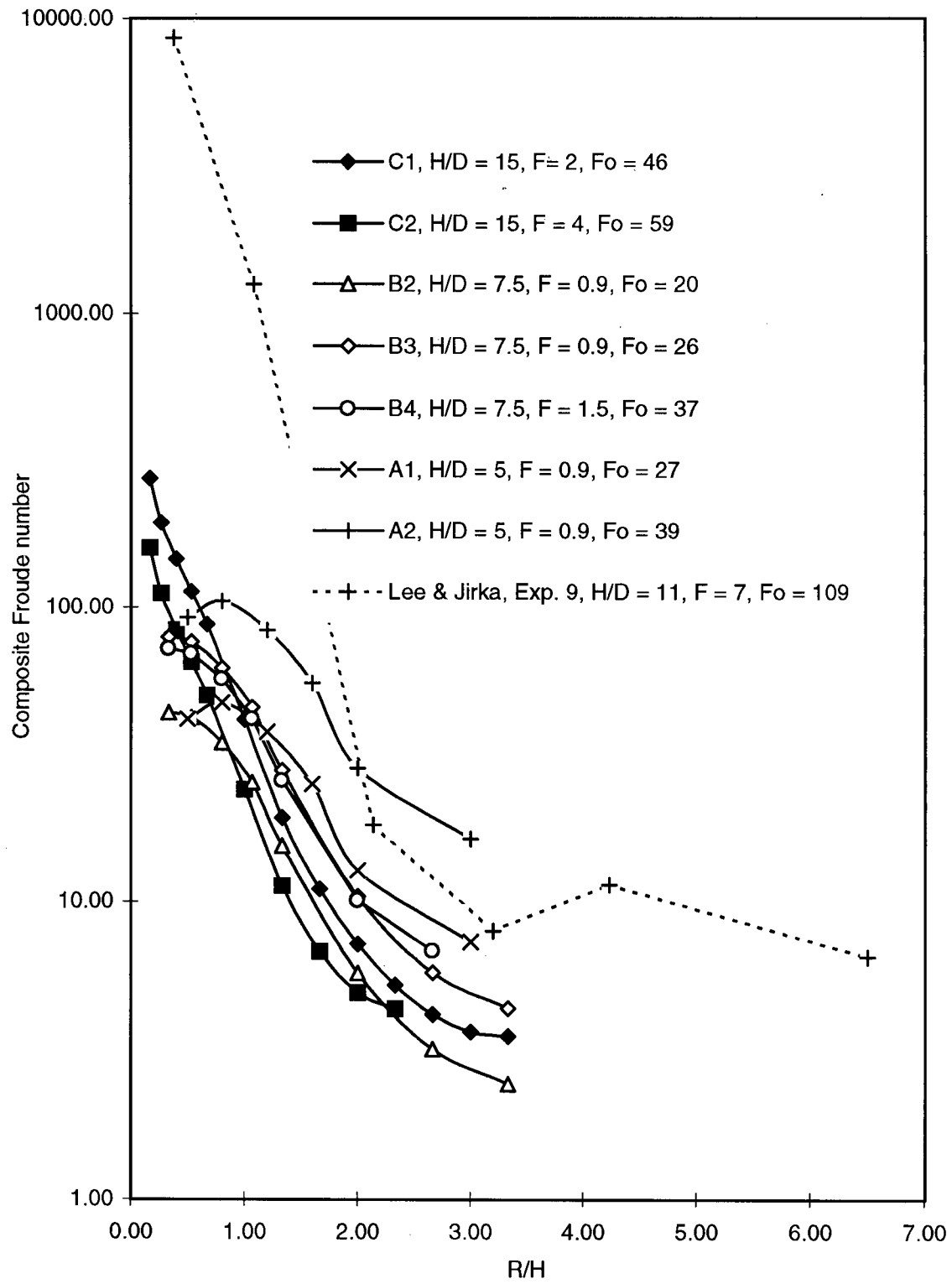


Figure 5.19: Plot of predicted Composite Froude number as a function of  $R/H$ .

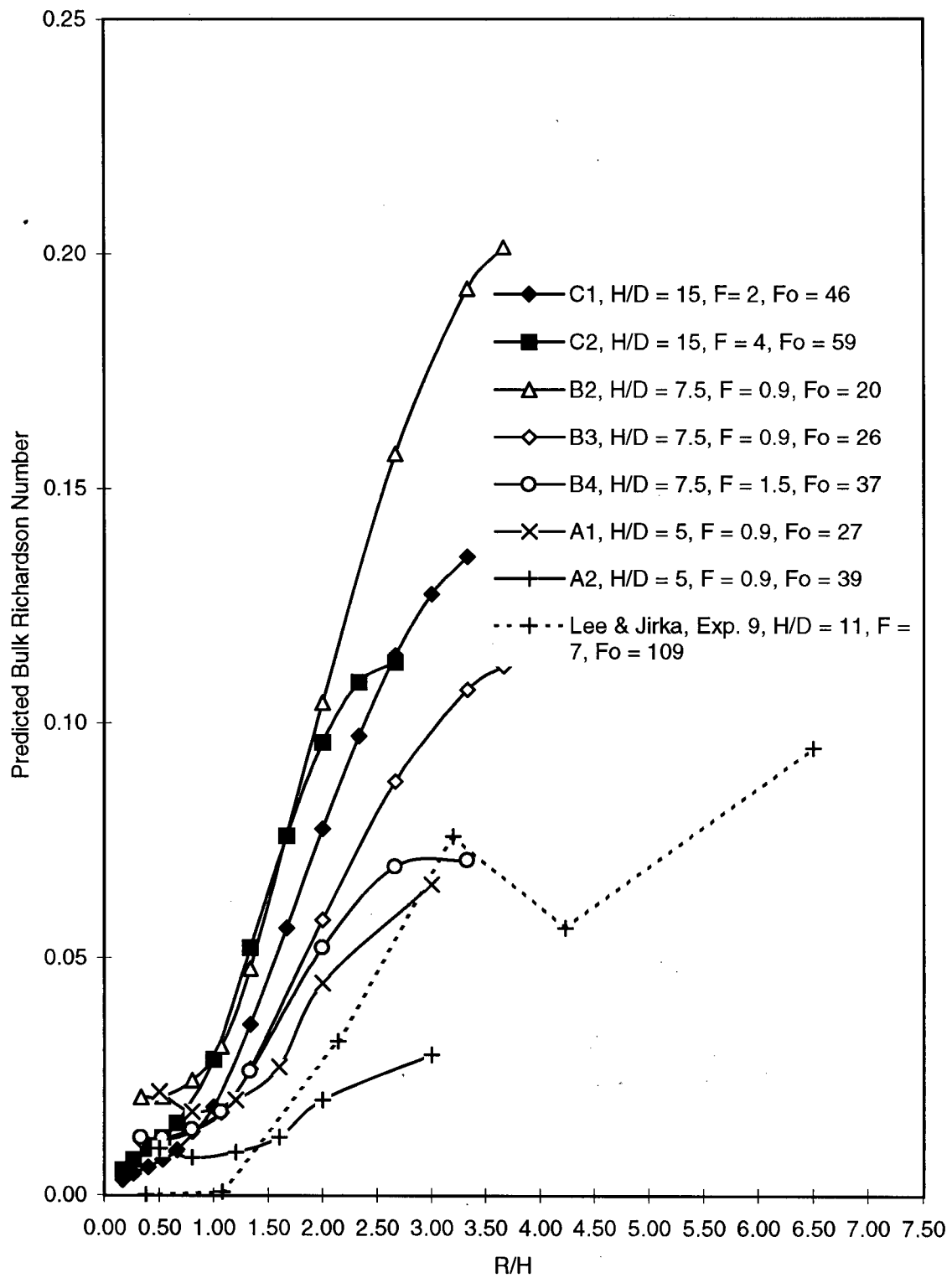


Figure 5.20: Plot of predicted bulk Richardson number as a function of  $R/H$ .

## Chapter 6

### Conclusions and Recommendations

#### **6.1 Conclusions**

The conclusions of the present study can be summarized as follows:

1. There is significant entrainment occurring into the radial jet emanating from the surface impingement region. Also, it appears that the entrainment into the radially spreading flow with distance is greater than that into the vertical jet region., this is evident in the results presented in figures 5.1 and 5.3. Equations 5.5 and 5.6 represent the best fit functions to the mean (bulk) and minimum dilutions respectively
2. The dilution of the radially spreading flow is essentially a linear function of radius and the entrainment rate was effectively constant for a given set of conditions.
3. The dilution results of the present study are consistent with the entrainment hypothesis of Morton, Taylor and Turner (1956). The entrainment velocity into the radial flow was proportional to the velocity difference between the upper and lower layers.
4. The depth of the radially spreading upper layer was found to be a second order polynomial function of the effective radius (equation 5.9) over the range of radii investigated in the present study.
5. The growth of the upper layer was consistent with the theory for the growth of mixing layers as reviewed by Ho & Heurre (1984), where the growth rate of a mixing layer is proportional to the velocity ratio between the two layers.
6. No internal hydraulic jumps were present anywhere in the radially spreading flow, over the extent investigated. The composite Froude number was always greater than 1 (i.e. the flow was internally supercritical) over the extent of radial flow investigated.
7. When the internal hydraulic jump component is removed from Lee & Jirka's (1981) model the dilution predictions are consistent with the results of the present study.

8. The Bulk Richardson number values begin well below the recognized critical value of 0.3 and increase with radius. Within the extent of flow investigated in this study the bulk Richardson number never increases above 0.3. Because the maximum radii to which measurements were made did not include the region where entrainment and upper layer growth subsides it is not possible to comment on whether entrainment subsides at or near the recognized critical value, or where in fact that would occur.

In previously reported studies of radially spreading surface flows, velocity measurements have not been included. As a result it has not been possible to determine the composite and stability Froude numbers, bulk Richardson numbers, or the tracer flux based dilutions. The present study expands the knowledge of radially spreading flows by determining these quantities and demonstrating that there is not an internal hydraulic jump in the radially spreading flow and that entrainment and dilution of the radially spreading surface flow is continuous and significant. The basic relationships developed as part of the present study should improve the understanding of radially spreading surface flows caused by vertical jets in shallow water, and the accuracy with which these flows can be predicted and modeled.

The results of the present study should be taken into account in the design of outfall diffusers in which the jet or plume originates as a single vertical source, or can be approximated as one, and is expected to surface. The results provide a clear indication that entrainment into the radially spreading flow is significant and occurs at a greater rate than into the vertical jet. The relative importance of any dilution of the radially spreading flow will depend on the extent of the vertical jet and the dilution which occurs there.

## **6.2 Recommendations**

Further studies are recommended to expand the range of conditions investigated and broaden the applicability of the predictive relationships developed in the present study. The results of studies over a wider range of jet parameters, such as the depth to

diameter ratio and densimetric Froude number, could then be incorporated into a predictive model over a wider range of governing conditions.

Any future studies should also investigate a greater extent of the radial flow, to an  $R/H$  perhaps as large as 6. This would place the region where flow conditions appear to change ( $R/H$  of 3 to 4) well within the extent of the experimental apparatus. The region in which entrainment and upper layer growth subsides could then be investigated, and predictive relationships for the cessation of large scale entrainment developed. However, this would probably not be successfully achieved by scaling down the depth of the tank, the overall scale of the flows investigated in the present study should be regarded as a minimum if an ADV were to continue to be used in such a study. This is a concession to the size of the sampling volume of such instruments, and its apparent problems with moving surfaces, smaller scale flows would likely compound the problem and further decrease the accuracy of the instrument. It is possible that other instrumentation may be used in place of the ADV, but it is not clear at the time what would be an appropriate replacement.

If absolutely necessary it may be possible to assume that the velocity profiles are the same shape as the temperature profiles and determine velocities iteratively from temperature data. However, such an approach would likely be less satisfactory than actual velocity measurements.

## Notation

$B = U_o g' \pi D^2 / 4$  : initial buoyancy flux of jet (equation 2.6)

$b_t = 0.127z$  : characteristic width of tracer profile (equation 2.14)

$b_u = 0.107z$  : characteristic width of velocity profile (equation 2.13)

$C = C_m \exp[-(x/b_t)^2]$  : tracer concentration away from jet center line (equation 2.16)

$C_o$  : initial tracer concentration

$C_m = 5.64C_o(l_Q/z)$  : tracer concentration on jet centerline (equation 2.15)

$c_p = 0.254$  : plume coefficient

$D$  : diameter of jet nozzle

$D_k = k/k_o$  : kinetic energy flux discrepancy

$D_T = T_f/T_{f_o}$  : temperature flux discrepancy

$D_Q \propto \sqrt{D_k}$  : volume flux discrepancy

$F_o = U_o / (g'_o D)^{1/2}$  : jet densimetric Froude number (equation 2.8)

$F = U_o / (gD)^{1/2}$  : jet Froude number (equation 2.7)

$F_U = U_U / \sqrt{g'h}$  : upper layer densimetric Froude number

$F_L = U_L / \sqrt{g'(H-h)}$  : lower layer densimetric Froude number

$F_\Delta^2 = \frac{\Delta U^2}{g'H}$  : stability Froude number (equation 3.6)

$F_I = \frac{U_U(H-h) + U_L h}{\sqrt{g'h(H-h)H(1-F_\Delta^2)}}$  : internal Froude number (3.7)

$F_E = \frac{\tilde{U}}{\sqrt{gH}}$  : external Froude number (equation 3.8)

$F_H = \frac{U_o}{\sqrt{gH}}$  : "depth" Froude number (equation 5.9)

$G^2 = \frac{U_U^2}{g'h} + \frac{U_L^2}{g'(H-h)}$  : composite Froude number squared (equation 3.5)

$g'_o = g \Delta \rho_o / \rho$  : initial effective gravitational acceleration

$g' = g \Delta \rho / \rho$  : effective gravitational acceleration

$H$  : total depth of ambient water

$h$  : depth of upper layer

$l_Q = Q / M^{1/2}$  : jet characteristic length scale (equation 2.10)

$l_M = M^{3/4}/B^{1/2}$ : characteristic length scale for buoyant jets (equation 2.19)

$M = U_o^2 \pi D^2/4$ : initial momentum flux of jet (equation 2.5)

$m = \int_A u^2 dA$ : specific momentum flux in jet (equation 2.2)

$N = \sqrt{(g/\rho)\partial\rho/\partial z}$ : Brunt Vaisälä (buoyancy) frequency

$Q_o = U \pi D^2/4$ : initial volume flux of jet (equation 2.4)

$Q_e$ : estimated entrained flow

$Q_R$ : ambient recharge flow rate

Re: jet Reynolds' number at exit from nozzle

$Ri_b = \frac{g'h}{\Delta U^2}$ : bulk Richardson number (equation 3.3)

$R_o = l_Q/l_M$ : initial jet Richardson number (equation 2.20)

$R_p = 0.557$ : plume Richardson number

$Ri_g = g \frac{\partial\rho}{\partial z} / \rho \left( \frac{\partial u}{\partial z} \right)^2$ : gradient Richardson number (equation 3.1)

$R$ : radius

$R' = R/D + 2.7$ : effective radius (equation 5.4)

$S$ : time averaged mean dilution

$S_{\min}$ : time averaged minimum (surface) dilution

$S_V = 0.254 \left( \frac{H}{D} \right) + \exp\left( -0.125 \frac{H}{D} \right)$ : dilution in vertical jet (equation 5.1)

$S_R = S - S_V$ : bulk radial dilution

$S_{R\min} = S_{\min} - S_V$ : minimum radial dilution

$U_o$ : average velocity at jet exit

$T_j$ : temperature of jet fluid at nozzle exit

$T_A$ : temperature of ambient fluid

$T_{AVG}$ : average temperature of radial jet

$T_s$ : surface (maximum) temperature

$\Delta T(R, z)$ : temperature difference as a function of radius ( $R$ ) and depth ( $z$ )

$\Delta T_{\max}(R)$ : maximum or surface temperature difference as a function of radius ( $R$ )

$Tf$ : temperature flux in radial jet

$Tf_o$ : initial temperature flux of jet

$U(R, z)$ : Radial velocity as function of radius ( $R$ ) and depth ( $z$ ).

$U_U$ : time averaged mean upper layer velocity

$U_L$ : time averaged mean lower layer velocity

$U_{\max}$ : time averaged maximum or surface velocity of upper layer or radial flow.

$U_{\max}(R)$ : maximum or surface velocity as function of radius ( $R$ )

$\tilde{U} = (U_U h + U_L (H - h)) / H$ : flow weighted mean velocity.

$\bar{U} = (U_u + |U_L|)/2$ : convective velocity in mixing layer between layers of stratified flow.

$\Delta U = U_U - U_L$ : velocity difference between layers in a stratified flow.

$u = u_c \exp[-(x/b)^2]$ : time averaged jet velocity (equation 2.9)

$u_c = 7.0 l_Q M / z G$ : time averaged velocity at jet center line (equation 2.11)

$u_c = 4.7 \frac{B^{1/3}}{z^{1/3}}$ : centerline velocity pure plumes (equation 2.17)

$\frac{\partial u}{\partial z}$  or  $\frac{\partial U}{\partial z}$ : horizontal or radial velocity gradient in the vertical direction.

$x$ : distance from jet centerline, vertical jets.

$z$ : distance along jet centerline (trajectory length) or depth from surface in velocity and temperature profiles of Chen (1980)

$z_t$ : length of Zone of Flow Establishment

$Z_t = z_t / D$ : non-dimensionalized length of Zone of Flow Establishment

$z_e$ : entrainment length

$Z_e = z_e / D$ : non-dimensionalized entrainment length

$\alpha$ : entrainment coefficient

$\beta = \int_A g' u dA$ : specific buoyancy flux in jet (equation 2.3)

$\mu = \int_A u dA$ : volume flux in jet (equation 2.1)

$\mu = 0.35 B^{1/3} z^{5/3}$ : volume flux in pure plume (equation 2.18)

$\mu = 0.254 \pi^{1/2} z$

$\frac{\mu}{Q_o} = 0.25 \frac{z}{l_Q}$ : bulk dilution in vertical jet (equation 2.12)

$\bar{\mu} = \zeta \zeta \ll 1$ : mean dilution in buoyant jet (equation 2.23)

$\bar{\mu} = \zeta^{5/3} \zeta \gg 1$ : mean dilution in buoyant jet (equation 2.24)

$\bar{\mu} = \frac{\mu}{Q_o} \left( \frac{R_o}{R_p} \right)$ : mean dilution in buoyant jet (equation 2.21)

$\nu$ : kinematic viscosity

$\Delta \rho_o$ : density difference between ambient and jet

$\frac{\partial \rho}{\partial z}$ : density gradient in the vertical direction

$\xi = \frac{az}{R}$ : dimensionless parameterization of depth (from Chen (1980))

$\zeta = c_p \left( \frac{z}{l_Q} \right) \left( \frac{R_o}{R_p} \right)$ : dimensionless expression for dilution in buoyant jet (equation 2.22)

## References

- Abraham, G., 1965, "Entrainment Principle and its Restriction to Solve Jet Problems", *Journal of Hydraulic Research*, Vol. 3, No. 2, pp. 1-23.
- Albertson, M.L., Dai, Y.B., Jensen, R.A., Hunter, R., 1950, "Diffusion of Submerged Jets", *Transactions of the American Society of Civil Engineers*, Vol. 115, pp. 639-664.
- Armi, L., 1986, "The hydraulics of two flowing layers of different densities", *Journal of Fluid Mechanics*, Vol. 163, part 27.
- Chen, J.C., 1980, "Studies on Gravitational Spreading Currents", W. H. Keck Laboratory Report No. KH-R-40, California Institute of Technology, Pasadena, California, 436 pp. .
- Christodoulou, G.C., 1986, "Interfacial Mixing in Stratified Flows", *Journal of Hydraulic Research*, Vol. 24, No. 2, pp. 77-91.
- Crow, S.C., Champagne, F.H., 1971, "Orderly Structure in Jet Turbulence", *Journal of Fluid Mechanics*, Vol. 48, pp. 547-591.
- Daugherty, R.L., Franzini, J.B., Finnemore, E.J., 1985, "Fluid Mechanics with Engineering Applications", 8th edition, McGraw-Hill, New York, 583 pp. .
- Fischer, H.B., List, E.J., Imberger, J., Koh, R.C.Y, Brooks, N.H., 1979, "Mixing in Inland and Coastal Waters", Academic Press, New York, 483 pp.
- Fisher, T.S.R., 1995, "Dilution of Axisymmetric Buoyant Jets and Surface Spreading Fields", Thesis submitted in partial fulfillment of the degree Master of Engineering, University of Canterbury, Christchurch, New Zealand, 138 pp.
- Hill, B.J., 1972, "Measurement of local entrainment rate in the initial region of axisymmetric turbulent air jets", *Journal of Fluid Mechanics*, Vol. 51, part 4, pp. 773-779.
- Ho, C-M, Heurre, P., 1984, "Perturbed Free Shear Flows", *Annual Review of Fluid Mechanics*, Annual Reviews Inc. pp. 365-424.
- Jirka, G.H., Harleman, D.R.F., 1979, "Stability and Mixing of a Vertical Plane Buoyant Jet in Confined Depth", *Journal of Fluid Mechanics*, Vol. 94, part 2, pp. 275-304.

- Koh, R.C.Y., 1971, "Two-dimensional surface warm jets", *Journal of the Hydraulics Division, ASCE*, Vol. **97**, HY6, pp. 819-836.
- Koop, C.G., Browand, F.K., 1979, "Instability and Turbulence in a Stratified Fluid with Shear", *Journal of Fluid Mechanics*, Vol. **93**, pp. 135-159.
- Lawrence, G.A., 1985. "The Hydraulics and Mixing of Two-Layer Flow Over an Obstacle", Thesis submitted in partial fulfillment of the degree Doctor of Philosophy, University of California, Berkeley, California. 130 pp.
- Lawrence, G.A., 1990, "Can mixing in exchange flows be predicted using internal hydraulics", *The Physical Oceanography of Sea Straits*, Kluwer Academic Publishers, Netherlands, pp. 519-536.
- Lawrence, G.A., 1990(2), "On the hydraulics of Boussinesq and non-Boussinesq two-layer flows", *Journal of Fluid Mechanics*, Vol. **215**, pp. 457-480.
- Lawrence, G.A., Browand, K.F., Redekopp, L.G., 1991, "The stability of a sheared density interface", *Physics of Fluids*, American Institute of Physics, A Vol.3 No. 10, pp. 2360-2370.
- Lee, J.H.W., Jirka, G.H., 1981, "Vertical round buoyant jet in shallow water", *Journal of The Hydraulics Division, ASCE*, Vol. **107**, pp. 1651-1675.
- List, E.J., Imberger, J., 1981, "Turbulent entrainment in buoyant jets and plumes", *Journal of the Hydraulics Division, ASCE*, Vol. **99**, pp 1651-1675.
- List, E.J. 1982. "Turbulent jets and plumes", *Annual Review of Fluid Mechanics*, Vol. **14**, pp. 189-212.
- MacLachy, M.R., 1993, "Radial Spreading of Vertical Buoyant Jets in Shallow Water", Thesis submitted in partial fulfillment of the degree Master of Applied Science, University of British Columbia, Vancouver, Canada, 78 pp.
- Morton, B.R., Taylor, G., Turner, J.S., 1956, "Turbulent gravitational convection from maintained and instantaneous sources", *Proceedings of the Royal Society of London*, Vol. **234(A)**, pp. 1-23.
- Turner, J.S., "*Buoyancy Effects in Fluids*", Cambridge University Press, 1973, 368 pp.
- Turner, J.S., 1986, "Turbulent entrainment: the development of the entrainment assumption and its application to geophysical flows", *Journal of Fluid Mechanics*, Vol. **173**, pp. 431-471.
- Tritton, D.J., "Physical Fluid Dynamics", Clarendon Press, 1991, 519 pp.

Tso, J., Kovaszny, L.S.G., Hussain, A.K.M.F., 1981, "Search for Large-Scale Coherent Structures in the Nearly Self-Preserving Region of Turbulent Axisymmetric Jet", *Journal of Fluids Engineering*, V **103**, p.p. 503-8.

Van Dyke, M., "*An Album of Fluid Motion*", Parabolic Press, 1982, 176 pp.

White, F.M., "*Viscous Fluid Flow*", McGraw Hill Inc, 1991, 613 pp.

Wilkinson, D.L., Wood, I. R., 1971, "A rapidly varied flow phenomena in a two layer flow", *Journal of Fluid Mechanics*, Vol. **47**, part 2, pp. 241-256.

Wilton, M.J., Lawrence, G.A., 1998, "The evolution of the island copper mine pit lake", submitted to the proceedings of the Canadian Water Resources Association conference, May 1998, Victoria, B.C., 10 pp.

Wright, S.J., 1985, "Discussion to Wastewater Field Thickness and Initial Dilution", *Journal of Hydraulic Engineering, ASCE*, Vol. **111**, pp. 891-896.

Wright, S.J., Bühler, J., 1986, "Control of Buoyant Jet Mixing by Far Field Spreading", Proceedings of Symposium of Advancements on Aerodynamics, Fluid Mechanics, and Hydraulics, Minneapolis, Minnesota, pp.736-743.

Wright, S.J., Roberts, P.J.W., Zhongmin, Y., Bradley, N.E., 1991, "Surface dilution of round submerged buoyant jets", *Journal of Hydraulic Research*, Vol. **29**, No. 1, pp. 67-89.

## Appendix A

### Extension of Froude Numbers to Radial Flows

By examination of the equations of motion, it is possible to demonstrate that the Froude numbers used to determine flow criticality in radial flows are of the same form as the planar flow Froude numbers. When viscosity is constant, or can be neglected, the equations of motion for a two layer planar flow are (Lawrence, 1990(2)):

$$\frac{\partial \underline{V}}{\partial t} + \underline{C} \frac{\partial \underline{V}}{\partial x} = \underline{D} \frac{\partial \underline{F}}{\partial x} \quad (\text{A.1})$$

The matrices  $\underline{V}$ ,  $\underline{C}$ ,  $\underline{D}$ ,  $\underline{F}$  are defined as:

$$\underline{V} = \begin{bmatrix} U_1 \\ U_2 \\ h_1 \\ h_2 \end{bmatrix}, \underline{C} = \begin{bmatrix} U_1 & 0 & g & g \\ 0 & U_2 & (\rho_1/\rho_2)g & g \\ h_1 & 0 & U_1 & 0 \\ 0 & h_2 & 0 & U_2 \end{bmatrix}, \underline{D} = \begin{bmatrix} -g & 0 \\ -g & 0 \\ 0 & Q_1 \\ 0 & Q_2 \end{bmatrix}, \underline{F} = \begin{bmatrix} h_s \\ b^{-1} \end{bmatrix}$$

In the vector  $\underline{F}$ ,  $h_s$  is the height of a sill, if present in the channel, and  $b$  is the width of the channel. When the matrices are expanded in equation A.1 the first two resulting equations are for momentum (Navier-Stokes) in each of the two layers, and the last two are continuity equations.

The characteristic velocities of internal long waves acting along the interface between the two layers depend upon the matrix  $\underline{C}$  and satisfy the following condition (Lawrence, 1990(2)):

$$\text{Det}(\underline{C} - \lambda I) = 0 \quad (\text{A.2})$$

If radial symmetry is assumed for a radial flow, and the vertical velocities are minor compared to the radial (neglecting entrainment), then the equations of motion for both the tangential ( $\theta$ ) and  $z$  components can be neglected. The equation of motion for the radial ( $R$ ) component is:

$$\begin{aligned} & \frac{\partial U_R}{\partial t} + U_R \frac{\partial U_R}{\partial R} + \frac{U_\theta}{R} \frac{\partial U_R}{\partial \theta} + U_z \frac{\partial U_R}{\partial Z} - \frac{V_\theta^2}{R} \\ & = \frac{-1}{\rho} \frac{\partial P}{\partial R} + \frac{1}{3} v \frac{\partial \Theta}{\partial R} + v \left[ \frac{1}{R} \frac{\partial}{\partial R} \left( r \frac{\partial U_R}{\partial R} \right) + \frac{1}{R^2} \frac{\partial^2 U_\theta}{\partial \theta^2} + \frac{\partial^2 U_R}{\partial z^2} - \frac{U_R}{R^2} - \frac{2}{R^2} \frac{\partial U_\theta}{\partial \theta} \right] + f_R \end{aligned} \quad (\text{A.3})$$

Assuming that density variations are minor, that viscosity is constant, and taking into account the previously stated assumptions of radial symmetry and small vertical velocities and radial velocity gradients in the vertical direction, equation A.3 simplifies to:

$$\frac{\partial U_R}{\partial t} + U_R \frac{\partial U_R}{\partial R} = \frac{-1}{\rho} \frac{\partial P}{\partial R} \quad (\text{A.4})$$

For two layer flows, the pressure ( $P$ ) is often replaced by the piezometric pressure ( $P^*$ ) which for the top and bottom layers, respectively, is:

$$P_1^* = \rho_1 g(z + h_1 + h_2)$$

$$P_2^* = \rho_2 g(z + h_2) + \rho_1 g h_1$$

The momentum equation for each of the two radially spreading layers from equation A.4 then becomes, after dropping the  $R$  subscript:

$$\frac{\partial U_1}{\partial t} + U_1 \frac{\partial U_1}{\partial R} = \frac{-1}{\rho_1} \frac{\partial}{\partial R} (\rho_1 g(z + h_1 + h_2))$$

$$\frac{\partial U_2}{\partial t} + U_2 \frac{\partial U_2}{\partial R} = \frac{-1}{\rho_2} \frac{\partial}{\partial R} (\rho_2 g(z + h_2) + \rho_1 g h_1)$$

After reorganizing the two equations are:

$$\frac{\partial U_1}{\partial t} + U_1 \frac{\partial U_1}{\partial R} + g \frac{\partial h_1}{\partial R} + g \frac{\partial h_2}{\partial R} = -g \frac{\partial z}{\partial R} \quad (\text{A.5})$$

$$\frac{\partial U_2}{\partial t} + U_2 \frac{\partial U_2}{\partial R} + g \frac{\rho_1}{\rho_2} \frac{\partial h_1}{\partial R} + g \frac{\partial h_2}{\partial R} = -\frac{\partial z}{\partial R} \quad (\text{A.6})$$

These two equations are the momentum equations governing the upper and lower layers respectively. The continuity equations for the two layers can be expressed as (neglecting entrainment):

$$\frac{\partial Q_1}{\partial R} = 0, \quad \frac{\partial Q_2}{\partial R} = 0$$

Recognizing that  $Q = 2\pi R U h$ :

$$\frac{\partial Q_1}{\partial R} = 2\pi R h \frac{\partial U_1}{\partial R} + 2\pi R U_1 \frac{\partial h_1}{\partial R} + 2\pi h_1 U_1 \frac{\partial R}{\partial R} = 0 \quad (\text{A.7})$$

$$2\pi h_1 \frac{\partial U_1}{\partial R} + 2\pi U_1 \frac{\partial h_1}{\partial R} = -\frac{2\pi h_1 U_1}{R} \frac{\partial R}{\partial R} \quad (\text{A.8})$$

The right hand side of equation (A.8) can be manipulated so that:

$$-\frac{2\pi h_1 U_1}{R} \frac{\partial R}{\partial R} = -\frac{2\pi R U h}{R^2} \frac{\partial R}{\partial R} = Q \frac{\partial}{\partial R} \left( \frac{1}{R} \right)$$

Equation A.8 then becomes:

$$h_1 \frac{\partial U_1}{\partial R} + U_1 \frac{\partial h_1}{\partial R} = \frac{Q}{2\pi} \frac{\partial}{\partial R} \left( \frac{1}{R} \right) = Q \frac{\partial}{\partial R} \left( \frac{1}{2\pi R} \right) \quad (\text{A.9})$$

The complete equation for continuity, including the time derivative, for the upper layer is then:

$$\frac{\partial h_1}{\partial t} + h_1 \frac{\partial U_1}{\partial R} + U_1 \frac{\partial h_1}{\partial R} = Q \frac{\partial}{\partial R} \left( \frac{1}{2\pi R} \right) \quad (\text{A.10})$$

The continuity equation for the lower layer is in all respects identical to equation 3.19 in its derivation and result. When the resulting equations of motion for the radial flow configuration are expressed in the same form as equation A.1:

$$\frac{\partial V}{\partial t} + \underline{C} \frac{\partial V}{\partial R} = \underline{D} \frac{\partial F}{\partial R} \quad (\text{A.11})$$

Then:

$$\underline{C} = \begin{bmatrix} U_1 & 0 & g & g \\ 0 & U_2 & (\rho_1/\rho_2)g & g \\ h_1 & 0 & U_1 & 0 \\ 0 & h_2 & 0 & U_2 \end{bmatrix}$$

The matrix  $\underline{C}$  is identical to that for two layer planar flows, and as a result the internal long wave speeds are defined identically. Hence the definitions of the various Froude numbers, as used for a two layer planar flow, are also used for a two layer radial flow.

## Appendix B

### Theoretical Development of Upper Layer Growth Model

This appendix investigates the rate at which the thickness of a radially spreading surface jet grows. This problem has been investigated by Chen (1980) for the case where the receiving fluid is infinitely deep and, consequently the return flow in the ambient is negligible. For steady flow the continuity and momentum equations become:

$$\frac{1}{R} \frac{\partial}{\partial R} (RU) + \frac{\partial W}{\partial z} = 0 \quad (\text{B.1})$$

$$U \frac{\partial U}{\partial R} + W \frac{\partial U}{\partial z} = \frac{\partial}{\partial z} \left( \frac{\tau_{zR}}{\rho} \right) \quad (\text{B.2})$$

Where  $R$  is the horizontal (radial) direction,  $U$  is the velocity in the radial direction,  $W$  is the velocity in the vertical direction  $z$ , and  $\tau_{zR}$  is the turbulent shear stress. A summary of Chen's analysis will be presented below followed by an extension to allow for the effect of a return flow in the lower layer.

Chen (1980) assumed a similarity solution for the velocity profile of the form:

$$\frac{U(R, z)}{U_{\max}(R)} = F'(\xi) \quad (\text{B.3})$$

Where:

$$F(\xi) = \int_{\infty}^{\xi} F'(\xi) d\xi \quad (\text{B.4})$$

Where  $\xi = az/R$ , a dimensionless parameterization of the depth, and  $U_{\max}(R)$  is the maximum or surface velocity as a function of radius. The boundary conditions for the velocities are:

1. vertical velocity at the surface equals zero,  $W(R,0) = 0$ .

2. vertical gradient of mean radial velocity equals zero at the surface,  
 $\partial/\partial z(U(R,0))=0$
3. mean radial velocity is the maximum at the surface,  $U(R,0)=U_{\max}(R)$
4. At infinite depth both the vertical and radial mean velocities are zero,  
 $U(R,\infty)=W(R,\infty)=0$ .

The boundary conditions for the velocities become (for  $F'(\xi)$ ):

1.  $F'(0)=1$
2.  $F''(0)=0$
3.  $F(\infty)=F'(\infty)=0$ .

The maximum velocity is proportional to the square root of the initial jet momentum flux and inversely proportional to the radius (by conservation of radial momentum, see Chen (1980)):

$$U_{\max}(R) \propto \frac{\sqrt{M}}{R} \quad (\text{B.5})$$

Chen (1980) used a Stokes' stream function, i.e.:

$$U(R,z) = \frac{1}{R} \frac{\partial \psi}{\partial z} \quad (\text{B.6})$$

$$W(R,z) = -\frac{1}{R} \frac{\partial \psi}{\partial R} \quad (\text{B.7})$$

With the result that the stream function  $\psi$  is:

$$\psi(R,z) = \frac{U_{\max}(R)R^2}{a} F(\xi) \quad (\text{B.8})$$

From equations B.7 and B.8 (primes denote differentiation with respect to  $\xi$ ):

$$W(R,z) = \frac{U_{\max}}{a} \{\xi F'(\xi) - F(\xi)\} \quad (\text{B.9})$$

The vertical gradient of the mean radial velocity is, from equations B.6 and B.8:

$$\frac{\partial}{\partial z}(U(R, z)) = \frac{aU_{\max}(R)}{R} F''(\xi) \quad (\text{B.10})$$

The turbulent shear stress in the radial momentum equation (B.2) can be treated as equivalent to an eddy viscosity ( $\epsilon_U$ ) multiplied by the vertical gradient of the mean velocity ( $\partial U/\partial z$ ):

$$\frac{\tau_{zR}}{\rho} = -\overline{U'W'} = \epsilon_U \frac{\partial U}{\partial Z}$$

Prandtl-Tollmien's assumption for the eddy viscosity is:

$$\epsilon_U = l_u^2 \left| \frac{\partial U}{\partial z} \right|$$

Where  $l_u$  is Prandtl's mixing length for momentum transfer and can be expressed as:

$$l_u = c_U R$$

Where  $c_U$  is a coefficient for the growth of the mixing length with radial distance. If  $K_U = c_U^2$  then the full Prandtl-Tollmien assumption for eddy viscosity is:

$$\epsilon_U = K_U R^2 \left| \frac{\partial U}{\partial z} \right|$$

And the expression for turbulent shear stress is expressed as:

$$\frac{\tau_{zR}}{\rho} = K_U R^2 \left| \frac{\partial U}{\partial Z} \right| \frac{\partial U}{\partial Z} \quad (\text{B.11})$$

Integrating the radial momentum equation in the vertical direction from  $\infty$  to  $z$  and substituting in equation B.11, gives this form of the radial momentum equation:

$$UW + \frac{1}{R} \frac{\partial}{\partial R} \left( \int_{\infty}^z RU^2 dz \right) - K_U R^2 \left| \frac{\partial U}{\partial z} \right| \frac{\partial U}{\partial z} = 0 \quad (\text{B.12})$$

Substituting in equations B.3 and B.9 gives the ordinary differential equation:

$$(F''(\xi))^2 - F(\xi)F'(\xi) = 0 \quad (\text{B.13})$$

And defines:

$$a = \sqrt[3]{\frac{1}{K_U}}$$

Thus, the self-similar solution assumed by Chen (1980) satisfies the equations of motion and the boundary conditions specified. The coefficient  $a$  is a constant assuming that  $K_U$  remains constant. Therefore the upper layer growth rate is a constant, i.e. linear growth of the characteristic depth of the velocity profile. The surface or maximum velocity varies inversely with radius.

The infinite ambient depth, with no return flow ( $U_L = 0$ ), as assumed by Chen (1980), makes this result compatible with measurements from a variety of mixing layers, see Ho & Heurre (1984), where the growth of the mixing layer is given by:

$$\frac{dh}{dx} = c \frac{\Delta U}{2\bar{U}} \quad (3.12)$$

Where  $\Delta U$  is the velocity difference between the two layers and  $\bar{U}$  is the average velocity between the two layers and represents the mean convective speed in the mixing layer. In mixing layers the constant  $c$  is often on the order of 0.14 (Lawrence et al., 1991).

The absence of a return flow in the infinite ambient case causes the mixing layer, which the upper layer is in effect, to grow at a constant rate, i.e. linearly:

$$\frac{dh}{dR} = c \frac{U_U - U_L}{U_U + U_L} = c \frac{U_U - 0}{U_U + 0} = c$$

This is consistent with Chen's theoretical result and therefore it appears valid to apply the mixing layer growth model to a radially spreading flow. A situation involving a finite ambient water depth, would probably result in the mixing layer growth assuming a non-linear form due to the non-zero return flow in the lower layer. The relationship for the growth of the radially spreading upper layer is hypothesized to be:

$$\frac{dh}{dR} = c \frac{\Delta U}{2\bar{U}} \quad (\text{B.14})$$

For the radial flow configuration the velocity difference is defined as:

$$\Delta U = U_{\max} + |U_L| \quad (\text{B.15})$$

The upper layer velocity at the surface ( $U_{\max}$ ) is used to provide the full velocity difference over the depth of the upper layer flow, which is in effect a mixing layer. The average or convective velocity is simply:

$$\bar{U} = (U_{\max} - |U_L|)/2 \quad (\text{B.16})$$

As the velocity profiles in the upper layer are roughly linear, except very near the surface or at small radii, the upper layer surface velocity ( $U_{\max}$ ) can be approximated as twice the average velocity in the upper layer ( $U_u$ ). Both the upper and lower layer velocities can be expressed in terms of the bulk dilution, upper layer depth and radius:

$$U_{\max} = 2U_u = \frac{2SQ_o}{2\pi Rh} = \frac{SQ_o}{\pi Rh} \quad (\text{B.17})$$

$$|U_L| = \frac{(S-1)Q_o}{2\pi R(H-h)} \quad (\text{B.18})$$

Substituting both these formulae into equation B.14 the following is obtained:

$$\frac{dh}{dR} = c \frac{U_{\max} + |U_L|}{U_{\max} - |U_L|} = c \frac{\frac{2S}{h} + \frac{S-1}{(H-h)}}{\frac{2S}{h} - \frac{S-1}{(H-h)}} \quad (\text{B.19})$$

Equation B.19 can be simplified to:

$$\frac{dh}{dR} = c \frac{1 - (S+1)h/2SH}{1 - (3S-1)h/2SH} \quad (\text{B.20})$$

Setting the following quantities:

$$a = (S+1)/2S, \quad b = (3S-1)/2S$$

and non-dimensionalizing by  $H$ :

$$h^* = h/H, \quad R^* = R/H$$

Equation B.20 can be stated as:

$$\frac{dh^*}{dR^*} = c \frac{1 - ah^*}{1 - bh^*} \quad (\text{B.21})$$

Rearranging equation B.21 and integrating both sides:

$$\int_{h_o}^h \frac{(1-bh)}{(1-ah)} dh = \int_{R_o}^R c dR \quad (\text{B.22})$$

Integration of the right hand side of equation B.22 is simply:

$$\int_{R_o}^R c dR = c(R - R_o) = \hat{R} \quad (\text{B.22})$$

Working with the left hand side of equation B.22:

$$\begin{aligned} & \int_{h_o}^h \frac{(1-bh)}{(1-ah)} dh \\ &= \int \frac{dh}{1-ah} - b \int \frac{h}{1-ah} \end{aligned}$$

Integrating and simplifying:

$$\begin{aligned} &= -\frac{1}{a} \ln(1-ah) + \frac{bh}{a} + \frac{b}{a^2} \ln(1-ah) \\ &= \frac{b-a}{a^2} \ln(1-ah) + \frac{bh}{a} \end{aligned}$$

Performing a Taylor series expansion on the natural log term:

$$\begin{aligned} &= \frac{b-a}{a^2} \left[ -ah - \frac{a^2 h^2}{2} - \frac{a^3 h^3}{3} - \dots \right] + \frac{bh}{a} \Big|_{h_0}^h \\ &= -\frac{bh}{a} + h - \frac{b-a}{a^2} \left[ \frac{a^2 h^2}{2} + \frac{a^3 h^3}{3} + \dots \right] + \frac{bh}{a} \Big|_{h_0}^h \end{aligned}$$

The following power series is obtained:

$$= h - \frac{b-a}{2} h^2 - \frac{(b-a)a}{3} h^3 - \frac{(b-a)a^3}{4} h^4 + \dots \Big|_{h_0}^h = c(R - R_0) = \hat{R}$$

Using reversion of power series:

$$h - h_0 = \hat{R} + \frac{b-a}{2} \hat{R}^2 + \left( \frac{(b-a)^2}{2} + \frac{(b-a)a}{3} \right) \hat{R}^3 + \dots \quad (\text{B.24})$$

Substituting in  $a = (S+1)/2S$ ,  $b = (3S-1)/2S$ ,  $b-a = (S-1)/S$ , equation B.24 becomes:

$$h - h_0 = \hat{R} + \frac{(1-1/S)}{2} \hat{R}^2 + \left( \frac{(S-1)^2}{2S^2} + \frac{(S-1)(S+1)}{6S^2} \right) \hat{R}^3 + \dots$$

$$h - h_0 = \hat{R} + \frac{(1-1/S)}{2} \hat{R}^2 + \left( \frac{3S^2 - 6S + 3}{6S^2} + \frac{S^2 - 1}{6S^2} \right) \hat{R}^3 + \dots$$

$$h - h_0 = \hat{R} + \frac{1}{2} \hat{R}^2 + \frac{1}{2S} \hat{R}^2 + \left( \frac{4S^2 - 6S + 2}{6S^2} \right) \hat{R}^3 + \dots$$

$$h - h_0 = \hat{R} + \frac{1}{2} \hat{R}^2 + \frac{1}{2S} \hat{R}^2 + \left( \frac{2}{3} - \frac{1}{S} + \frac{2}{6S^2} \right) \hat{R}^3 + \dots$$

The coefficient for the  $\hat{R}^3$  term is always less than or equal to  $2/3$  as:

$$-\frac{1}{S} + \frac{2}{6S^2} \begin{cases} = -\frac{2}{3}, S = 1 \\ \rightarrow 0, S \rightarrow \infty \end{cases}$$

and if  $\hat{R} < 1$  then:

$$h - h_o = \hat{R} + \frac{1}{2}\hat{R}^2 + \left[ < \frac{2}{3}\hat{R} + \frac{1}{2S} \right] \hat{R}^2 + \dots \quad (\text{B.25})$$

Then the third term is small and all terms with  $\hat{R}$  to powers greater than 2 can be neglected and equation B.25 simplifies to:

$$h - h_o = \hat{R} + \frac{1}{2}\hat{R}^2 \quad (\text{B.26})$$

As an example consider series A experiments where the largest radius at which measurements were made was 60cm, and  $R_o = 2.7D = 16.2\text{cm}$ , and  $H = 30$ . Assuming that  $c = 0.14$ , then:

$$\hat{R} = c \frac{R - R_o}{H} \text{ and then } \hat{R} = 0.204, \hat{R}^2 = 0.0418, \hat{R}^3 = 0.00854$$

So provided that  $\hat{R} < 1$ , which is the case for the range of radii investigated in the present study, then terms of higher order than 2 can easily be neglected. Returning equation B.26 to dimensional form achieves the general form of the relationship for the upper layer depth as a function of radius:

$$\frac{h - h_o}{H} = c \frac{(R - R_o)}{H} + \frac{1}{2} \left( c \frac{(R - R_o)}{H} \right)^2 \quad (\text{B.27})$$

Provided that  $c(R - R_o)/H < 1$ .

## Appendix C

### Plots of Velocity Profiles for Individual Experiments

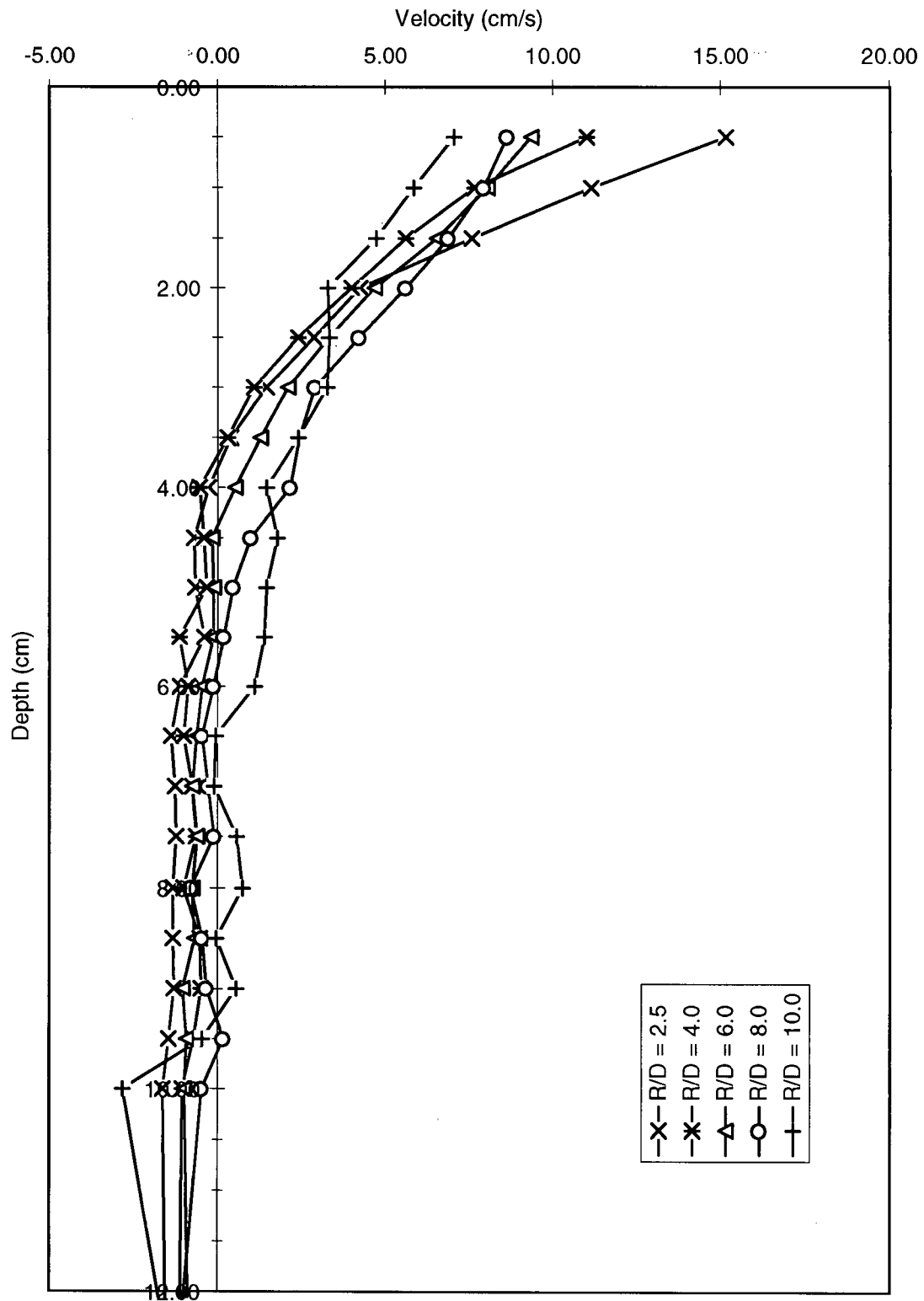


Figure C.1: Time averaged radial velocity profiles for experiment A1 (average of all replicates).

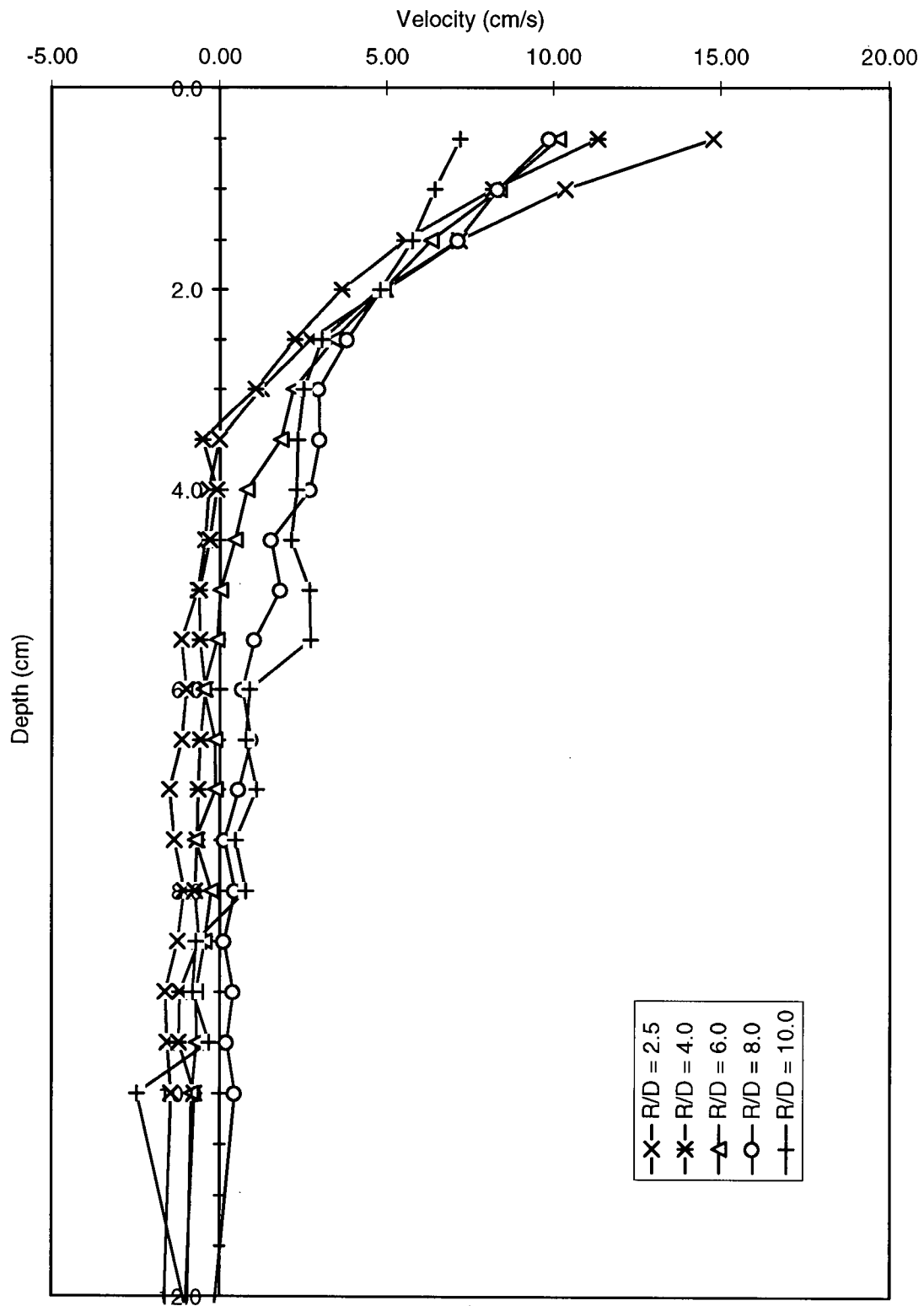


Figure C.2: Time averaged radial velocity profiles for experiment A2 (average of all replicates).

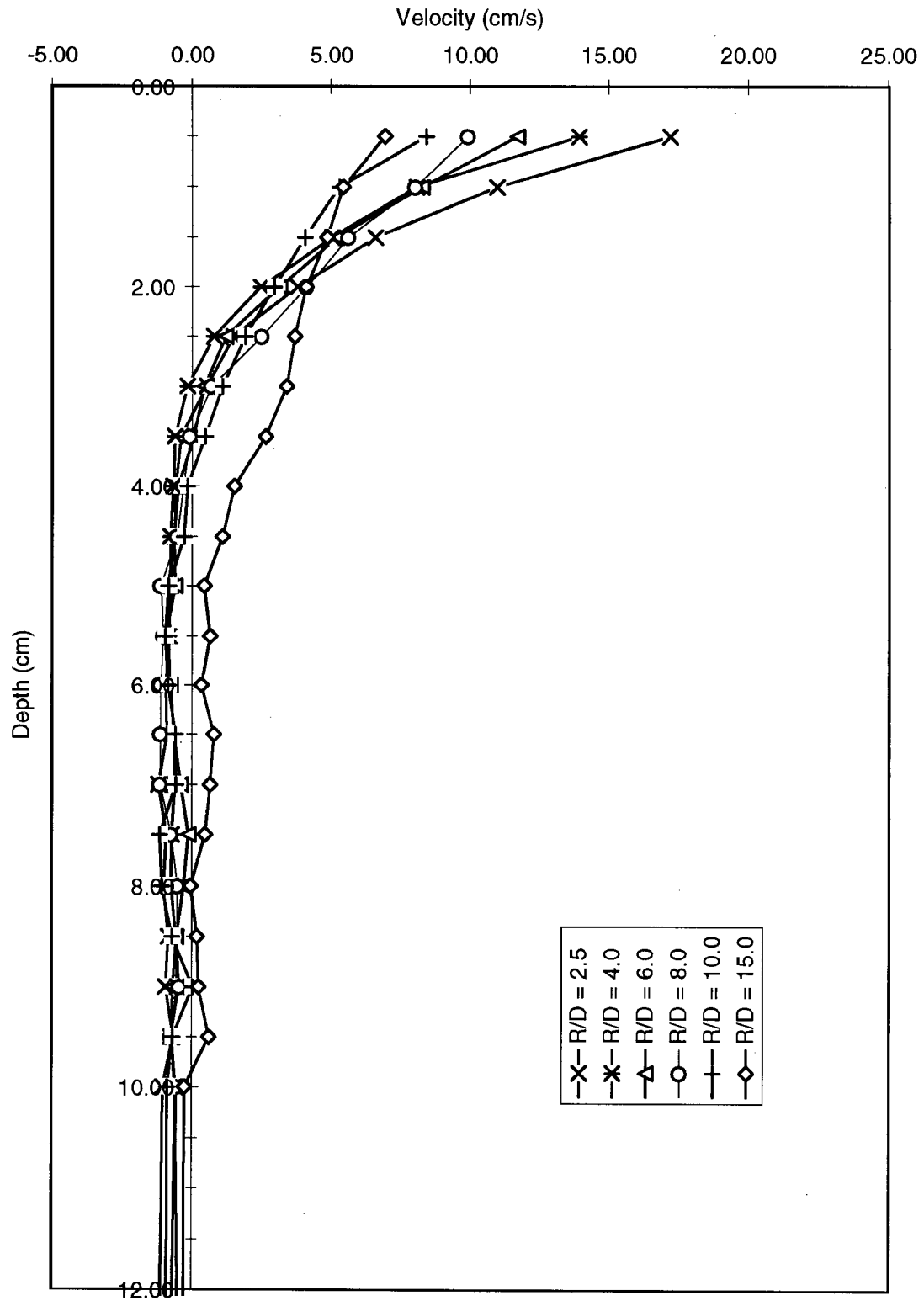


Figure C.3: Time averaged radial velocity profiles for experiment B2 (average of all replicates).

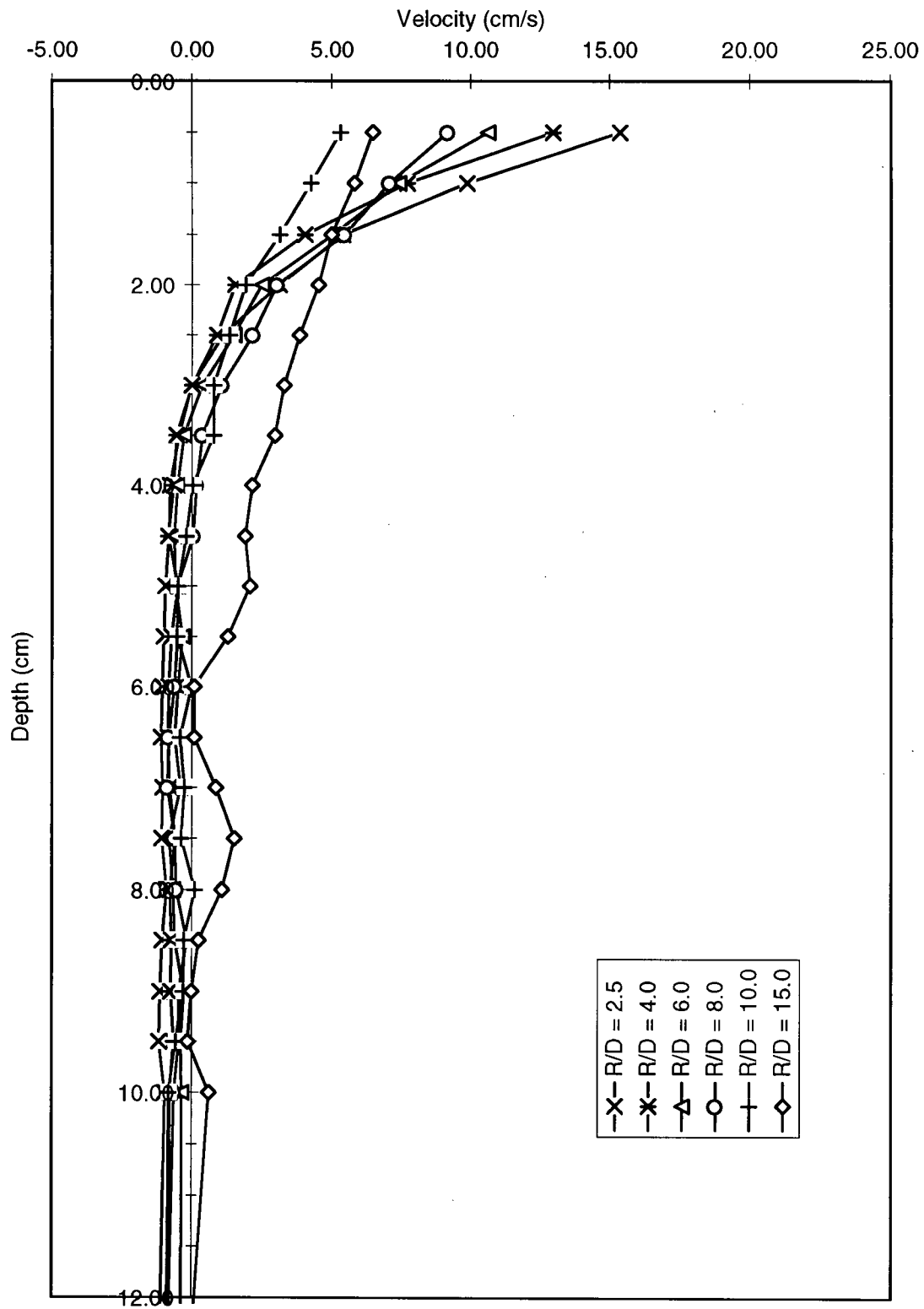


Figure C.4: Time averaged radial velocity profiles for experiment B3 (average of all replicates).

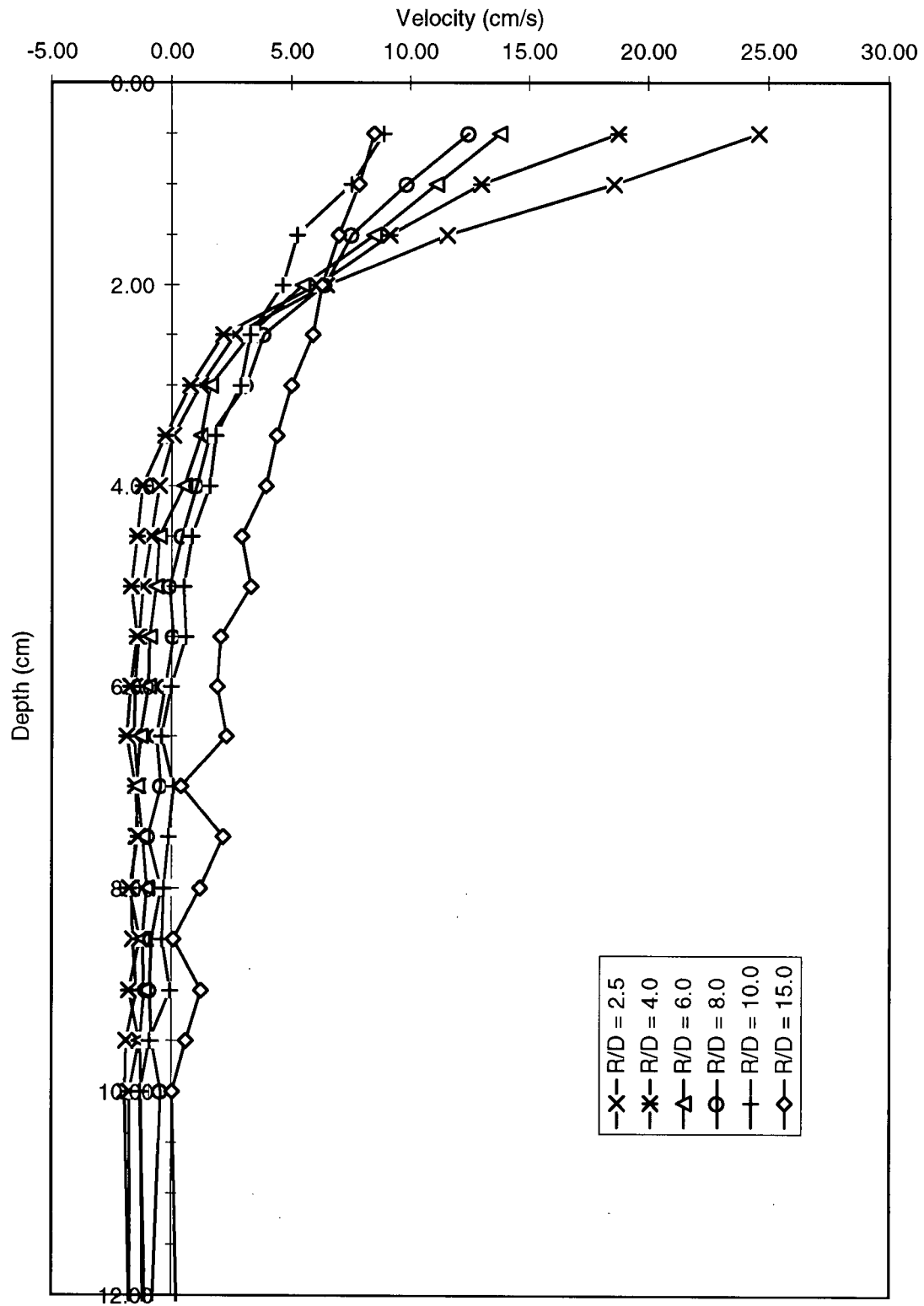


Figure C.5: Time averaged radial velocity profiles for experiment B4 (average of all replicates).

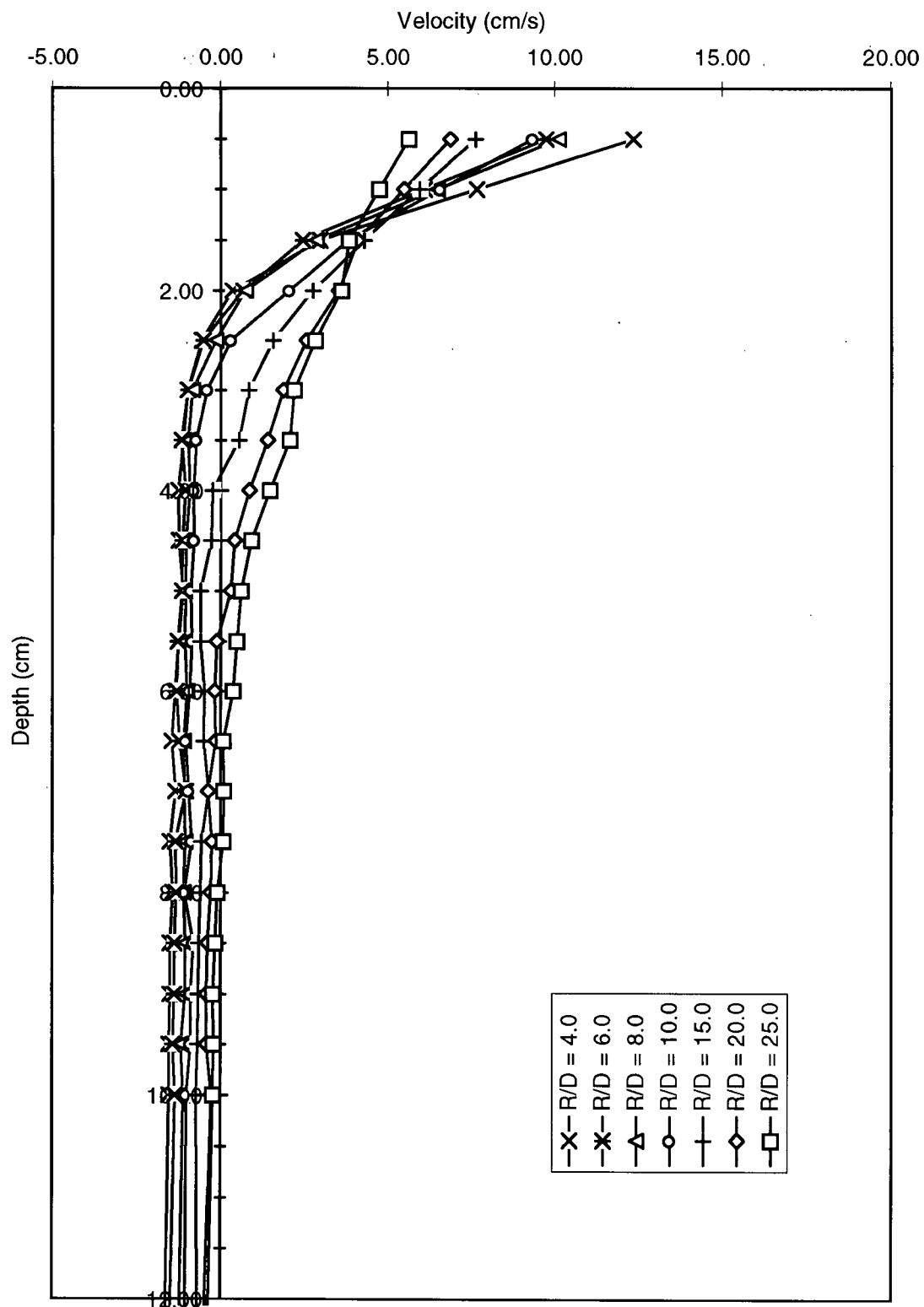


Figure C.6: Time averaged radial velocity profiles for experiment C1 (average of all replicates).

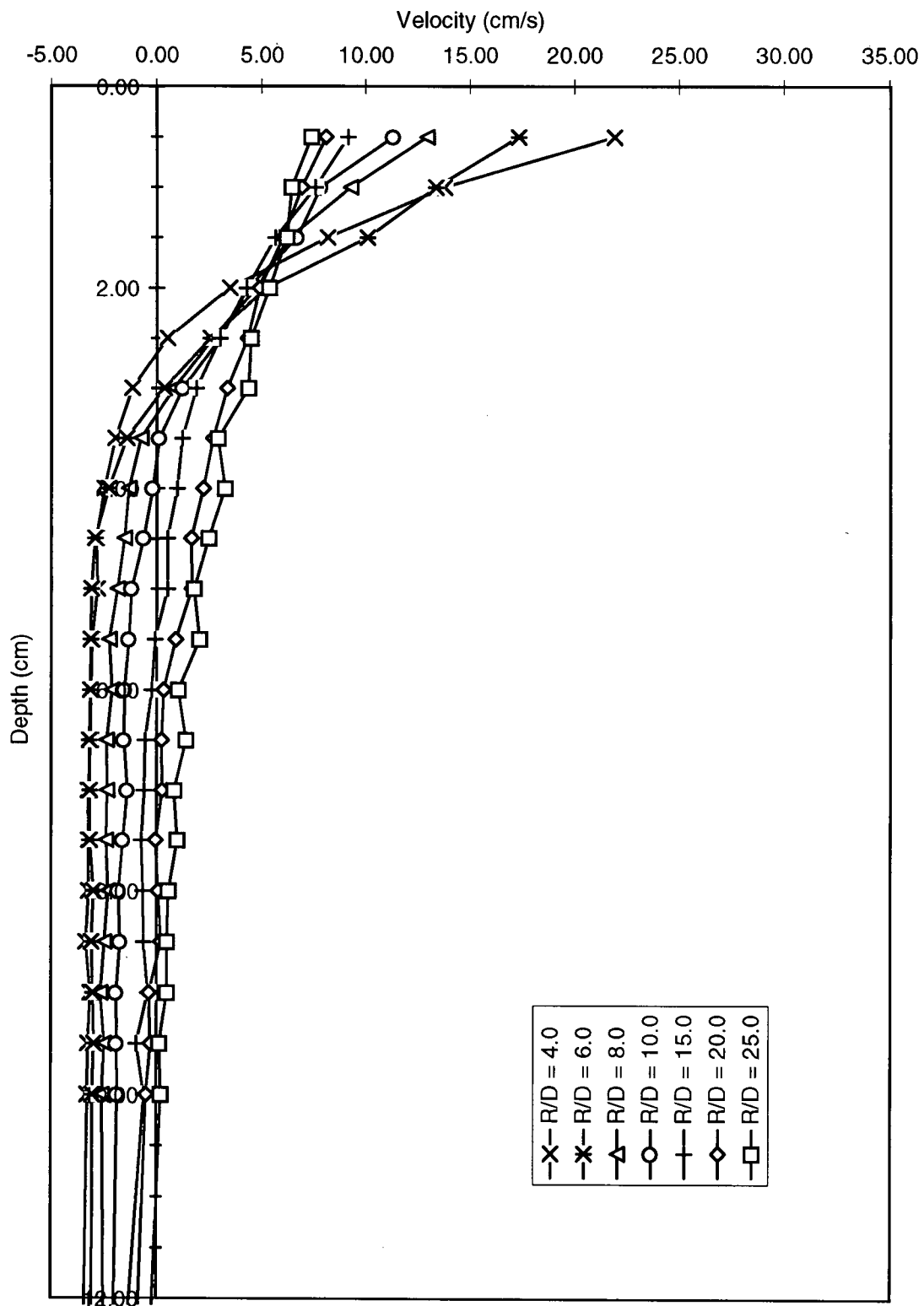


Figure C.7: Time averaged radial velocity profiles for experiment C2 (average of all replicates).

**Appendix D****Plots of Temperature Profiles for Individual Experiments**

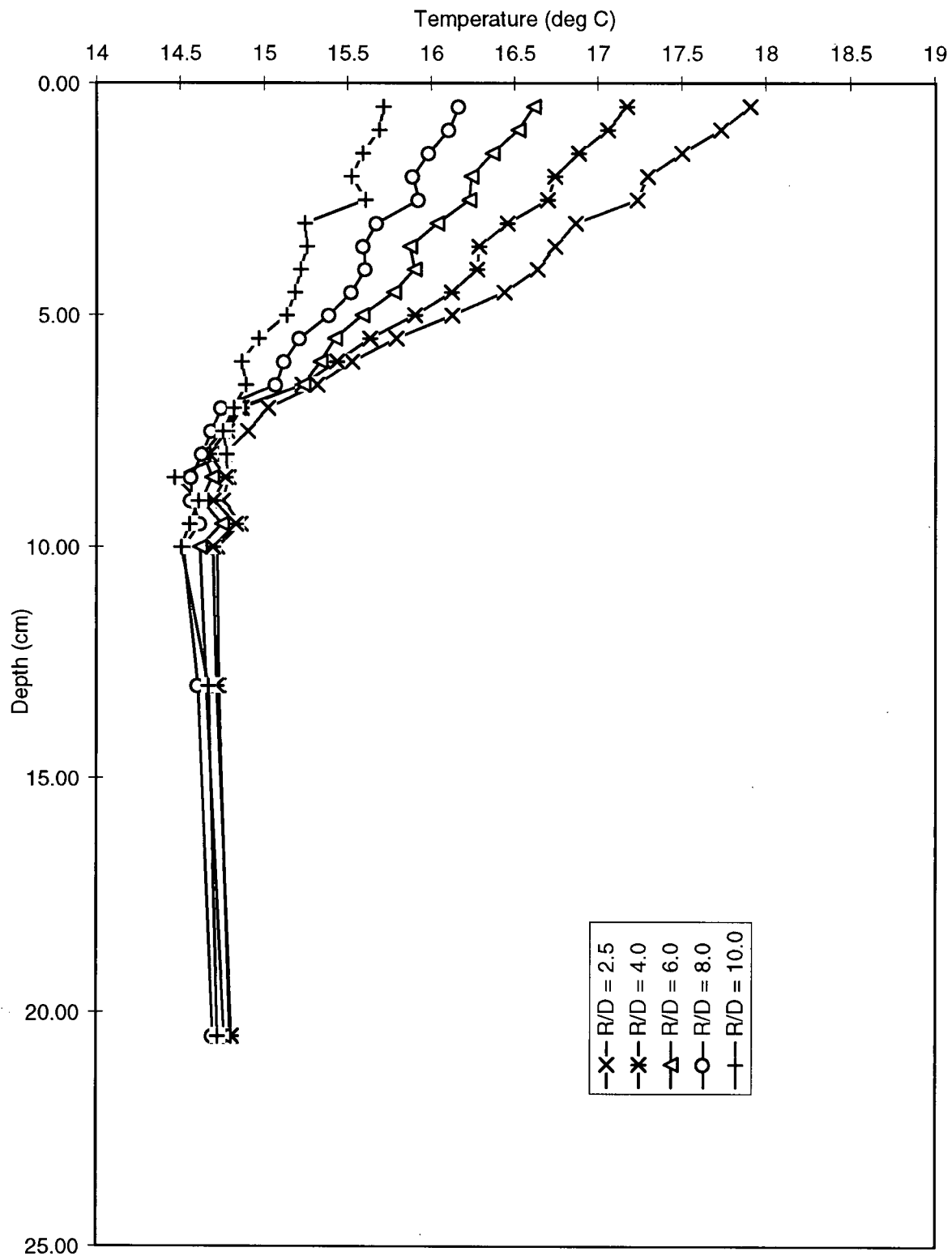


Figure D.1 Time averaged temperature profiles for experiment A1 (average of all replicates).

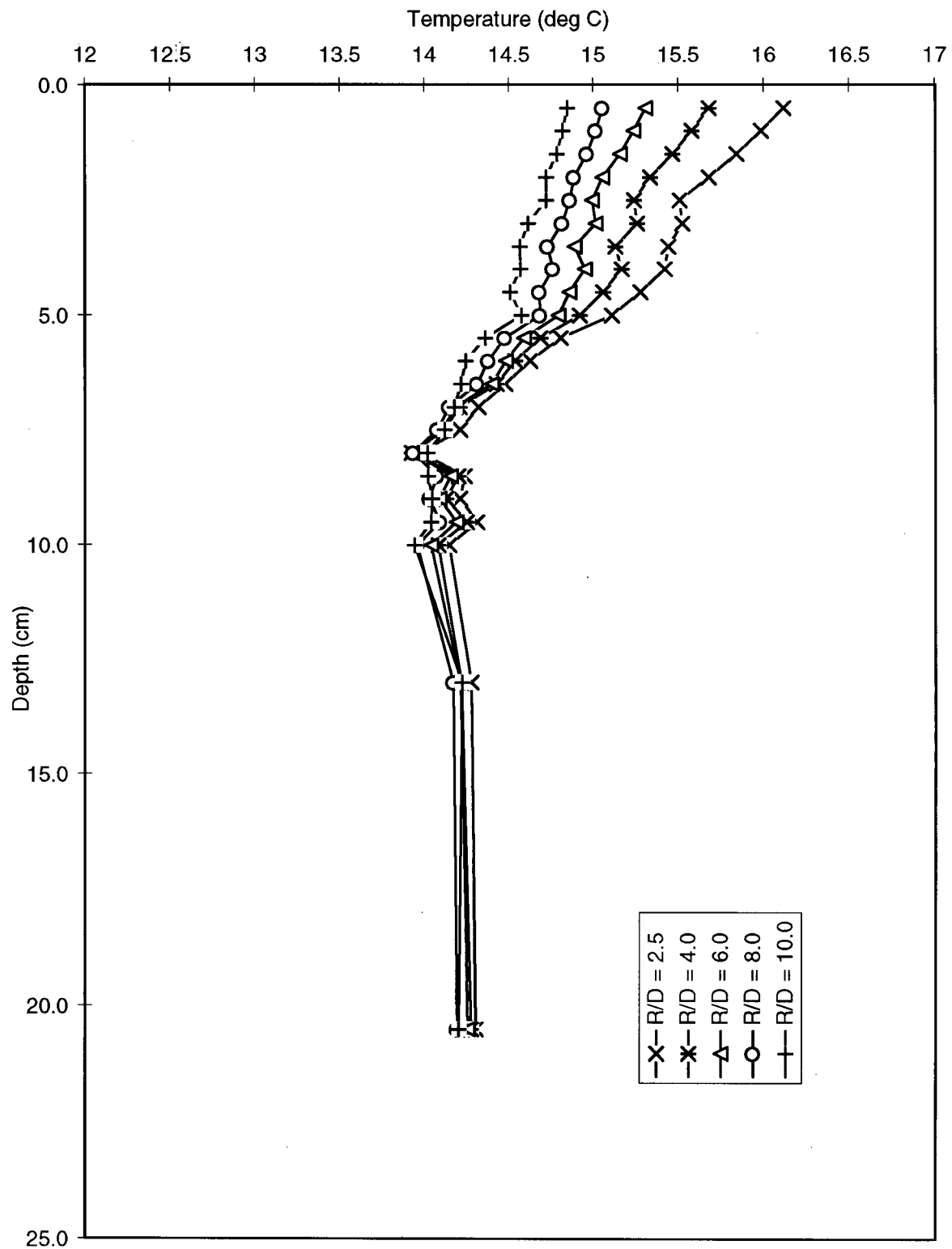


Figure D.2 Time averaged temperature profiles for experiment A2 (average of all replicates).

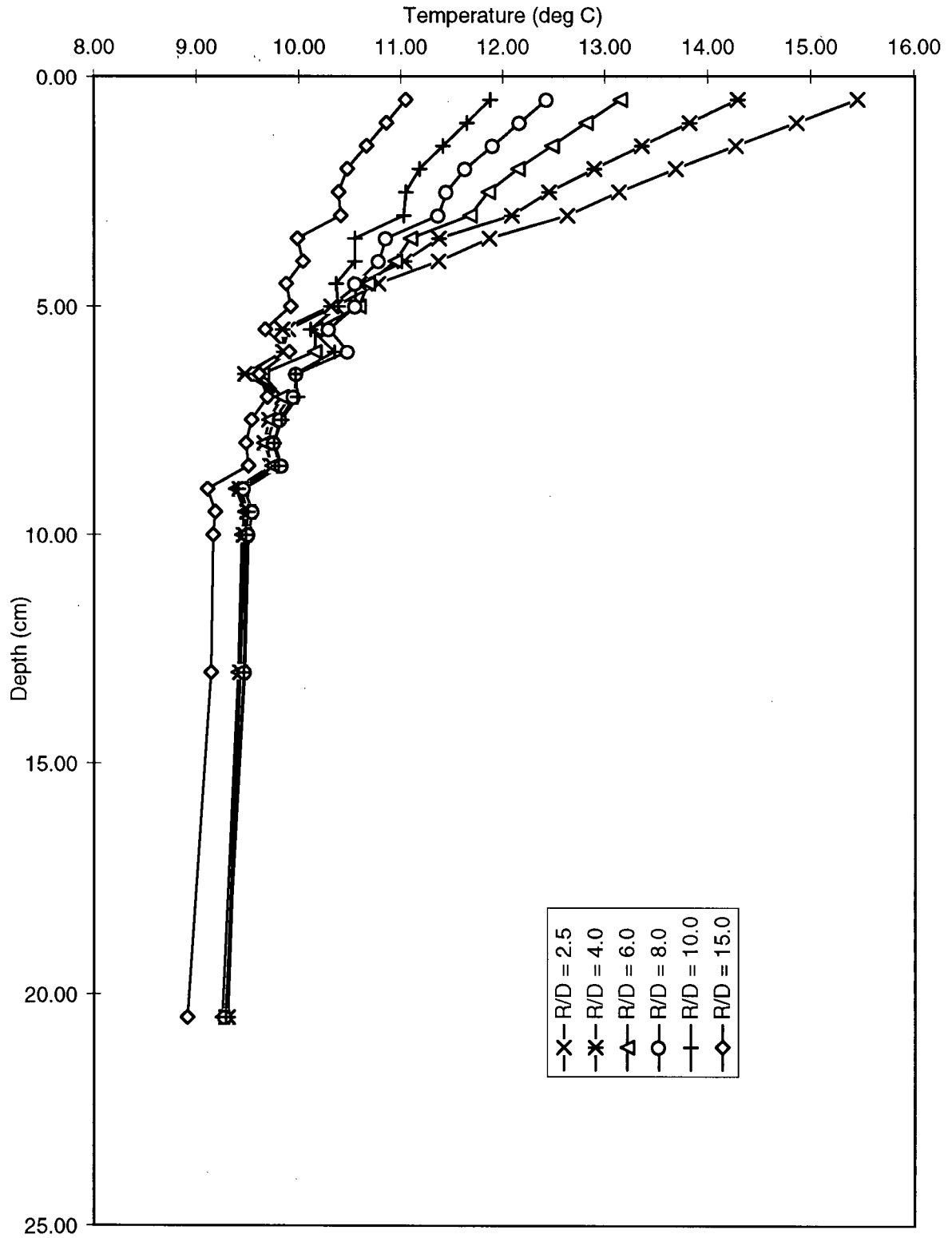


Figure D.3 Time averaged temperature profiles for experiment B2 (average of all replicates).

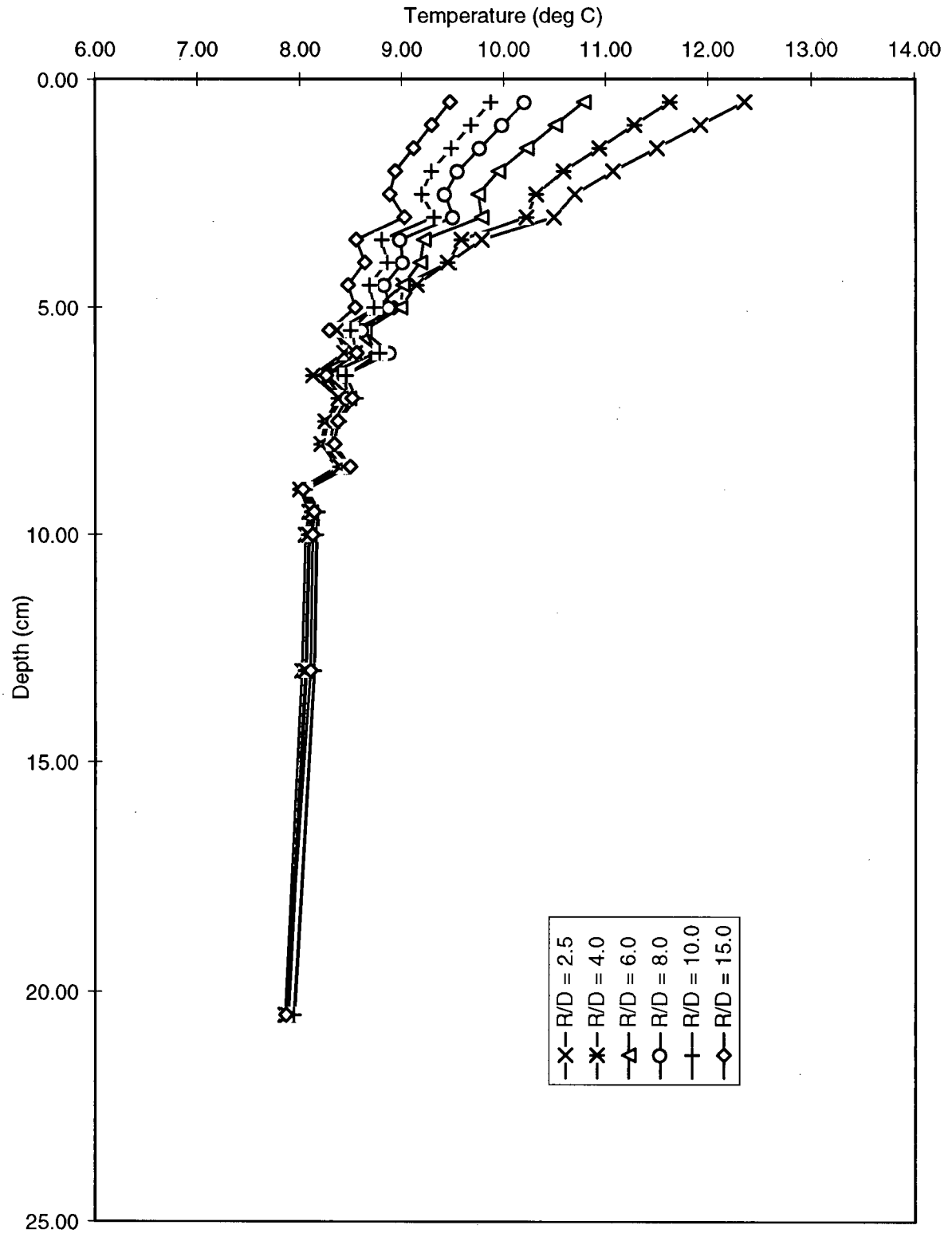


Figure D.4 Time averaged temperature profiles for experiment B3 (average of all replicates).

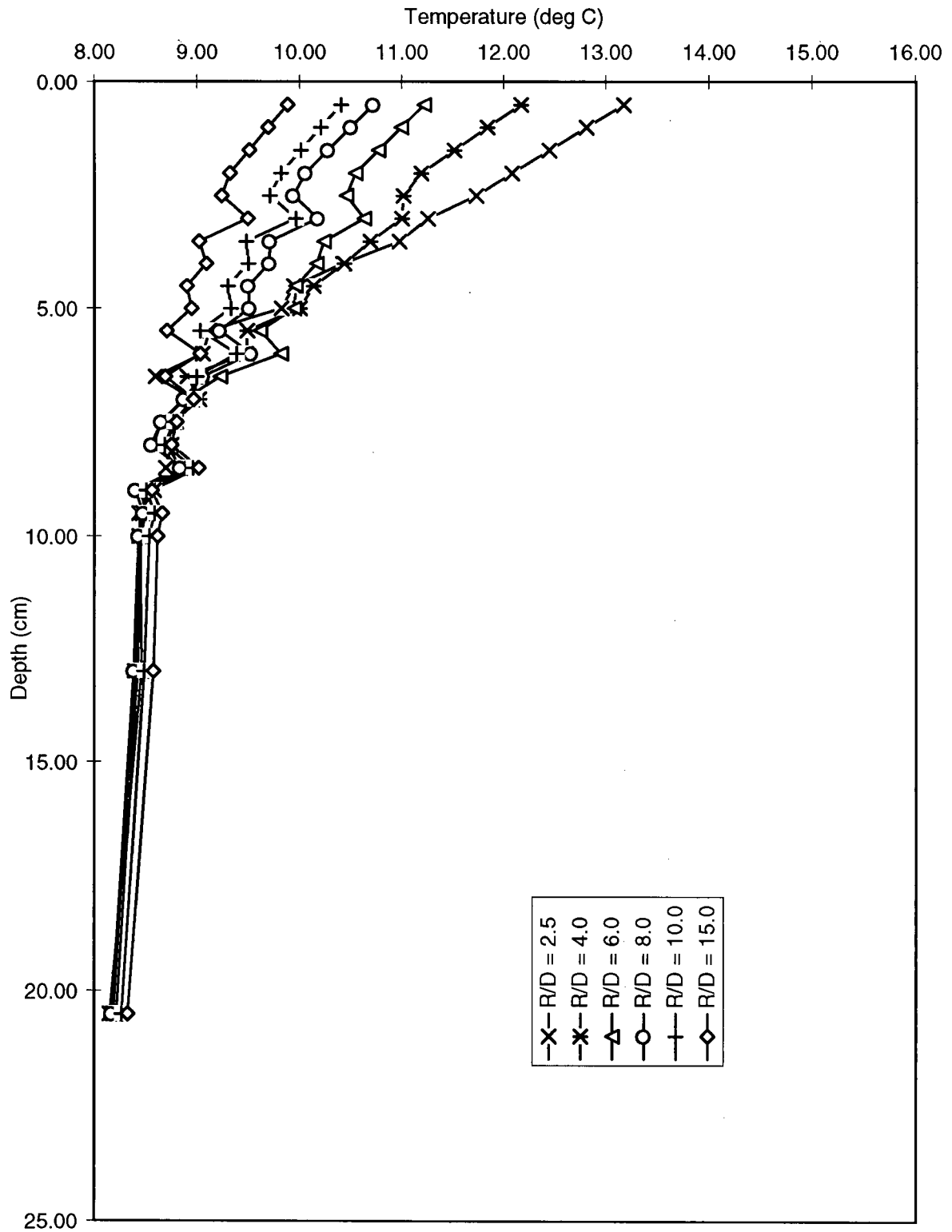


Figure D.5 Time averaged temperature profiles for experiment B4 (average of all replicates).

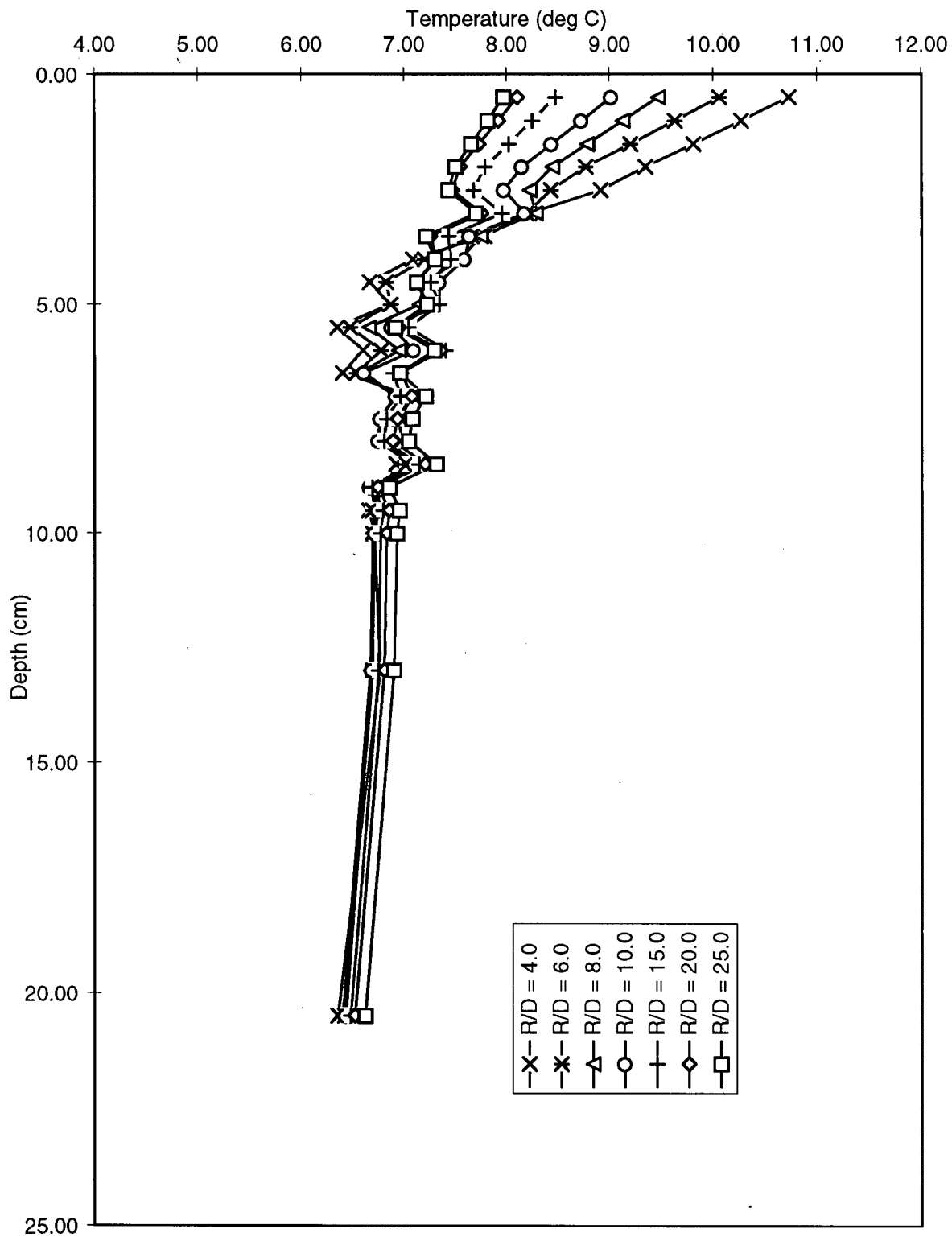


Figure D.6 Time averaged temperature profiles for experiment C1 (average of all replicates).

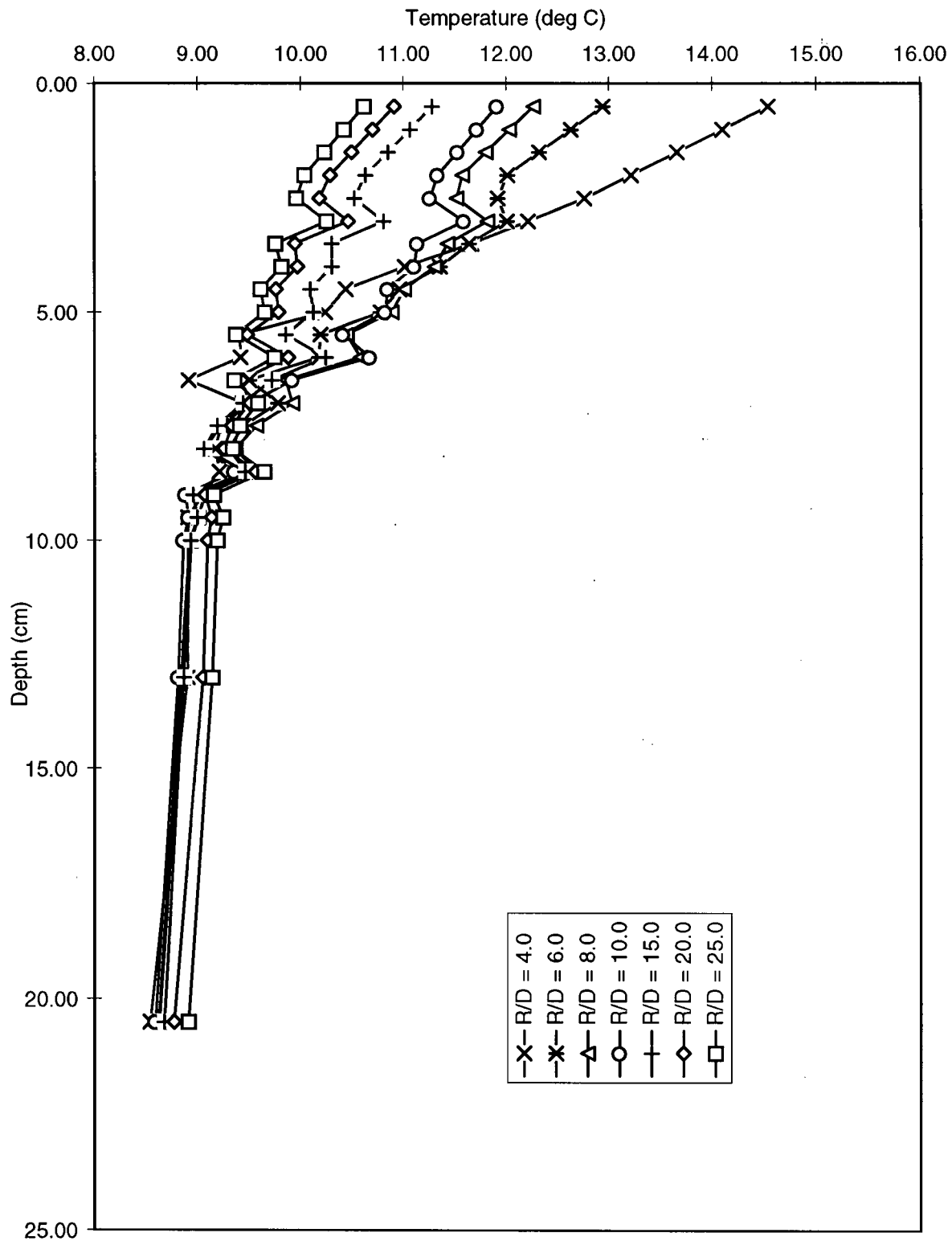


Figure D.7 Time averaged temperature profiles for experiment C2 (average of all replicates).